Ph. D.
Thesis

SUBIR SARKAR

Thesis-1997-Sarkar

1997

L3 Note 21

Study of Hadronic Events in e^+e^- Collisions using L3 Detector at Large Electron Positron (LEP) Collider at CERN

SUBIR SARKAR

Tata Institute of Fundamental Research
BOMBAY

1997

Study of Hadronic Events in e^+e^- Collisions using L3 Detector at Large Electron Positron (LEP) Collider at CERN

Subir Sarkar

Tata Institute of Fundamental Research
Bombay 400 005

A Thesis submitted to the

University of Bombay

for the degree of

Doctor of Philosophy in Physics

March, 1997

To my parents

Acknowledgement

It is a pleasure to acknowledge the guidance of my thesis supervisor, Prof. Sunanda Banerjee. I learnt not only physics from him, but also a lot about L3 software and analysis techniques starting from the very basics.

I thank the European Organisation for Nuclear Research for extending its warm hospitality and for providing a stimulating working environment. The members of the LEP accelerator group are entirely responsible for an extremely successful operation of the LEP accelerator over the years. I acknowledge their effort towards the realisation of my work.

I express my gratitude towards all the members of the L3 Hadron group. John Field, Thomas Hebbeker, Aurelio Bay, Andreas Ricker, Dominique Duchesneau, David Kirkby, Alex Buytenhuijs and Jorge Casaus helped me a lot with my analyses. I acknowledge many a help I received from Christopher Paus and Ulrich Uwer. I thank Hans, Rizwan and Mehnaz who solved all the problems I faced with different computing systems in L3.

The Tata Institute of Fundamental Research offered a pleasant atmosphere and all the facilities I might need. I would like to thank Prof. S. N. Ganguli, Prof. Atul Gurtu, Dr. R. Raghavan, Dr. K. Sudhakar, Dr. Tariq Aziz and Dr. Kajari Mazumdar for many helpful suggestions towards the refinement of my analyses.

I thank P.V. Deshpande for maintaining the computing system in our group in good shape all along.

I thank all my fellow students in the group who helped me with all physics and other general issues at every occasion. I enjoyed the relationship with Sandeep, Manas, Gobinda, Tania, Satyaki, Raja and Swagoto.

I acknowledge the true friendship I have enjoyed with Tapan, Debajyoti, Krishanu, Sreerup, Bunty, Gautam, Monoranjan, Zakir, Kartik, Soma, Nirmalya, Sandeep (SSP), Mrinal and Dilip.

Synopsis

Title of the Thesis	:	Study of Hadronic Events in e^+e^- collisions using L3 Detector at Large Electron Positron (LEP) Collider at CERN.
Name of the Candidate	:	Mr. Subir Sarkar
Registration No.	:	TIFR–27 dated 26.04.93
Degree	:	Doctor of Philosophy
Subject	:	Physics
Thesis Supervisor	:	Prof. Sunanda Banerjee
Institution	:	Tata Institute of Fundamental Research.

The strong interactions of quarks and gluons are described by Quantum Chromodynamics (QCD) [1]. The predictions of the perturbative QCD can be tested with high precision from e^+e^- interactions at the Large Electron Positron (LEP) Collider. In e^+e^- interactions, the initial state of the process is completely known. So studies of final states with hadrons can reveal the structure of the strong interactions. In the first phase of operation, LEP has copiously produced events at Z peak allowing for a precise test of the Standard Model of particle physics. In the second phase, the center of mass energy has been increased above the threshold for W^+W^- production.

At the Z resonance the hadronic cross section is large compared to the other background processes. The initial state radiation and the interference between initial and final state radiation are highly suppressed. The high momentum quarks and gluons form jets of hadrons, which preserve the energy and direction of the primary partons. At these energies, hadronisation effects are small and the jets formed are collimated. High energy and copious production of hadronic events at the Z resonance makes LEP an ideal laboratory for QCD related studies. At higher center of mass energies away from the Z peak, the hadronic cross section is small and the effect of initial state radiation is significant. These two facts make the study of the hadronic events at energies beyond Z resonance difficult.

The most important measurement in QCD is the determination of the strong coupling constant, α_s, which is the only free parameter in the theory. Numerous electroweak and QCD tests rely on an accurate determination of the strong coupling constant. The work presented in this thesis describes the determination of α_s, (a) at various center of mass energies in the range from 30 GeV to 86 GeV using hadronic events with a hard photon in the final state from Z decays, and (b) at $\sqrt{s} = 161$ GeV. These measurements can be used together with the other measurements of α_s from L3 to test energy evolution of the strong coupling constant.

In e^+e^- interactions, hadronic events are characterised by a large number of charged and neutral particles in the final state and these particles are dominantly produced at large scattering angles. So in experiments with hermetic detectors, a large fraction of the incident energy is visible in hadronic events. One can utilise the above feature of the hadronic events to perform the final energy calibration. This is accomplished by scaling the total visible energy to the center of mass energy, which is precisely known. The energy and spatial resolutions which characterise the L3 electromagnetic and hadron calorimeters allow us to determine the energy of the particles accurately from the raw energy deposited in the calorimeters (and optionally from the momentum measured in the tracking chamber and the muon chambers) using simple weight factors for different detector regions. These factors are known as the G-factors. Two methods of energy determination have been described. The standard algorithm uses the linear combination of energy measured in the calorimeters and the muon chambers. On the other hand, the second method makes use of information from the tracking chamber as well and also the correlations in the measurement of energy among adjacent detector components. This introduces nonlinear terms in the energy determination. Performances of the two methods are compared. Energy Calibration has been performed for the entire period of running of LEP at Z peak as well as at the higher energy points.

We have studied the structure of hadronic events with a hard radiated photon ($e^+e^- \rightarrow Z \rightarrow$ hadrons $+ \gamma$) where the photon is visible in the detector. The event sample has been recorded by the L3 detector at center of mass energy around 91 GeV. The high energy photons of interest are radiated either through initial state radiation which is strongly suppressed around Z resonance or through an early branching in the process of quark bremsstrahlung. On the other hand, the development of hadronic shower takes place over a larger time scale. Therefore, the emitted photon becomes decoupled from the system and strong interactions take place at a reduced effective center of mass energy. If s is the true center of mass energy then the effective center of mass energy s′ is given by the relation

$$\sqrt{s'} = \sqrt{s\left(1 - \frac{2E_\gamma}{\sqrt{s}}\right)}$$

where E_γ is the energy of the emitted photon. The center of mass energy of the hadronic subsystem in this study lies in the range between 30 GeV and 86 GeV. Event shape variables, like thrust, heavy jet mass, total, wide jet broadening etc., have been studied at these reduced center of mass energies and have been compared with the predictions of different QCD Monte Carlo programs.

Selection of hadronic events with high energy isolated photons in the final state requires rejection of a huge background from neutral hadrons decaying either into two photons unresolved in the detector or two well separated photons only one of which is detected. Small contributions come from $\tau^+\tau^-$ and two photon ($e^+e^- \rightarrow e^+e^-$ + hadrons) events. One needs to apply sophisticated topological cuts on photon candidates and to exploit the specific features of the detector to achieve the required purity at a reasonable selection efficiency.

We have studied a number of event shape variables from the sample of hadronic events produced in e^+e^- interactions at $\sqrt{s} = 161$ GeV. At this energy, well beyond the Z resonance, hard initial state radiation dominates, decreasing the effective center of mass energy to m_Z. The emitted initial state photons mostly go unnoticed down the beam pipe, but some of them may be detected well inside the detector. So the selection of hadronic events which are produced at $\sqrt{s} = 161$ GeV needs specific criteria to remove hadronic events produced at lower center of mass energy. Apart from the contribution from irreducible background coming from initial state radiation, the selected data sample contains a background contribution from W^+W^- events, the production of which is kinematically allowed at this energy. The two photon background too becomes significant at this energy.

The selected data samples have been corrected for background contamination, detector resolution and finite acceptance effects on a bin-by-bin basis, which is dictated by the available statistics, for all the energy points. The global structure of these events is well reproduced by several Monte Carlo models, based on parton shower evolution, together with string or cluster fragmentation and with parameters adjusted using hadronic Z decays at $\sqrt{s} = 91$ GeV. We have studied the evolution of the mean values of the event shape variables under consideration with center of mass energy after correction, which are given in tables 1 and 2, where the first error is statistical and the second one systematic. The mean values of the event shape variables obtained earlier by L3 [2], [3] at $\sqrt{s} = 91$, 130, and 136 GeV are listed for completeness. The mean value of the corrected charged multiplicity at $\sqrt{s} = 161$ GeV is obtained to be $< n_{ch} >$ $= 25.59 \pm 0.4$ (stat) $\pm$ 0.4 (syst). The energy evolution of these variables are compared with different QCD models. Data agrees reasonably well with the predictions from different parton shower models.

$\sqrt{s}$ (GeV)	<T>	$< \rho >$
30–50	0.906 ±0.003 ±0.004	0.065 ±0.002 ±0.002
50–60	0.917 ±0.002 ±0.003	0.061 ±0.002 ±0.003
60–70	0.922 ±0.002 ±0.003	0.059 ±0.001 ±0.002
70–80	0.928 ±0.001 ±0.003	0.051 ±0.001 ±0.002
80–84	0.929 ±0.002 ±0.004	0.051 ±0.001 ±0.002
84–86	0.932 ±0.002 ±0.005	0.050 ±0.001 ±0.003
91	0.9364±0.0003±0.0021	0.0539±0.0001±0.0014
130	0.948 ±0.004 ±0.007	0.045 ±0.003 ±0.001
136	0.943 ±0.005 ±0.008	0.046 ±0.004 ±0.001
161	0.946 ±0.003 ±0.001	0.044 ±0.003 ±0.002

Table 1: Mean values of thrust (T), scaled heavy jet mass (ρ), measured at various center of mass energies. For completeness mean values at $\sqrt{s} = 91$, 130, and 136 GeV are listed as well. The first error is statistical and the second one systematic.

Finally from a fit of the corrected data to resummed $\mathcal{O}({\alpha_s}^2)$ QCD calculations, we determine the strong coupling constant α_s over a wide range of energy in the range from 30 GeV to 86 GeV and at $\sqrt{s} = 161$ GeV as given in table 3. For the sake of completeness values of α_s obtained by L3 [2], [3] at $\sqrt{s} = 91$ and 133 GeV are also listed. Statistical error is combined

$\sqrt{s}$(GeV)	$< B_T >$	$< B_W >$
30–50	0.139±0.002±0.002	0.088±0.002±0.004
50–60	0.127±0.002±0.002	0.083±0.002±0.004
60–70	0.120±0.002±0.003	0.081±0.002±0.004
70–80	0.113±0.001±0.002	0.075±0.001±0.005
80–84	0.112±0.002±0.004	0.075±0.001±0.005
84–86	0.109±0.002±0.005	0.073±0.002±0.006
91	0.1102 ± 0.0022	0.0738 ± 0.0019
130	0.095±0.004±0.001	0.067±0.003±0.001
136	0.094±0.005±0.001	0.066±0.004±0.001
161	0.094±0.003±0.001	0.068±0.003±0.002

Table 2: Mean values of total jet broadening (B_T), and wide jet broadening (B_W), measured at various center of mass energies. For completeness mean values at $\sqrt{s}$ = 91, 130, and 136 GeV are listed as well. The first error is statistical and the second one systematic. For total and wide jet broadening at $\sqrt{s}$ = 91 GeV the error given is a combination of statistical and systematic errors.

with systematic error in quadrature to give the total experimental error. Theoretical errors come due to approximations in the calculation of the higher order corrections and also due to uncertainties in modelling fragmentation. We find the energy dependence of the strong coupling constant α_s to be consistent with expectations from QCD.

$\sqrt{s}$ (GeV)	α_s ($\sqrt{s}$)	$\Delta\alpha_s$ (experimental)	$\Delta\alpha_s$ (theoretical)
30–50	0.139	± 0.010	± 0.009
50–60	0.139	± 0.011	± 0.007
60–70	0.132	± 0.008	± 0.006
70–80	0.116	± 0.008	± 0.006
80–84	0.118	± 0.010	± 0.007
84–86	0.111	± 0.010	± 0.005
91	0.124	± 0.003	± 0.008
133	0.107	± 0.005	± 0.006
161	0.102	± 0.005	± 0.005

Table 3: α_s at the various center of mass energies from the four fits to the event shape variables. For the sake of completeness values of α_s at $\sqrt{s}$ = 91 and 133 GeV are also listed.

References

[1] M. Gell-Mann, Acta Phys. Austriaca Suppl. **IX** (1972) 733;
H. Fritzsch and M. Gell-Mann, 16th International Conference on High Energy Physics, Batavia, 1972; editors J.D. Jackson and A. Roberts, National Accelerator Laboratory

(1972);

H. Fritzsch, M. Gell-Mann and H. Leytwyler, Phys. Lett. **B47** (1973) 365;

D.J. Gross and F. Wilczek, Phys. Rev. Lett. **30** (1973) 1343;

D.J. Gross and F. Wilczek, Phys. Rev. **D8** (1973) 3633;

H.D. Politzer, Phys. Rev. Lett. **30** (1973) 1346;

G. 't Hooft, Nucl. Phys. **B33** (1971) 173.

[2] L3 Collaboration, B. Adeva *et al.*, Z. Physik **C55** (1992) 39.

S. Banerjee, S. Müller, L3 Internal Note no. 1441, (1993).

[3] L3 Collaboration, M. Acciarri, Phys. Lett. **B371** (1996) 137.

Statement Required Under Ordinance 0.770

I hereby state that the work presented in this thesis has not been submitted to this or any other university for Ph.D or any other degree.

Statement Required Under Ordinance 0.771

Statement No. 1 regarding new facts:

The study of quantum chromodynamics and determination of strong coupling constant at various center of mass energies in the range from 30 GeV to 86 GeV demonstrates the novel use of the hadronic events from Z decays with a hard photon in the final state. It describes the running of the strong coupling constant with center of mass energy where the systematic errors, both experimental and theoretical, are common to all the energy points. There has been no direct measurement of strong coupling constant in the energy range from 70 GeV to 85 GeV from e^+e^- interactions. This analysis, which is the first of its kind, provides the above mentioned energy range with reliable measurements. The other analysis described in this thesis is the determination of strong coupling constant at a center of mass energy of 161 GeV which is one of the first measurements of the strong coupling constant at this energy in e^+e^- collisions.

Statement No. 2 regarding author's contribution in joint work:

The L3 experiment is a huge collaborative effort comprising of around 500 physicists from about 40 institutes/laboratories all over the globe. Numerous individuals have contributed significantly towards the successful joint venture in the fields of detector design, building and maintenance as well as software development, both online and offline, without which this work would not have been realized. The scientists and engineers of the CERN accelerator divisions contributed towards the excellent performances of the LEP collider over the years. I have carried out the analyses under the supervision of Prof. Sunanda Banerjee. A few other physicists in L3 were involved in this work. The work where major responsibility towards the analyses rests on the author is described in this thesis.

References are properly cited at appropriate places whenever use has been made of earlier works. The principal aspects of the work of the author can be summarised as

Energy calibration using hadronic events which is widely used in the collaboration.

Optimisation of the procedure of selection of hadronic events with hard photon(s) in the final state using events from Z decays. Estimation of the background contaminations.

Study of the Initial state radiation at a center of mass energy of 161 GeV and optimisation of the selection method for hadronic events.

Study of various global event shape variables. Correction of the detector level distribution for background, detector resolution and finite detector acceptance. Study of the energy evolution of the mean values of the event shape variables.

Determination of the strong coupling constant at various center of mass energies using the selected sample of events alongwith the estimation of statistical and systematic errors coming from different sources.

Testing the energy evolution of the strong coupling constant using the L3 measurements at various center of mass energies.

Subir Sarkar
Signature of the Candidate

Sunanda Banerjee
Signature of the Supervisor

Contents

List of Figures

List of Tables

Chapter 1

Introduction and Overview

We have analysed here the structure of hadronic events in electron positron interactions. The study has been carried out on an event sample recorded by the L3 detector from 1991 to 1994, with a hard photon radiated in the final state ($e^+e^- \rightarrow Z \rightarrow hadrons + \gamma$). The centre of mass energy corresponds to about 91 GeV. The motivation behind this study is to determine the strong coupling constant at various reduced centre of mass energies depending on the energy of the emitted photon. Determination of the strong coupling constant from one single experiment will reduce the experiment dependent systematic errors.

Radiation of high energy signal photons in hadronic events occurs either through initial state radiation or through quark (antiquark) bremsstrahlung before the first gluon branching. The complete shower, as predicted by perturbative QCD [3], develops over a larger time scale. Therefore, the onset of effects of quantum chromodynamics takes place at a reduced centre of mass energy. In other words, one can effectively look at hadron production at reduced centre of mass energies from a study of hadronic events with a hard isolated photon.

The centre of mass energy of the hadronic system is in the range between 30 GeV and 86 GeV. Event shape variables have been measured at this reduced centre of mass energies and compared with the predictions of different QCD Monte Carlo programmes. The data are in agreement with the QCD models. From a fit of the data to resummed $\mathcal{O}(\alpha_s{}^2)$ QCD calculations, we determine the strong coupling constant (α_s), over a wide range of energy.

We have studied the structure of hadronic events to determine the strong coupling constant at a centre of mass energy of 161 GeV also as a part of the work.

A brief outline of the thesis is given below :

Chapter 2 discusses the essential aspects of the Standard Model of elementary particle interactions which is extremely successful in explaining most of the observations in high energy physics. Perturbative Quantum Chromodynamics (QCD) relevant for the process

$e^+e^- \rightarrow Z \rightarrow$ *hadrons* has been discussed in detail.

Chapter 3 provides a description of the Large Electron Positron (LEP) collider and the L3 detector with all its subdetectors and their performances. The online L3 trigger system is also described.

Chapter 4 gives a general outline of the Monte Carlo Simulation of events in the L3 framework which is divided into event generation and detector simulation. Reconstruction of real and simulated events, which converts raw detector signals into meaningful objects such as tracks, clusters, jets etc. has also been presented.

Chapter 5 describes the general ideas behind the energy calibration of the L3 detector through optimisation of the energy resolution using hadronic Z decays. The standard energy flow analysis and an improved algorithm are presented. A comparison between the two algorithms reveals the impact of the new algorithm of energy determination on a variety of physics analyses.

Chapter 6 presents the selection of hadronic events and subsequent selection of a sample of hadronic events with a hard, isolated photon in the final state. The irreducible background contamination in the selected sample has been estimated using detector simulated Monte Carlo events. Several event shape variables have been studied over a large energy range. The background subtracted data is corrected for the detector resolution and acceptance effects.

Chapter 7 presents the selection of hadronic events during a high energy run of LEP, at a centre of mass energy of 161 GeV. The huge background due to initial state radiation and other processes has been minimised and the observed global event shape distributions are corrected for the effects of remaining background, detector resolution and acceptances.

Chapter 8 describes the analysis which finally leads to the determination of strong coupling constant (α_s), at various centre of mass energies. The different sources of errors on the strong coupling constant have been discussed in detail. The values of the coupling constant, obtained from reduced hadronic system and the high energy point, are placed in the proper context of QCD evolution with centre of mass energy. Thus, we verify the running of the strong coupling constant as predicted by quantum chromodynamics.

Chapter 9 summarises the main results of the work presented in this thesis.

Chapter 2

Standard Model of Particle Physics

The Standard Model (SM) of particle physics [1], is a unified description of the strong, weak, and electromagnetic interactions of the fundamental particles. Numerous experimental inputs have gone into the development of the theory.

2.1 Particle Content of the Standard Model

The Standard Model is a local quantum field theory. The Lagrangian of the theory is invariant under a $\mathrm{SU(3)_C} \otimes \mathrm{SU(2)_L} \otimes \mathrm{U(1)_Y}$ transformation. The field content of Standard Model is the following.

2.1.1 Gauge Sector

Local gauge invariance requires the presence of a set of massless gauge fields. The gauge bosons are spin 1 vector fields. The gauge fields are $G^a_\mu(a = 1, 2, .., 8)$, $W^i_\mu(i = 1, 2, 3)$ and B_μ corresponding to the symmetry groups $\mathrm{SU(3)_C}$, $\mathrm{SU(2)_L}$ and $\mathrm{U(1)_Y}$ respectively. The corresponding gauge couplings are denoted by $\mathrm{g_s}$, g and g$'$.

2.1.2 Fermion Sector

The known matter fields are spin 1/2 fermions: quarks and leptons. Three generations of fermions have been found experimentally. The charged leptons take part in electromagnetic and weak interactions whereas the neutral leptons take part only in weak interactions. The quarks feel all the three interactions discussed above. Table 2.1 lists the fermions and their various quantum numbers.

2.1.3 Scalar Sector

Some of the physical gauge bosons are massive, although gauge invariance requires them to be massless. Spontaneous symmetry breaking (SSB) was introduced as a mechanism to

	Families			I_3	Y	Q
Leptons	$\begin{pmatrix} \nu_e \\ e \end{pmatrix}_L$	$\begin{pmatrix} \nu_\mu \\ \mu \end{pmatrix}_L$	$\begin{pmatrix} \nu_\tau \\ \tau \end{pmatrix}_L$	+1/2 −1/2	−1 −1	0 −1
	e_R	μ_R	τ_R	0	−2	−1
Quarks	$\begin{pmatrix} u \\ d \end{pmatrix}_L$	$\begin{pmatrix} c \\ s \end{pmatrix}_L$	$\begin{pmatrix} t \\ b \end{pmatrix}_L$	+1/2 −1/2	+1/3 +1/3	+2/3 −1/3
	u_R	c_R	t_R	0	+4/3	+2/3
	d_R	s_R	b_R	0	−2/3	−1/3

Table 2.1: The fermion sector of the Standard Model.

generate masses of the massive gauge bosons and the massive fermions. When spontaneous symmetry breaking occurs, the Lagrangian is still invariant but the physical ground state is not.

In the minimal version of the electroweak theory one doublet of scalar (Φ) is considered. After spontaneous symmetry breaking, in addition to the fermions and the gauge bosons discussed earlier, we have a neutral scalar particle left in the spectrum, the Higgs boson. Higgs is yet to be discovered in experiments. The quantum numbers of the scalar fields in the doublet are listed in the table 2.2.

		I_3	Y	Q
Scalars	$\begin{pmatrix} \phi^+ \\ \phi^\circ \end{pmatrix}$	+1/2 −1/2	+1/2 +1/2	+1 0

Table 2.2: The scalar sector of the Standard Model.

2.2 Electroweak Interactions

The electroweak theory incorporates electromagnetic and weak forces in a common gauge structure. The theory is based on the internal symmetry group $SU(2)_L \otimes U(1)_Y$.

The free parameters of the electroweak theory are the gauge couplings (g and g$'$) of the symmetry group $SU(2)_L \otimes U(1)_Y$, the vacuum expectation value (v) of the scalar field Φ, the mass parameter of the postulated Higgs particle, the fermion mass parameters (m_f) and the quark mixing (CKM) matrix elements. The first three parameters are replaced by three more convenient parameters, $\alpha = e^2/4\pi$, the fine structure constant, G_F, the Fermi constant and $\sin^2\theta_W$, where θ_W is the electroweak mixing angle. The first two of these are precisely known, leaving $\sin^2\theta_W$ as the single parameter to be constrained.

2.3 Quantum Chromodynamics

Quantum Chromodynamics (QCD) [3] is a gauge theory which describes the strong interactions of the coloured spin-1/2 quarks and spin-1 gluons, collectively known as partons. QCD is based on an exact internal symmetry with non-abelian SU(3) group structure. The mediator of the strong force, gluon, carries colour charge and hence can couple to another gluon. As a consequence vacuum polarisation effects produce an anti-screening of the bare QCD charges, which results in two novel properties of the theory, asymptotic freedom and colour confinement. Asymptotic freedom tells us that the effective coupling decreases logarithmically at short distances (at high momentum transfer) making the partons quasi-free so that perturbative calculation stands relevant at that scale. Colour confinement, on the other hand, states that the potential energy between colour charges increases approximately linearly at large distances and as a consequence only colour singlet states can be formed and observed in nature.

The perturbative calculation of a process requires the use of Feynman rules describing the interactions of quarks and gluons which can be derived from the effective Lagrangian density of the interaction. The fundamental vertices of the theory are shown in figure 2.1. The applicability of the perturbative calculation depends on the size of the expansion parameter. To lowest order, the QCD gauge coupling, α_s $(= g_s^2/2\pi)$, is a constant and a free parameter of the theory. When higher order corrections are included, it is necessary to remove the ultraviolet divergences by renormalisation of the fields and couplings. It is convenient to choose a renormalisation scheme (one such choice is *modified minimal subtraction* or $\overline{\mathrm{MS}}$ scheme) for the regularisation of the divergences. The renormalisation procedure introduces, in the theory, an arbitrary mass scale μ, the point at which the subtractions which remove the ultraviolet divergences are performed. All renormalised quantities are subsequently defined at this common energy scale μ.

2.3.1 Running of Strong Coupling Constant

Running of the coupling constant is described by

$$\mu^2 \frac{\partial \alpha_s}{\partial \mu^2} = -{\alpha_s}^2 \sum_{k=0} \beta_k {\alpha_s}^k$$

The renormalisation scale (μ) is interpreted as an energy scale. Hence $\alpha_s(\mu)$ is the strong coupling constant at an energy scale μ.

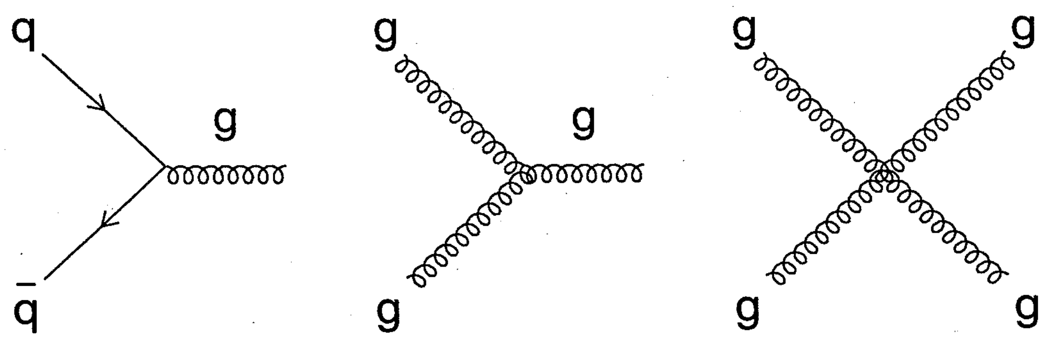

Figure 2.1: Fundamental Feynman diagrams of QCD describing quark-gluon and gluon self couplings.

The first three β-coefficients have been calculated [4]. They are given by

$$\begin{aligned}
\beta_o &= \frac{33 - 2\,N_f}{12\pi} && = 0.610 \\
\beta_1 &= \frac{153 - 19\,N_f}{24\pi^2} && = 0.245 \\
\beta_2 &= \frac{77139 - 15099\,N_f + 325\,{N_f}^2}{3456\pi^3} && = 0.091
\end{aligned}$$

The evolution equation in the lowest order can be written as

$$\mu^2 \frac{\partial \alpha_s}{\partial \mu^2} \equiv \frac{\partial \alpha_s}{\partial \ln\mu^2} = -\beta_o {\alpha_s}^2$$

which has the solution given by

$$\alpha_s(\mu) = \frac{\alpha_s(\mu_o)}{1 + \beta_0 \alpha_s(\mu_o) \ln(\mu^2/\mu_o^2)},$$

where μ_o is a reference scale. The above relation shows that α_s decreases with increasing μ for $N_f \leq 16$, This is contrary to the analogous running of the electromagnetic or weak coupling constants which increase with increasing energy.

The next-to-leading order solution can be written as

$$\alpha_s(\mu) = \frac{1}{\beta_o \ln(\mu^2/\Lambda^2)} \left[1 - \frac{\beta_1 \ln\ln(\mu^2/\Lambda^2)}{\beta_o^2 \ln(\mu^2/\Lambda^2)} \right]$$

The parameter Λ indicates the boundary between non-perturbative and perturbative energy ranges and is given by

$$\Lambda = \mu_o \exp\left(\frac{1}{-2\beta_o \alpha_s(\mu_o)} \right)$$

One can choose either α_s or Λ as the free parameter of the theory. The parameter α_s is a function of the scale μ and is more suited as it is directly related to experimental measurement.

2.3.2 Tests of QCD at LEP

The discovery of quark and gluon jets, confirmation of gluon spin of 1, determination of number of colours $N_C = 3$, and the measurement of strong coupling constant to second order at the pre-LEP e^+e^- colliders [5,6] convincingly established QCD as the theory of strong interaction. The process $e^+e^- \to$ *hadrons* at high centre of mass energies illustrates the basic ideas and properties of perturbative QCD.

In e^+e^- interactions at LEP, the initial state of the process is clean and fully known which offers a straightforward energy scale at which quantum chromodynamics takes place. At the Z resonance the hadronic cross section is large and the background small. Hard initial state radiation is strongly suppressed. The high momentum quarks and gluons form jets, which preserve the energy and direction of the primary partons. Hadronisation effects are small at this energy and the jets formed are collimated. High energy and copious production of hadronic events at the Z resonance makes LEP an ideal laboratory for QCD related studies [7].

Nevertheless, the precision of QCD tests is less striking compared to that of electroweak theory and is limited typically to a 10% level by the following drawbacks:

- perturbative calculations involve a large number of diagrams,
- due to the large value of the strong coupling constant the perturbative expansion series converges slowly,
- non-perturbative effects like structure functions, hadronisation are not modelled completely.

2.3.3 Hadronic Z Decays in e^+e^- Interactions

The process $e^+e^- \to$ *hadrons* can be separated into different distinct phases as depicted in figure 2.2. They correspond to different time and energy scales. In the first phase, e^+e^- annihilate to produce quark-antiquark pair via electroweak interaction. Before the annihilation, initial state QED bremsstrahlung (ISR) may occur reducing the effective centre of mass energy for hadron production. In the next step, the produced primary $q\bar{q}$ pair evolve under perturbative QCD by radiating gluons and photons (FSR). The gluons in their turn may radiate. The third phase depicts the transition from partons to hadrons which represents the non-perturbative regime. In the final step unstable hadrons decay into stable particles. The qualitative features of these decays are known, but little quantitative understanding exists. For the description of the last two phases one has to use phenomenological models inspired by QCD and experimental results which are implemented in different QCD event generators. Experimentally measured branching ratios are the main inputs in the description of the decays.

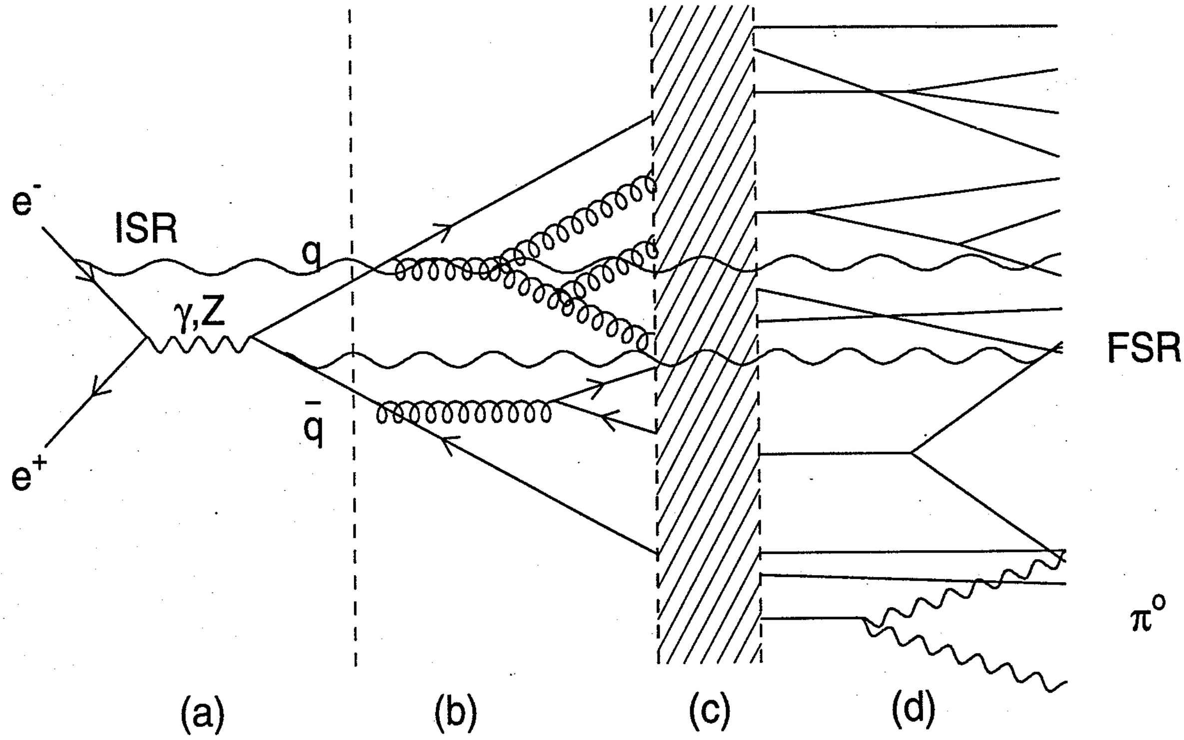

Figure 2.2: Schematic view of the distinct phases of the process $e^+e^- \rightarrow$ *hadrons*, (a) e^+e^- annihilation and production of quark-antiquark pair in an electroweak process, (b) Perturbative QCD evolution, (c) Non-perturbative regime representing transition from partons to hadrons and (d) decays of unstable hadrons into stable particles.

The observables relevant to the process $e^+e^- \rightarrow$ *hadrons* are classified in two categories. The first category contains fully inclusive observables that place no restriction on the final state, and thus allow an unambiguous interpretation of the partonic calculation. Observables in this class are related to total cross section.

The second class of observables describe the distribution of hadrons in the final state and hence represent the topology of the event. They can be classified as perturbative and non-perturbative. Examples of perturbative observables are jet differential cross-sections and various event shape variables, while examples of non-perturbative observables are number of hadrons in the final state and correlations between identical hadrons.

2.3.4 Perturbative QCD

Perturbative QCD describes the radiation of gluons off the primary quarks and the subsequent parton cascade due to gluon splittings into quarks or gluons, and radiation of gluons off secondary quarks. As the centre of mass energy increases, hard gluon emission becomes increasingly important, relative to fragmentation, in determining the event structure. There are two complementary approaches towards describing the perturbative QCD : (a) Matrix Element and (b) Parton Shower.

Matrix Element

In the Matrix Element (ME) [8] approach, Feynman diagrams are calculated, order by order. But the calculations become increasingly difficult for the higher order diagrams, in particular for the loop diagrams. Matrix Element calculations, therefore, exist only up to second order in α_s [9]. The final state consists of at most four partons. Emission of multiple soft gluon, moreover, limits the applicability of the matrix elements.

The matrix element approach takes into account exact kinematics, and the full interference and helicity structure. The strong coupling constant, α_s, has a well defined meaning in this approach. The matrix element approach is required to determine α_s and to study QCD in 3-jet and 4-jet events.

The Born process $e^+e^- \rightarrow q\overline{q}$ (figure 2.3a) is modified in the first order QCD by the process $e^+e^- \rightarrow q\overline{q}g$ as shown in figure 2.3b. For massless quarks the matrix elements reads

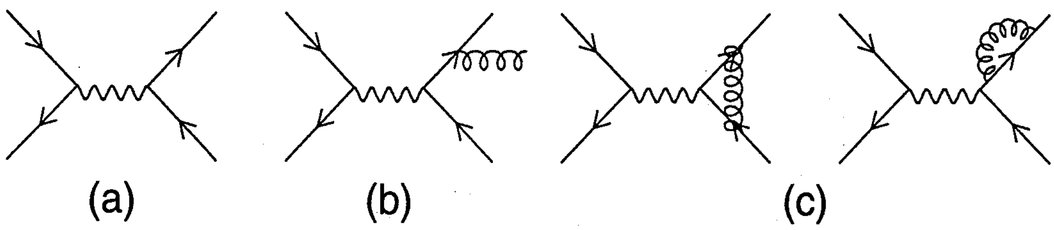

Figure 2.3: Feynman diagrams for the $\mathcal{O}(\alpha_s)$ corrections to the tree level $e^+e^- \rightarrow$ *hadrons* process, diagrams (a) and (c) have $q\overline{q}$ in the final state and are zeroth and second order respectively, whereas diagram (b) is the first order process having $q\overline{q}g$ in the final state. There are more diagrams which can be obtained by symmetry.

$$\frac{1}{\sigma_o}\frac{d^2\sigma}{dx_q dx_{\overline{q}}} = \frac{\alpha_s}{2\pi}C_F\frac{x_q^2+x_{\overline{q}}^2}{(1-x_q)(1-x_{\overline{q}})}.$$

x_q, $x_{\overline{q}}$ and $x_g = 2 - x_q - x_{\overline{q}}$ denote the scaled energy of the quark, antiquark and gluon respectively, $x_i = 2E_i/\sqrt{s}$. σ_o is the lowest order cross section and C_F is the colour factor. The cross section diverges for $x_q \rightarrow 1$ or $x_{\overline{q}} \rightarrow 1$ (collinear divergence). Similarly divergence occurs when $x_g \rightarrow 0$ (infrared divergence). When first order propagator and vertex corrections (shown in figure 2.3c) are included, the same singularity appears with opposite sign in the $q\overline{q}$ cross section. The total hadronic cross section up to $\mathcal{O}(\alpha_s)$ is thus finite and given by,

$$\sigma_{\mathrm{total}} = \sigma_o(1+\alpha_s/\pi)$$

To $\mathcal{O}(\alpha_s{}^2)$ Feynman diagrams shown in figure 2.4 are included. As in the first order, a full second order calculation consists both of real parton emission terms and of vertex and propagator correction terms.

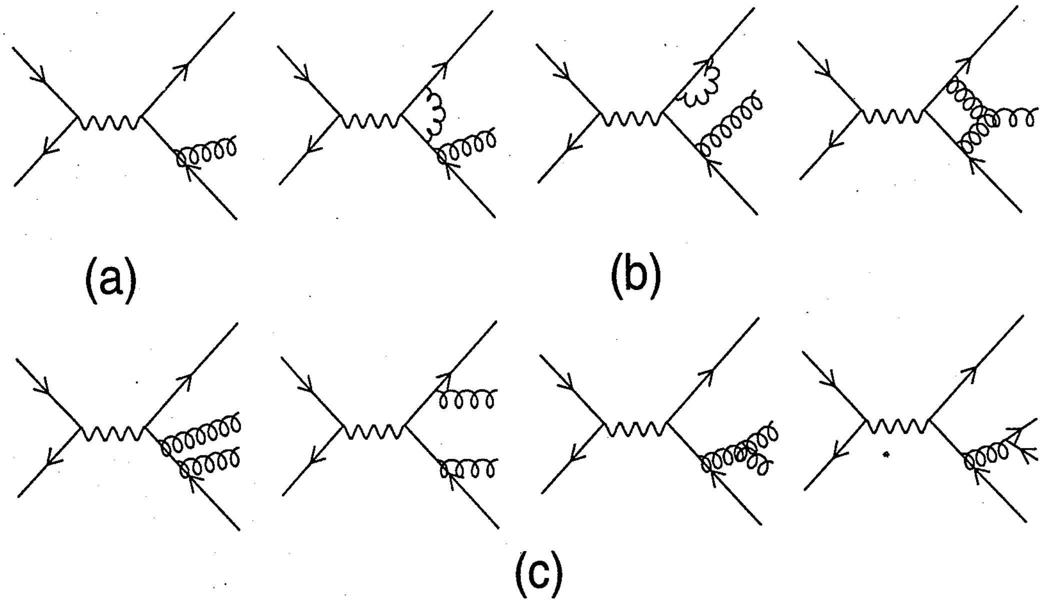

Figure 2.4: Feynman diagrams to order $\mathcal{O}(\alpha_s{}^2)$. (a) The diagram contributing to 3-jet production in first order. (b) Vertex and propagator correction diagrams which contribute 3-jet production in second order. (c) Diagrams which contribute to 4-jet production. There are more diagrams which can be obtained by symmetry.

Parton Showers

The parton shower approach [10] is derived within the framework of the leading logarithm approximation (LLA). Only the leading terms in the perturbative expansion are kept and resummed. Subleading corrections, which are down in order by factors of $\ln Q^2$ or $\ln z$ ($\ln(1-z)$), or by powers of $1/Q^2$, are thus neglected. Nevertheless, different schemes have been devised to take into account some subleading corrections like next-to-leading (NLLA) terms.

An arbitrary number of branchings of one parton into two or more may be put together, to yield a description of multi-jet events, with no explicit upper limit on the number of partons involved.

Development of the parton shower is based on an iterative use of the basic branchings $q \rightarrow qg$, $g \rightarrow gg$ and $g \rightarrow q\bar{q}$. A probabilistic approach is used to describe these branchings.

One can rewrite the differential cross section for $\mathcal{O}(\alpha_s)$ matrix element as

$$\frac{d^2\sigma}{dm^2dz} \sim \alpha_s \cdot \frac{1}{m^2} \cdot \frac{1+z^2}{1-z},$$

where $z=\frac{x_q}{x_q+x_g}$ and m is the invariant mass of the qg system. Integration over m^2 or $1-z$ (assuming $z \approx 1$) gives

$$\begin{aligned}\frac{d\sigma}{dz} &\sim \alpha_s \cdot \ln(m^2) \cdot \frac{1+z^2}{1-z}\\ \frac{d\sigma}{dm^2} &\sim \alpha_s \cdot \ln(1-z) \cdot \frac{1}{m^2}\end{aligned}$$

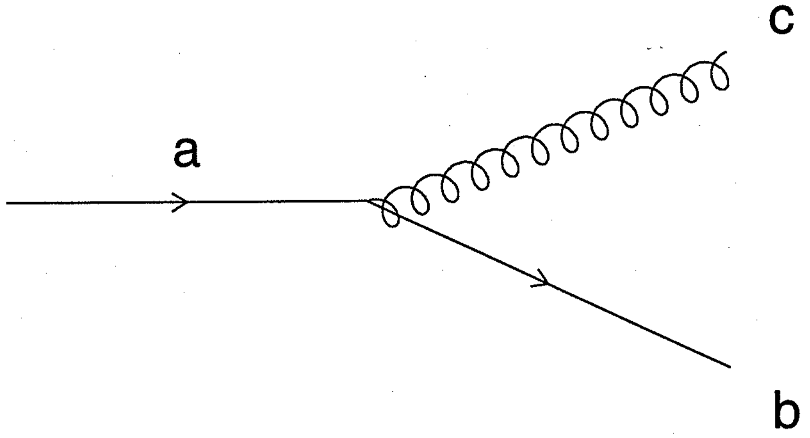

Figure 2.5: The parton branching process $a \to bc$.

The probability $\mathcal{P}$ that a branching $a \to bc$ as shown in figure 2.5 will take place during a small change $dt = dQ^2_{evol}/Q^2_{evol}$ of the evolution parameter $t = \ln Q^2_{evol}/\Lambda^2$ is given by Altarelli-Parisi equations [11]

$$\frac{d\mathcal{P}_{a\to bc}}{dt} = \int dz \frac{\alpha_s(Q^2)}{2\pi} P_{a\to bc}(z)$$

For gluons, it is necessary to sum over all allowed final state flavour combinations b and c to obtain the total branching probability. The $P_{a\to bc}(z)$ are the Altarelli-Parisi splitting kernels,

$$\begin{aligned}P_{q\to qg}(z) &= C_F\frac{1+z^2}{1-z}\\ P_{g\to gg}(z) &= N_C\frac{(1-z(1-z))^2}{z(1-z)}\\ P_{g\to q\bar{q}}(z) &= T_R(z^2+(1-z)^2)\end{aligned}$$

with $C_F = 4/3$, $N_C = 3$ and $T_R = N_f/2$. The z variable specifies the sharing of four-momentum between the daughters, with daughter b taking fraction z and c taking $1-z$.

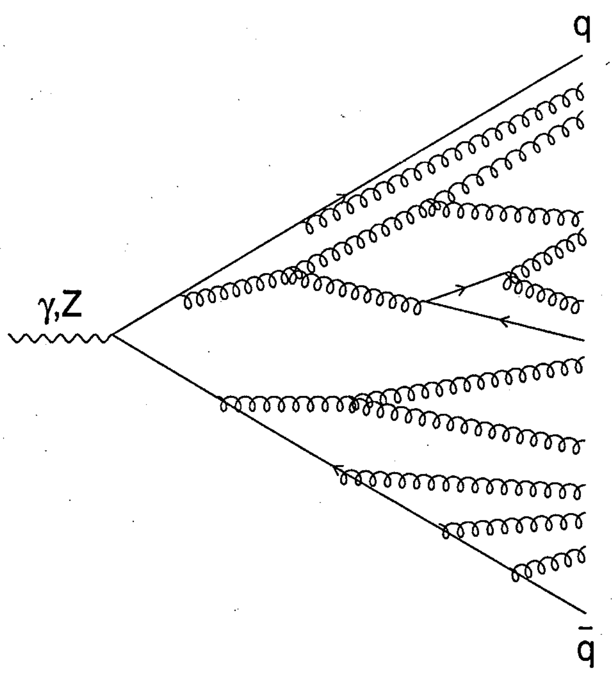

Figure 2.6: One possible configuration of the leading log parton shower evolution in e^+e^- interactions.

2.3.5 Fragmentation

During a hard collision, the partons can be regarded as free. But colour forces organise them into colourless hadrons as the system evolves. *Fragmentation* describes the conversion of coloured partons into hadrons. This involves creation of additional $q\bar{q}$ pairs by the colour force field. The initial parton configuration governs the contribution of fragmentation towards the complete process. Fragmentation is governed by soft non-perturbative processes that cannot be described from the first principle, starting from the QCD Lagrangian.

There are essentially three models which are used to describe fragmentation.

Independent Fragmentation

The independent fragmentation model [12] assumes that the fragmentation of any system of partons can be described as an incoherent sum of independent fragmentation procedures for each parton separately. Each parton gives rise to its own jet of hadrons. The process is to be carried out in the overall centre of mass frame of the jet system, with each jet fragmentation axis given by the direction of motion of the corresponding parton in that frame. The fragmentation process can be viewed as an iterative procedure, where an initial quark picks up an antiquark from a vacuum fluctuation to form a meson leaving behind the other quark. The sharing of momentum between the meson and the remaining quark is described by a fragmentation function f(z), which is the probability density for the meson to carry a fraction z of the initial quark momentum. The remaining quark carries the momentum fraction $1 - z$. Transverse momentum components are introduced according to a gaussian distribution with zero mean and a standard deviation of typically 300 MeV. The procedure is repeated with the remaining quark, until the energy falls below a cutoff. Gluons can be treated by splitting them into a quark-antiquark pair first and then following the same mechanism as described above for hadron production.

Independent fragmentation models have been widely used at PEP [5] and PETRA [6]. They have become less important with the discovery of string effect [13] which these models fail to explain.

String Fragmentation

The string fragmentation model [14] is based on the idea that, as the partons ($q\bar{q}$ pair) produced in the e^+e^- interactions move apart, a colour flux tube (string) is stretched between the q and the $\bar{q}$. The transverse dimension of the tube is of the typical hadronic size, roughly 1 fm which provides a natural scale for the creation of transverse momenta. For a $q\bar{q}g$ system, where all the partons are moving from a common origin, a string is stretched from the q end via the g to the $\bar{q}$ end. In other words, the gluon can be seen as a kink on the string, as shown in figure 2.7, which carries energy and momentum. As a consequence, a gluon has two string segments attached to it.

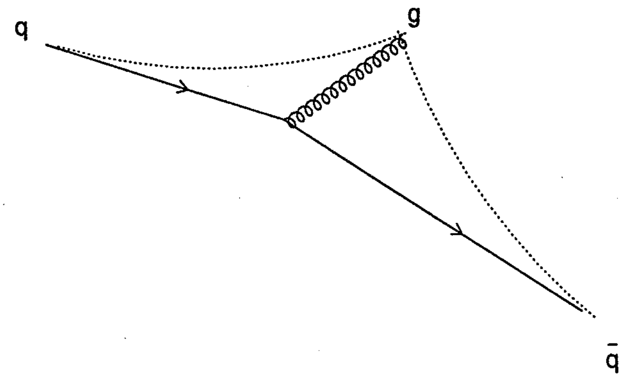

Figure 2.7: String representation of a $q\bar{q}g$ system. For such a system where all the partons move apart from a common origin a string is stretched from the q end via the g to the $\bar{q}$ end.

If several gluons are present in the system, they will still appear as kinks between the q and $\bar{q}$ ends, although the configuration will be much more complicated. When two partons connected with a string segment have a small invariant mass, two such nearby partons together drag out a string very much like what would have been dragged out by one single parton with the summed momentum. A soft gluon does not affect the string evolution significantly. These properties of the string motion are the reasons why the string fragmentation scheme is safe with respect to soft or collinear gluon emission.

When the partons move apart, the potential energy stored in the string increases, and the string may break producing a new quark-antiquark pair at a point when the energy density reaches about 1 GeV/fm. Thus the system splits into two colour singlet quark-antiquark pairs. If the invariant mass of either of these string segments is large enough, strings pieces may break further. The quarks and antiquarks from adjacent branches can then form mesons. Baryon formation is also possible via di-quark production (1:10^9). Finally only on-shell hadrons remain in the spectrum, each hadron corresponding to a small piece of string.

Cluster Fragmentation

Cluster fragmentation [15] is used only for developed parton configuration. The clusters are considered to be the basic units from which the hadrons are produced. A cluster does not have an internal structure and is characterised by its total mass and total flavour content. No explicit assumptions about fragmentation functions and the generation of transverse momenta are required. The decay of the cluster is assumed to be isotropic in the rest frame of the cluster. There are different clusters fragmentation schemes which differ to the extent to which string fragmentation ideas are incorporated.

- a parton shower picture is used to produce a partonic configuration. At the end of the shower evolution, all the remaining gluons are split into $q\bar{q}$ pairs. The quark from one splitting may combine with the antiquark which is close in phase space to form a colourless cluster as shown in figure 2.8. These clusters subsequently decay isotropically into observable hadrons according to flavour content and phase space.

  There is basically only one free parameter, the maximum cluster mass. Clusters with higher mass first decay into smaller clusters, which subsequently decay into hadrons.

- parton showers or matrix elements are used to generate a partonic configuration, with string stretched in between the partons. These strings subsequently fragment into clusters, which again decay into the final hadrons.

2.4 Event Shape Variables

Many variables can be defined which are sensitive to the radiation of hard gluons from quarks. Observables which describe the topology of hadronic events are known as event

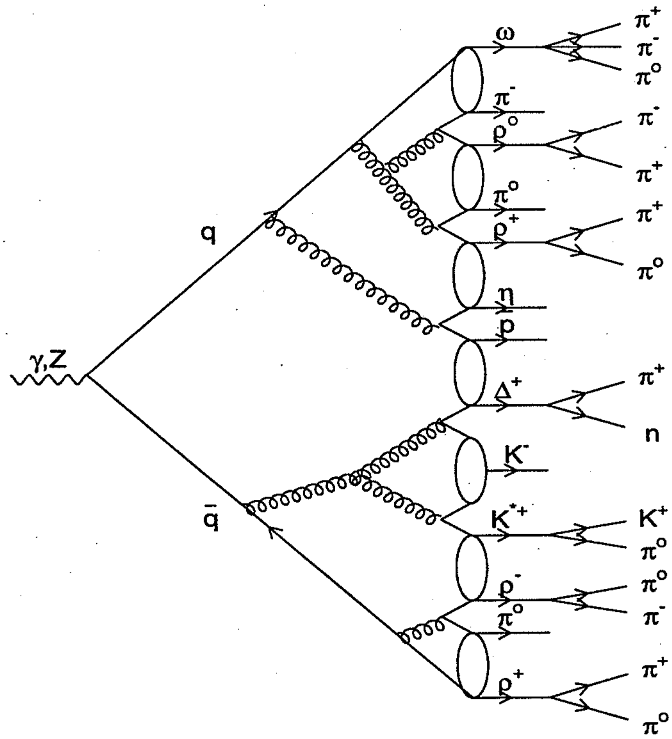

Figure 2.8: One cluster fragmentation scenario. Shower evolution is followed by forced $g \to q\bar{q}$ branchings and formation of clusters which decay subsequently into hadrons. Occasionally a cluster is associated with a single particle.

shape variables. In order to be finite order-by-order in perturbation theory, after renormalisation of ultraviolet divergences, an observable should be both collinear and infrared safe. This implies that the observable should be insensitive to the emission of soft particles and to the splitting of one particle into two collinear ones. In other words, the observable should depend linearly on final state momenta. Apart from the theoretical arguments, infrared and collinear safe variables are also preferred for experimental reasons. They allow calorimetric measurements, and adding a soft particle or splitting a particle into two with half the energy, changes the measurement in a continuous way.

Different event shape variables have different sensitivities to fragmentation and higher order perturbative effects. Therefore, an important estimate of theoretical uncertainties can be made by comparing the values of a physical parameter, α_s for instance, derived from different observables.

- One of the earliest variables is the maximum directed momentum or *thrust* (T) [16] defined as

$$T = \max \frac{\sum_a |\vec{p}_a \cdot \vec{n}_T|}{\sum_a |\vec{p}_a|}$$

where the sum runs over all the final state particles a with momentum vector $\vec{p}_a$. The thrust axis, $\vec{n}_T$, is the unit vector which maximises the above expression.

For two particle final states, thrust is 1, while for events with three and four particles in the final state thrust lies in the range $\frac{2}{3} \leq T \leq 1$, and $\frac{1}{\sqrt{3}} \leq T \leq 1$ respectively. For an arbitrary number of particles in the final states $\frac{1}{2} \leq T \leq 1$. The thrust distribution is thus discontinuous with respect to the multiplicity in the final state. Since multiplicity is an infrared sensitive quantity, some amount of smearing is necessary around the kinematical boundaries.

It is evident from the definition that thrust is an infrared and collinear safe quantity. Thus the cross section

$$\sigma(\tau) = \int_{1-\tau}^{1} \frac{d\sigma}{dT} dT$$

is finite order-by-order in QCD perturbation theory and the experimental data on this quantity after correction for detector and hadronisation effects should be directly comparable with perturbative calculations at the parton level.

The perturbative prediction of the thrust distribution has the form

$$\frac{1}{\sigma}\frac{d\sigma}{dT} = \alpha_s A_1(T) + \alpha_s{}^2 A_2(T) + \alpha_s{}^2 A_3(T) + \dots \quad ,$$

where $A_1(T)$ and $A_2(T)$ are completely known, i.e exact perturbative predictions exist up to $\mathcal{O}(\alpha_s{}^2)$. A fit to the data (suitably corrected for detector and hadronisation effects) neglecting the higher order terms yields a measured value of the strong coupling constant, α_s. As long as thrust is not too large, the fixed order perturbative calculations should be reliable. Near two jet region (at large values of thrust), where the statistics is high, however, there are terms in higher order that become enhanced by powers of $\ln(1-T)$. In this kinematical region the perturbative coefficients become

$$A_n(T) \underset{T\to 1}{\sim} \frac{\ln^{2n-1}(1-T)}{1-T}.$$

The real expansion parameter in the perturbative series is the large effective coupling $\alpha_s \ln^2(1-T)$. Thus for the higher orders to be negligible, it is not sufficient to have just $\alpha_s \ll 1$. We also require the effective coupling $\alpha_s \ln^2(1-T) \ll 1$. Any fixed order perturbative calculation cannot, therefore, give accurate estimation of the cross section. The explicit large logarithm terms in each order of perturbation theory need to be identified and resummed to all orders in α_s before a reliable prediction can be made. The resummation is most effective when the logarithm terms exponentiate, i.e. when they combine in such a way that the logarithm of the cross section is less divergent in the two jet limit. We shall discuss exponentiation and resummation of large logarithms in detail in Chapter 8 for a few global event shape variables for which such calculations exist.

- *Major* (T_{major}) is defined in the same way as thrust but maximising the expression

$$T_{major} = \max \frac{\sum_a |\vec{p}_a \cdot \vec{n}_{major}|}{\sum_a |\vec{p}_a|}$$

in a plane perpendicular to the thrust axis. The resulting direction is known as the major axis, $\vec{n}_{major}$. An orthogonal system is constructed to describe the spatial distribution of the energy flow by defining the minor axis as

$$\vec{n}_{minor} = \vec{n}_T \times \vec{n}_{major}$$

The resulting quantity is called *minor* (T_{minor}). *Oblateness* (O) [17] is the difference of the major and the minor values,

$$O = T_{major} - T_{minor}$$

For collinear and spherical events oblateness vanishes. It is large for planar configuration. For 3 particle configuration $O < \frac{1}{\sqrt{3}}$. For planar four particle events the maximal value of oblateness is $\frac{1}{\sqrt{2}}$.

- After dividing an event into two hemispheres by a plane perpendicular to the thrust axis, the transverse momentum fraction

$$f_T = \frac{\sum_a |\vec{p}_a \times \vec{n}_T|}{\sum_a |\vec{p}_a|}$$

is calculated for each hemisphere. The hemisphere with the smaller f_T is called the narrow side and the minor derived from the particles in this hemisphere is called the *minor of the narrow side*, (T^{NS}_{minor}) [18].

- The heavy jet mass (M_H), [19] is defined as

$$M_H = \max[M_+(\vec{n}_T), M_-(\vec{n}_T)]$$

where $M_\pm$ are the invariant masses in the two hemispheres, $S_\pm$, defined by dividing the event by a plane normal to the thrust axis, n_T,

$$M^2_\pm = \left(\sum_{a \in S_\pm} p_a\right)^2.$$

Here p_a is the four momentum of particle a. The scaled heavy jet mass (ρ) is defined as

$$\rho = M_H^2/s$$

where $\sqrt{s}$ is the centre of mass energy. We define the light jet mass as

$$M_L = \min[M_+(\vec{n}_T), M_-(\vec{n}_T)]$$

and write the scaled light jet mass (ρ_L)in the following form:

$$\rho_L = M_H^2/s$$

- The l^{th} order *Fox-Wolfram moment* [20] is defined as

$$H_l = \sum_{a,b} \frac{|\vec{p_a}||\vec{p_b}|}{s} P_l(\cos\theta_{ab})$$

  where P_l are the Legendre polynomials, p_a and p_b are the momenta of the particles a and b respectively and θ_{ab} is the angle between them. The sum runs over all the particles in the final state. The second (H_2), third (H_3) and fourth (H_4) Fox-Wolfram moments correspond to $l=2$, $l=3$ and $l=4$ respectively.

- Jets are reconstructed using different jet clustering algorithms. The JADE algorithm [21] uses invariant mass of a pair of particles while the DURHAM algorithm [22] uses scaled transverse momentum of the softer particle with respect to the other in a pair to define the jet resolution or closeness variable. For each pair of particles a and b, the closeness variable y_{ab} is defined as

$$y_{ab}^{JADE} = \frac{2E_aE_b}{\sqrt{s}}(1 - \cos\theta_{ab})$$

  for JADE, and as

$$y_{ab}^{DURHAM} = 2\frac{\min(E_a^2, E_b^2)}{\sqrt{s}}(1 - \cos\theta_{ab})$$

  for DURHAM algorithms. Here E_a and E_b are the energies of the particles, θ_{ab} is the angle between them and $\sqrt{s}$ is the centre of mass energy. The pair with the smallest value of the jet resolution variable is replaced by a pseudo-particle c with 4-momentum

$$p_c = p_a + p_b$$

  This procedure is repeated until all $y_{ab}^{JADE}(y_{ab}^{DURHAM})$ exceed a predefined jet resolution parameter y_{cut}. The pseudo-particles at the end of this recombination procedure are called jets. The maximum jet resolution parameter for which the event still has 3 jet structure is known as 3-jet resolution parameter, and denoted by y_{23}^{JADE} for JADE and y_{23}^{DURHAM} for DURHAM algorithms.

In JADE algorithm two soft particles with small invariant mass can combine even if they are far apart in angular distance. This makes the algorithm inadequate in cases where resummation of the contributions of soft and collinear gluon emissions is important. Durham jet algorithm avoids the above mentioned drawback of the JADE algorithm as transverse momentum of one particle with respect to the other.

- For each event we define the normalised momentum tensor M_{ij} as

$$M_{ij} = \frac{\sum_a p_a^i p_a^j}{\sum_a p_a^2}$$

where i and j run over three space dimensions and p_a is the momentum of particle a, summed over final state particles a in the event. M_{ij} is a symmetric matrix can can be diagonalised, with unit eigenvector n_j, and eigenvalues Q_j that are normalised and ordered by

$$Q_1 + Q_2 + Q_3 = 1 \qquad 0 \leq Q_1 \leq Q_2 \leq Q_3$$

The *sphericity*, S and *aplanarity*, A [23] are defined as

$$S = \frac{3}{2}(Q_1 + Q_2) \qquad A = \frac{3}{2}Q_1$$

Sphericity lies in the range $0 \leq S \leq 1$. Events with $S \approx 1$ are spherical whereas those with $S \ll 1$ look like a pair of back-to-back jets. Aplanarity lies in the range $0 \leq A \leq \frac{1}{2}$. A is small for coplanar events. The momentum tensor M_{ij} is intrinsically collinear unsafe because it has a quadratic dependence on particle momenta. So are sphericity and aplanarity.

- *C parameter* [24] is defined from the eigenvalues of the infrared safe momentum tensor

$$\theta^{ij} = \frac{\sum_a p_a^i p_a^j / |p_a|}{\sum_a |p_a|}$$

where the sum on a runs over all the final state hadrons, and p_a^i is the i^{th} component of the three momentum of the hadron a in the centre of mass system. The tensor θ is normalised to have unit trace. In terms of eigenvalues of θ^{ij}, $\lambda_{1,2,3}$, the *C and D parameters* are defined as

$$\begin{aligned} C &= 3(\lambda_1\lambda_2 + \lambda_2\lambda_3 + \lambda_3\lambda_1) \\ D &= 27\,\lambda_1\lambda_2\lambda_3 \end{aligned}$$

For two particle final state both C and D parameters vanish, while for three particle final state C ranges between 0 and 2/3 and D = 0. For larger number of particles in the final state C can extend its value up to 1.

- Both thrust and scaled heavy jet mass are sensitive to the longitudinal structure of jets and the resummed expressions are similar. It would be very desirable to have resummed predictions for event shape variables which are less correlated and hence complementary to thrust and scaled heavy jet mass. Event shape variables which are sensitive to the transverse development of jet are in particular interesting. For e^+e^- interactions, the jet broadening [25] variables are defined by dividing the event in two hemispheres $S_\pm$ by a plane perpendicular to the thrust axis, and computing in each hemisphere the quantity

$$B_\pm = \frac{\sum_{a \in S_\pm} |\vec{p}_a \times \vec{n}_T|}{2\sum_a |\vec{p}_a|}$$

The sum in the denominator runs over all final state particles, while that in the numerator runs over particles in one hemisphere. The observables, total (B_T) and wide (B_W) jet broadening, are then defined respectively as

$$\begin{aligned} B_T &= B_+ + B_- \\ B_W &= \max(B_+, B_-) \end{aligned}$$

To leading order in α_s, $B_T = B_W = \frac{1}{2}\,O$, where O is the oblateness. Both B_T and B_W tend to zero in the two jet region.

2.5 Final State Photon Radiation From Quarks

Final state photon radiation from quarks provides a powerful tool to probe the parton development of a hadronic event. Once a quark-antiquark pair has been formed from the hard process $e^+e^- \to q\bar{q}$, the quark and antiquark may radiate both gluons and photons. The two basic branchings $q \to qg$ and $q \to q\gamma$ have similar structures and appear as competing processes. The probability of a quark to branch at some given virtuality scale Q^2, with the daughter quark retaining a fraction z of the mother energy, is given by

$$d\mathcal{P} = \left\{ \frac{\alpha_s}{2\pi} C_F + \frac{\alpha}{2\pi} \langle e_q^2 \rangle \right\} \frac{dQ^2}{Q^2} \frac{1+z^2}{1-z} dz.$$

Here the first term corresponds to gluon emission and the second to photon emission. The average squared charge, $\langle e_q^2 \rangle$ is given for the standard LEP flavour mixing. α_s is the typical first order value used in QCD shower description while α is the electromagnetic coupling constant and C_F is the QCD colour factor. The relative probability for a photon emission against a gluon emission is given by the ratio

$$\frac{\mathcal{P}_{q\to q\gamma}}{\mathcal{P}_{q\to qg}} = \frac{\alpha\langle e_q^2\rangle}{\alpha_s C_F} \approx \frac{\frac{1}{137}0.22}{0.25\frac{4}{3}} \approx \frac{1}{200}$$

The photon emission is, therefore, strongly suppressed against gluon emission.

While the coupling strengths of photon and gluon radiation differ, the dynamics are similar. The radiated photon is typically of low energy and produced at a small angle with respect to the quark. These photons cannot be identified from the other inclusive photons. But if an energetic and isolated photon is emitted, presumably before the first gluon branching, this could be detected.

The difference between a photon and a gluon emission constitutes the fact that a gluon may further branch through either of the processes g$\to$gg and g $\to$ q$\bar{\text{q}}$, but due to a smaller value of the electromagnetic coupling constant further branching of the photon would be infrequent at the centre of mass energy we consider here. One can choose the lower cut off (Q_o) for shower evolution separately for gluon and photon emission.

Figures 2.9, 2.10 and 2.11 show the leading order Feynman diagrams which contribute to the $q\bar{q}\gamma$ and $q\bar{q}\gamma g$ final states.

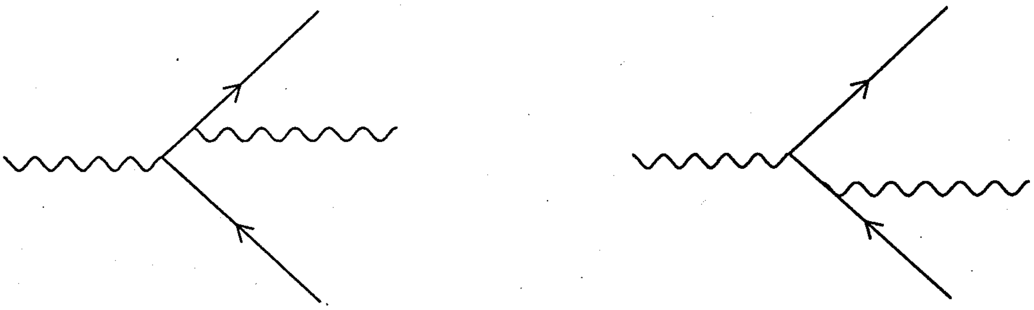

Figure 2.9: Lowest order diagram for the process $Z \to q\bar{q}\gamma$.

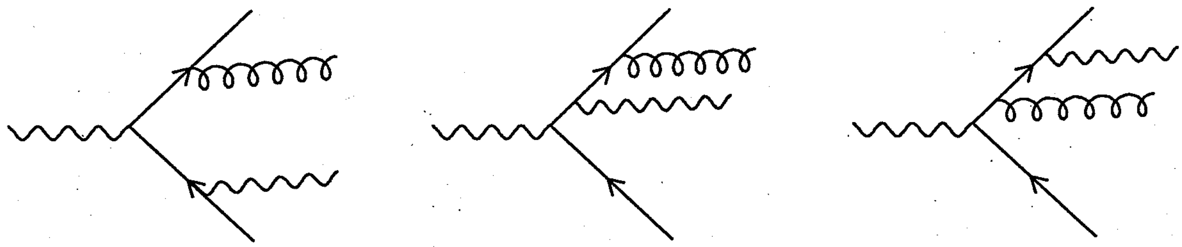

Figure 2.10: Leading order QCD diagrams for the process Z $\rightarrow$ q$\bar{q}$gγ. The complete set of diagrams are obtained by interchanging quark and antiquark legs.

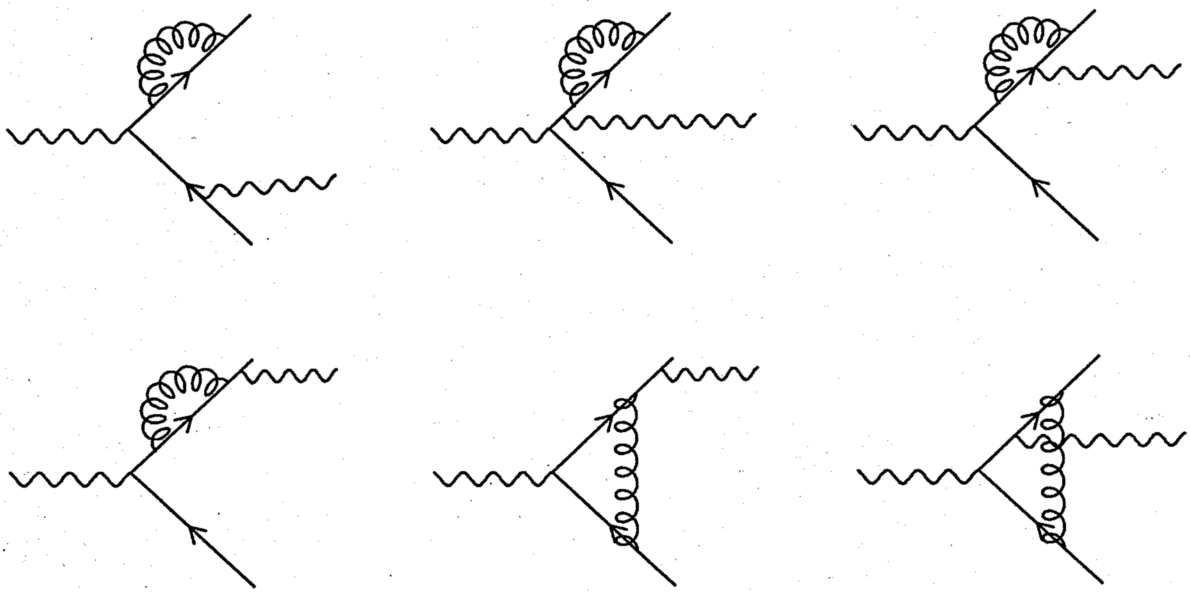

Figure 2.11: Leading order QCD diagrams for the process Z $\rightarrow$ q$\bar{q}\gamma$. The complete set of diagrams includes diagrams obtained by interchanging quark and antiquark legs.

Chapter 3

The L3 Experiment

3.1 The Large Electron Positron Collider

The Large Electron Positron (LEP) collider is an e^+e^- accelerator and storage ring designed to operate at centre of mass energies in the range $100 - 200$ GeV. The LEP accelerator ring, shown in figure 3.1, is equipped with four detectors ALEPH [26], DELPHI [27], L3 [28], and OPAL [29], at four out of eight selected interaction points. In the first phase of its running, LEP has operated at centre of mass energies around 91 GeV. LEP energy has been increased during the second phase so that W pair production is kinematically possible.

The LEP storage ring is an octagonal polygon with eight straight sections, each about 500 m long, and eight circular arcs with a radius of curvature of 3300 m. The ring is located in an underground tunnel with a circumference of 26.7 km at varying depth, from a minimum of 50 to a maximum of 150 m.

The various stages of the LEP injection system is shown in figure 3.2. Electrons from an electron gun are accelerated to 200 MeV in a high current linear accelerator (LINAC) and then directed towards a tungsten target to produce positrons through bremsstrahlung followed by pair production. These positrons and also electrons are accelerated to 600 MeV by a second LINAC and then stored in the electron positron accumulator (EPA). The electron positron accumulator condenses the beams into bunches through synchrotron radiation damping. The bunches are then accelerated to 3.5 GeV in the proton synchrotron (PS) and then to 20 GeV in the super proton synchrotron (SPS), after which they are injected in the main LEP ring. LEP accelerates the electron and positron beams to the required energy and then operates as a storage ring. Energy for acceleration and for compensation of losses due to synchrotron radiation ($\approx$ 120 MeV per turn for beam energy of 45 GeV, for instance) is provided by radio frequency cavities. The cavities were initially made out of copper and subsequently replaced by super conducting cavities made of niobium-tin.

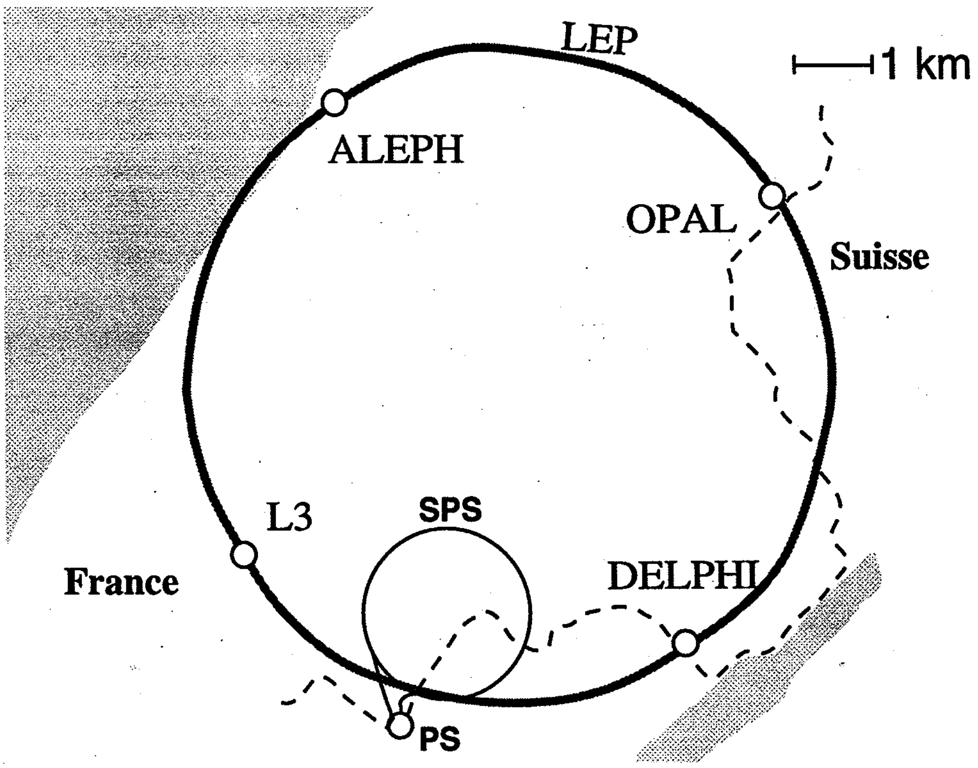

Figure 3.1: Perspective view of the LEP collider.

The two fundamental parameters in the design of any particle collider are the beam energy and the luminosity. The beam energy must be sufficient to allow observation of the physics processes of interest. The luminosity must be enough to permit such observations at a reasonable rate. At LEP the beam energy has been dictated by the energy required for the production of on-shell Z in the first phase of its operation and of W^+W^- pair in the next phase. For a collider experiment, luminosity is defined as the rate of collisions at the interaction point and is given by

$$\mathcal{L} = \frac{N_e N_p n_b f_{rev}}{4\pi\sigma_x\sigma_y},$$

where N_e (N_p) is the number of electrons (positrons) per bunch, n_b is the number of bunches per beam, f_{rev} is the revolution frequency and σ_x (σ_y) is the transverse beam size in the (perpendicular to the) beam plane. The design luminosity of LEP is 1.7 $\times 10^{31}\mathrm{cm}^{-2}\mathrm{s}^{-1}$ for $E_{CM} \simeq 91$ GeV.

The luminosity can be increased most effectively by increasing the number of bunches. LEP operated in the four bunch per beam mode from 1989 to 1991. The optics were then upgraded to use a *Pretzel Scheme* [30], between 1992 and 1994. Pretzel scheme used 8 bunches per beam with a lower current per bunch. Hence an overall increase of about 50% in the average luminosity [31] was achieved. During 1995 LEP operated in the

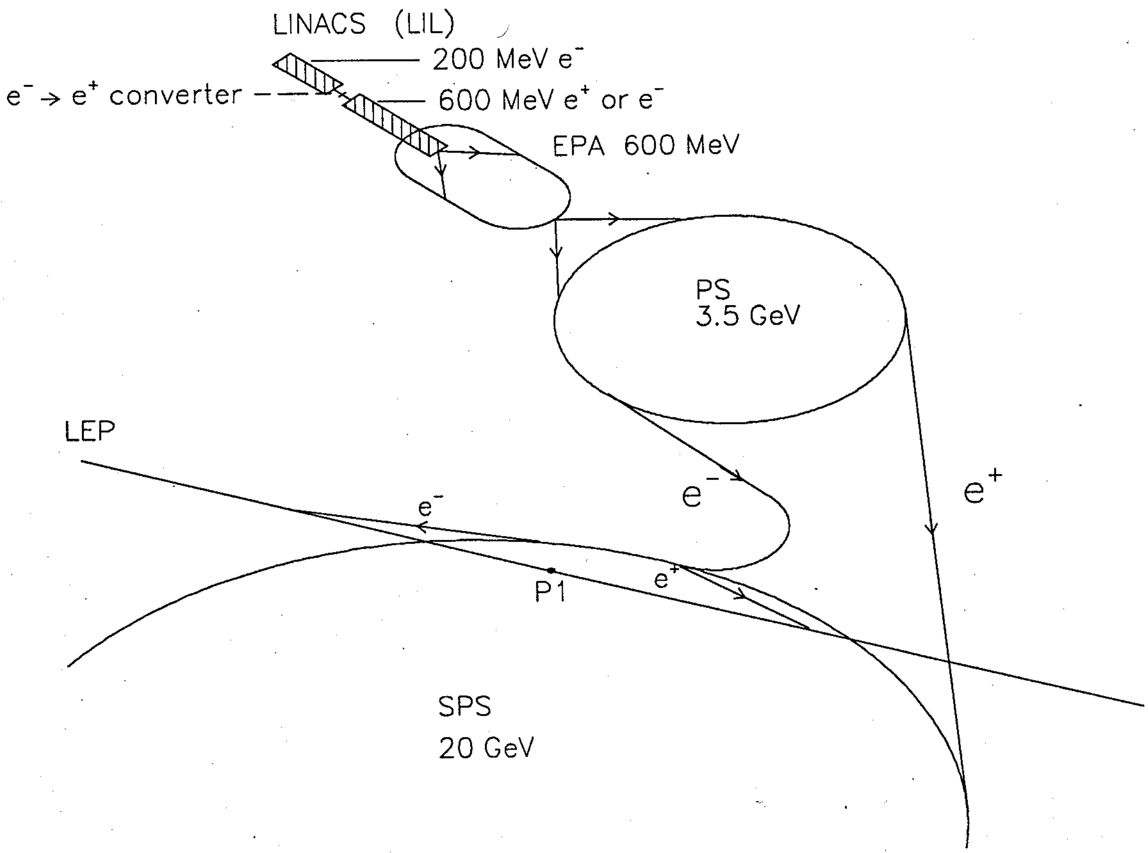

Figure 3.2: Injection scheme for LEP.

bunch train [32] mode which allowed 12+12 bunches to collide at four interaction points. Each bunch train was 220 m long and consisted of three *bunchlets.* Although this scheme is expected to deliver much higher luminosity which would be required for LEP II, the performance in 1995 was not as good as expected. Table 3.1 lists various parameters related to LEP performance, like centre of mass energy (E_{CM}), number of bunches per beam, n_b, integrated luminosity ($\int \mathcal{L}$) delivered at each interaction point, efficiency of LEP, which is defined as the ratio of the number of physics hours realised to the number of physics hours allocated, during the first phase of running of the LEP accelerator. In 1993 and 1995, significant time was spent for energy calibration which was not counted as time in physics.

3.2 L3 Detector

The L3 experiment [28, 33] is installed at the second interaction point of the LEP e^+e^- ring. The detector is 14 m long and has a diameter of 16 m. The design goal of the L3

Year	1990	1991	1992	1993	1994	1995
E_{CM} (GeV)	88.23–94.22	88.48–93.72	91.29	89.45–93.03	91.22	89.45–92.98
n_b	4+4	4+4	4+4,8+8	8+8	8+8	12+12
$\int \mathcal{L}$ pb^{-1}	7.6	17.3	28.6	40.0	64.4	39.9
Efficiency (%)	42	45	51	55	59	46

Table 3.1: The performance of LEP from 1990 to 1995.

detector is to study e^+e^- collisions in the energy range 100−200 GeV. The detector design emphasises on measurements of energy of electrons, photons and momentum of muons with high resolution. The full view of the detector is shown in figure 3.3. The L3 detector consists of the following components,

- central tracking system
  - time expansion chamber (TEC) to determine momenta and sign of charge of particles and to reconstruct the event vertex,
  - silicon microvertex detector (SMD) in combination with the time expansion chamber to reconstruct secondary vertices,
  - central Z detector to provide precise z measurements along the track giving rise to measurements of the polar angle, θ,
- electromagnetic calorimeter
  - barrel and endcap electromagnetic calorimeters made of Bismuth Germanium Oxide (BGO) crystals to precisely measure the energy and direction of photons and electrons,
  - instrumented (active) lead ring (ALR) for energy measurement of small angle electrons and photons and to trigger two photon processes,
  - electromagnetic gap detector (EGAP) between the barrel and the endcap electromagnetic calorimeters,
  - forward tracking chamber (FTC) for a precise determination of the impact point of charged particles in the endcap electromagnetic calorimeter,
- ring of scintillation counters to provide timing informations of an event,
- hadron calorimeter
  - barrel and endcap hadron calorimeters (HCAL) consisting of uranium absorber with proportional chamber readout to measure jet energies,
  - active muon filter used for energy and coordinate measurements,

- muon spectrometer, consisting of large drift chambers, for precise measurement of muon momenta,
- luminosity monitor (LUMI), to determine luminosity by counting small angle Bhabha events,
- solenoidal and toroidal magnets.

All the subdetectors, but the muon spectrometer, are installed inside a support tube made of steel. The support tube is 32 m long, has an outer diameter of 4.45 m and a thickness of 50 mm which is equivalent to 0.52 nuclear interaction length. The tube is concentric with the LEP beam line and symmetric with respect to the interaction point. The part of the support tube (14.1 m long), which is inside the magnetic field, is made of non-magnetic stainless steel.

The right handed coordinate system used in L3 has its origin in the centre of the detector. The positive z-axis points along the magnetic field which is the same as the electron beam direction. The y-axis points perpendicular to the plane containing the LEP ring whereas the positive x-axis points towards the centre of the ring.

3.2.1 The Magnet

A huge 7800 ton octagonal solenoidal magnet surrounds all the detectors and provides a uniform magnetic field of 0.5 T in a large volume to optimise the muon momentum resolution which improves linearly with the field but quadratically with the track length. Additional 1.5 T toroidal magnets were added to the main magnet doors during 1994.

The solenoidal coil, of inner radius 5.93 m and total length 11.90 m, is made of aluminium plates welded together. Cooling is provided by two independent circuits made of an aluminium alloy which has high resistance to corrosion. The gaps between turns are closed with rubber joints to minimise heat transfer to the detector. An active thermal shield is placed inside the coil to protect the detectors.

The magnetic structure is made of soft iron with 0.5% carbon content. The magnetic field in the inner volume of the support tube was mapped with Hall probes. The field in the remaining volume has been mapped with about one thousand magneto-resistors, permanently installed on the muon chambers. In addition, five NMR probes measure the absolute value of the field.

3.2.2 Central Tracking Detector

The central tracking detector [34] is comprised of the time expansion chamber (TEC), the Z detector, a layer of plastic scintillating fibres (PSF) and the silicon microvertex detector (SMD). Figure 3.4 shows the perspective view of the central tracking detector.

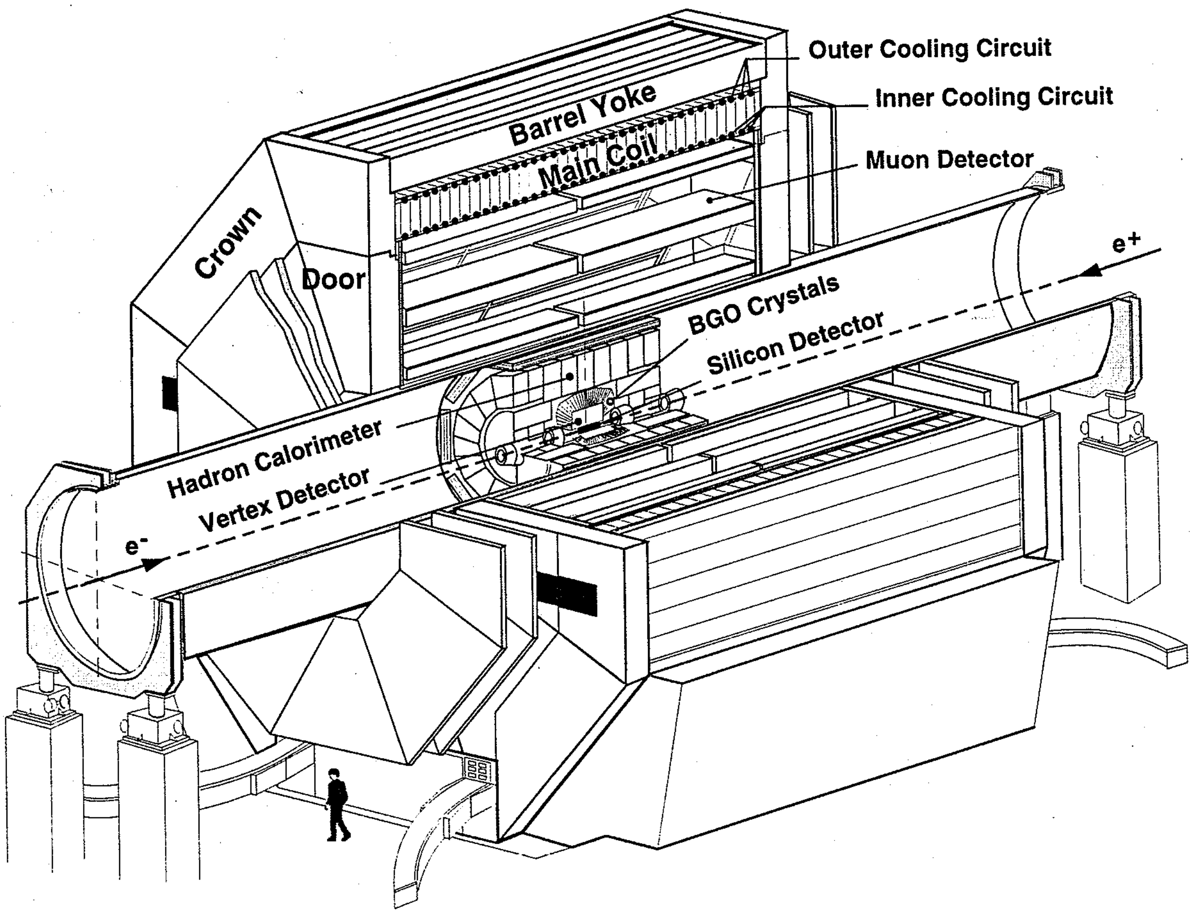

Figure 3.3: Perspective view of the L3 detector showing all the subdetector components, support structure and the magnet.

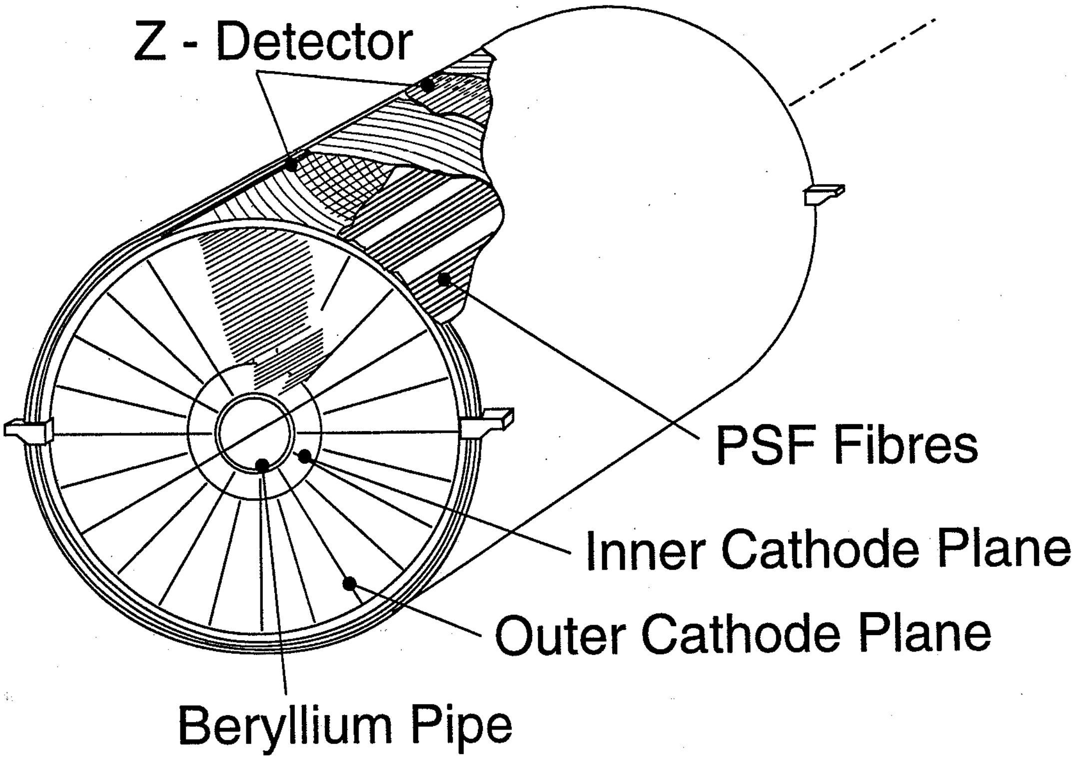

Figure 3.4: General view of the central tracking detector.

Time Expansion Chamber

The time expansion chamber (TEC) consists of two concentric cylindrical drift chambers on common end plates. The chamber operates with a gas mixture of 80% of CO_2 and 20% of *iso*-C_4H_{10}, which has a low longitudinal diffusion and thus permits a low drift speed. Electrons drift at a pressure of 1.2 bar and temperature of 18°C with a velocity of 6 μm/ns. The radial length available inside the TEC volume for track measurement is 31.7 cm. The wires are aligned parallel to the beam direction. The inner and outer chambers of the TEC are subdivided into 12 and 24 ϕ sectors respectively as shown in figure 3.4. Figure 3.5 shows an inner sector and the associated outer sectors of the time expansion chamber. The sectors are separated from each other by cathode planes. The anode plane is located at the middle of each sector. Each inner sector of TEC has 8 anode wires while each outer sector has 54 anode wires allowing for a maximum of 62 coordinate measurements for a single track. Below an angle of 42° the number of wires available for coordinate measurement decreases linearly and at 21° one has only a maximum of 15 wires for coordinate measurement.

The electron drift region in the TEC is divided into a region with uniform and low electric field and an amplification region with a high electric field. The two regions are separated by a plane of grid wires at zero potential. Figure 3.6 shows the drift region of

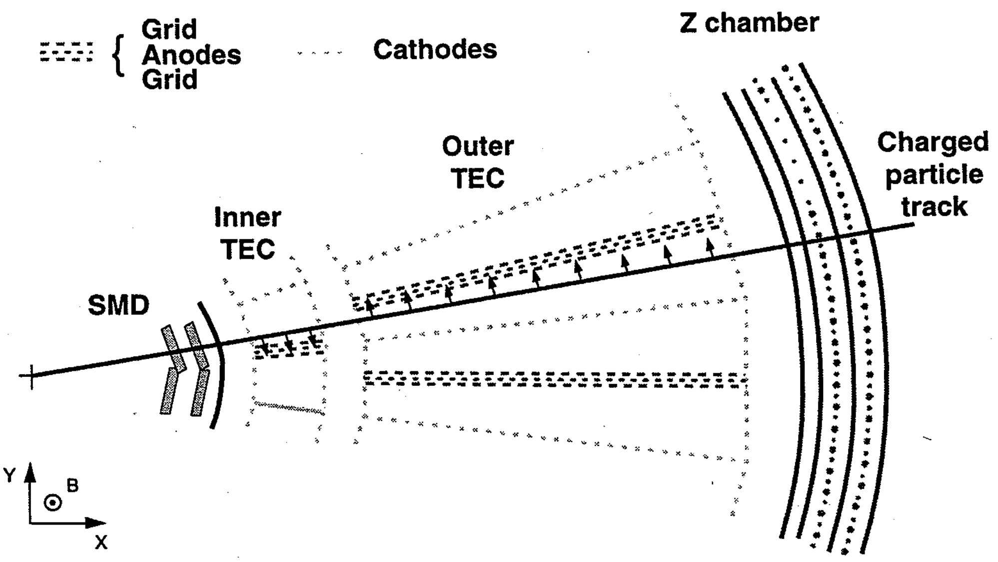

Figure 3.5: Wire configuration in one inner TEC sector and in part of two outer sectors.

the time expansion chamber. The symmetric configuration of TEC minimises the electric field differences between the two half drift regions.

The resolution in the measurement of coordinates of a charged track is $\sim 50\,\mu$m which leads to a resolution in the measurement of transverse momentum of

$$\frac{\sigma(\mathrm{p_T})}{\mathrm{p_T^2}} = 0.02\,(\mathrm{GeV})^{-1}\,.$$

The outer surface of each outer sector of the time expansion chamber is wrapped with a plastic scintillating fibre (PSF) ribbon to monitor the drift velocity. Each ribbon consists of 143 fibres running along z-axis. The drift velocity is measured from the average drift time for each anode wire and the corresponding PSF position.

The Z Detector

The Z detector consists of two cylindrical proportional chambers with cathode strip readout, covering the outer cylinder of the time expansion chamber. The Z detector has an effective length of 1.068 m, an outer radius of 0.49 m and a thickness of 0.0215 m. An 80% argon and 20% CO_2 gas mixture is used for operation in drift mode. The cathode strips are inclined with respect to the z axis by 69° and 90° for the inner chamber, and by −69° and 90° for the outer chamber. Ionisation signals are read out from a total of 920 cathode

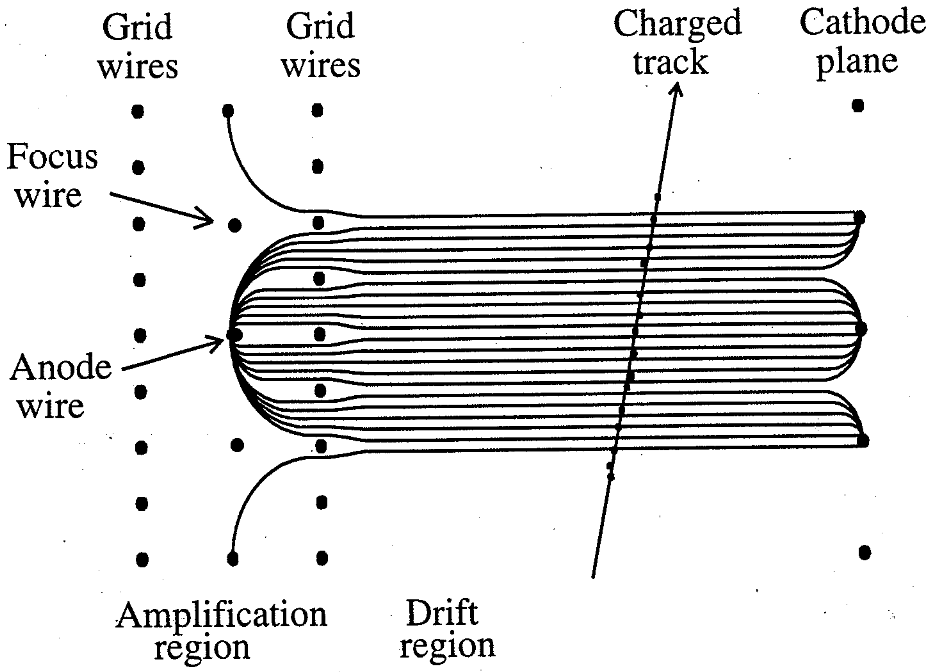

Figure 3.6: Drift region of the time expansion chamber.

strips. The Z detector measures the z coordinate of an isolated track with a resolution of 320 μm.

Silicon Microvertex Detector

The silicon microvertex detector [35] consists of two radial layers of double sided silicon strip detectors at 6 cm and 8 cm respectively from the z-axis as shown in figure 3.7. The detector is 35.5 cm long. The SMD is capable of providing $r-\phi$ and $r-z$ coordinate measurements over polar angular range $|\cos\theta| \leq 0.93$ and over the full azimuth.

The basic detector element of the SMD is built from two electrically and mechanically joined double-sided silicon strip sensors. Each sensor is 70 mm long and 40 mm wide and made from 300 μm thick high purity n-type silicon. The active area of the strips is 70×38.3 mm^2. Half-ladders are built from the silicon strips. Two separate half-ladders, in turn, combine to construct a ladder. There are a total of 24 ladders as shown in figure 3.7. The total number of readout channels is $\sim$ 73000.

The outer silicon surface of each ladder is read out at 50 μm intervals for $r-\phi$ coordinate measurements, and the inner surface is read out at 150 μm (central region) or 200 μm (forward region) intervals for z coordinate measurements. The design resolutions of the silicon microvertex detector are approximately 0.3 mrad in ϕ, and 1 mrad in θ.

The installation of the silicon microvertex detector in 1993 just outside the LEP beam-

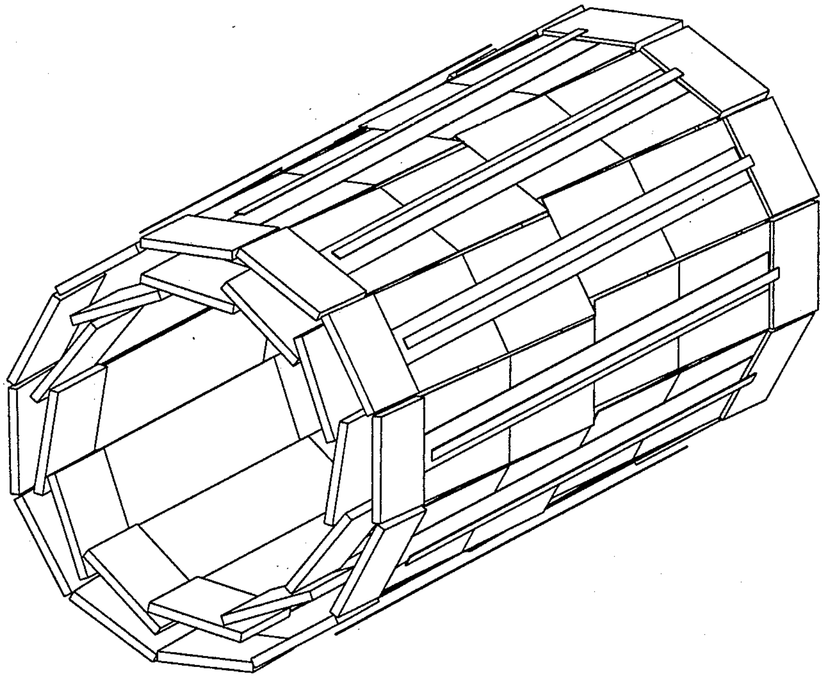

Figure 3.7: Perspective view of the L3 silicon microvertex detector.

pipe surrounding the interaction vertex has significantly enhanced the tracking capabilities of the L3 detector, both in r$-\phi$ and z projections. This has improved the analysing power of the central tracking detector on impact parameter, momentum and z resolution as well as track reconstruction and jet identification capabilities.

The following tasks are accomplished by the tracking detector in a small volume available inside the electromagnetic calorimeter.

- detection of charged particles and precise measurement of the location and direction of their tracks,
- determination of transverse momentum and sign of the charge for particles up to 50 GeV/c,
- reconstruction of the primary vertex and of secondary vertices for particles with lifetimes greater than 10^{-13} s,
- reconstruction of the impact point and direction of charged particles while entering the electromagnetic calorimeter.

3.2.3 Electromagnetic Calorimeter

The electromagnetic calorimeter uses bismuth germanate, $Bi_4Ge_3O_{12}$ (BGO) crystals both as showering and detecting medium. The calorimeter has excellent energy and spatial resolution for electrons and photons over a wide a range of energy, from 100 MeV to 100 GeV. The choice of BGO crystals was dictated by the fact that they have short radiation length and large nuclear interaction length. BGO crystals have reasonable light yield as shown in table 3.2. Moreover, they have low afterglow and are non-hygroscopic.

Density (g/cm^3)	7.13
Radiation length (cm)	1.12
Interaction length (cm)	22
Moliere radius (cm)	2.4
Peak emission wavelength (nm)	480
Light yield (γ/MeV)	$\simeq 2.8 \times 10^3$
Lifetime (μs)	0.35

Table 3.2: Properties of BGO crystals.

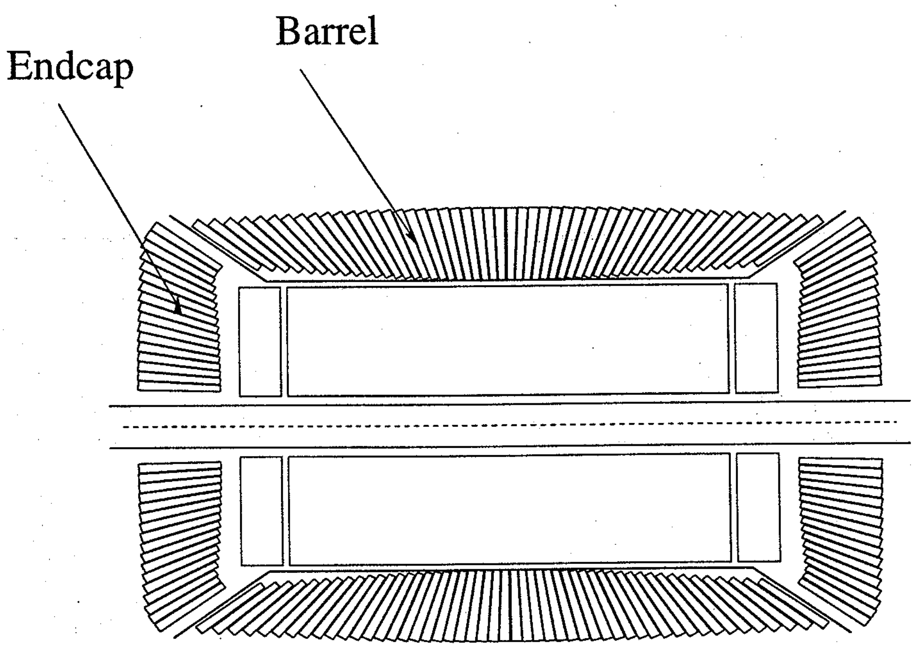

Figure 3.8: Side view of the L3 electromagnetic calorimeter.

The electromagnetic calorimeter consists of 10734 BGO crystals. Each crystal is 24 cm long and has the front and back face dimensions of 2×2 cm^2 and 3×3 cm^2 respectively.

The crystals are tapered and their axes point towards the interaction region with a small angular offset to avoid cracks in the detector. The polished crystals are coated with a 40 to 50 μm thick layer of high reflectivity paint to ensure nearly uniform light collection efficiency.

The detector surrounds the central tracking chamber and consists of two half barrels and two endcaps as shown in figure 3.8. The amount of material in front of the barrel electromagnetic calorimeter is negligible. In the endcap region, however, the material in front amounts to $\sim 1\ X_o$.

The barrel electromagnetic calorimeter is divided into two cylindrical half barrels by the r-ϕ plane. The polar angular coverage of the barrel calorimeter is $42.3° - 137.7°$. The inside radius and length of the barrel are 52 cm and 100 cm respectively. Each half barrel consists of 3840 crystals in 24 rings along z-axis each contaning 160 crystals over the entire azimuthal angular range. There are 24 different crystal shapes in the barrel, corresponding to different θ positions. Each crystal subtends angles with respect to the interaction point of $\Delta\phi = 2.25°$ and $1.5\ ° < \Delta\theta < 2.2°$.

The endcaps are made of two symmetrical parts, each having 1527 crystals. The polar angular coverages of the endcaps are $11.6° < \theta, (180° - \theta) < 38°$. Each endcap is divided into two halves at the y$-$z plane. There are 17 different shapes of crystals in the endcaps. Each crystal subtends angles of $1.68° < \Delta\theta < 7.5°$ and $2.25° < \Delta\phi < 7.5°$ with respect to the interaction region.

Two silicon photodiodes of dimension 1.5 cm^2 detect the scintillation light from the rear face of each crystal. The silicon photodiodes are insensitive to magnetic field and have a quantum efficiency of 70%. A charge sensitive amplifier is mounted directly behind each crystal.

The barrel calorimeter was calibrated in test beams using electrons of energies 0.18, 2, 10, and 50 GeV. The energy resolution obtained is $\approx 5\%$ at 100 MeV, less than 2% above 2 GeV and about 1.2% at 45 GeV as shown in figure 3.9. The linearity is better than 1%. The position resolution determined by the centre of gravity method is ~ 1 mm whereas the angular resolution is ~ 1 mrad for electromagnetic showers at 45 GeV.

Continuous monitoring of the detector is mandatory to maintain the calibration of the BGO which was achieved in beam tests. A Xenon light monitoring system measures the crystal transparency by injecting light pulses into the rear face of each crystal through a network of optical fibres [36]. The absolute calibration is maintained to within 0.9% by combining the results of analysis of Bhabha events together with the information from the Xenon monitor. The minimum ionising signal of muons are also used to obtain absolute energy calibration at low energy [37].

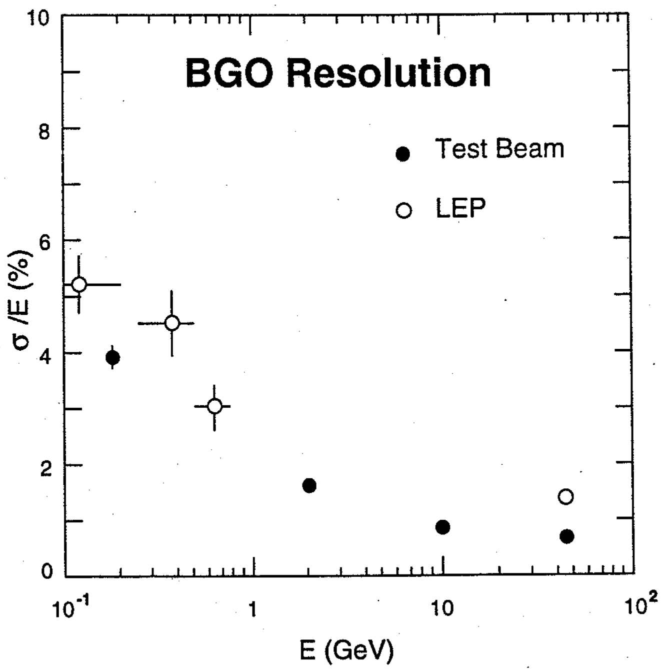

Figure 3.9: Energy resolution of the electromagnetic calorimeter.

Active Lead Ring

The active lead ring (ALR) is located at 108 cm $< |z| <$ 118.4 cm in between the endcap electromagnetic calorimeter and the luminosity monitor. It covers the forward angular regions $4.5° < \theta, (180° - \theta) < 8.8°$. The active lead ring consists of 3 layers of 18.5 mm thick lead followed by 10 mm thick plastic scintillator. Each layer of scintillator is divided into 16 azimuthal segments which are individually read out by photo-diodes. Successive layers are rotated by one third of a segment. The ALR can determine the ϕ coordinates of isolated particles with a resolution of $\approx 1.3°$. With its ability to measure the polar angle as well, the ALR can be efficiently used to trigger the two photon processes.

Electromagnetic GAP Detector

The gap between the barrel and endcap electromagnetic calorimeters has been filled with instrumented blocks of lead threaded with plastic scintillating fibres during the 1995–96 shutdown period of LEP. A better total energy resolution is expected once the detector can be used with full potential.

3.2.4 The Scintillation Counters

The scintillation counter system measures the timing of particles traversing the detector relative to the beam crossing time. The barrel scintillator counter system is located between the barrel electromagnetic and hadron calorimeters. The barrel counter system is comprised of 30 single plastic strips in a cylindrical barrel. Each plastic strip is 2.9 m long and has a thickness of 1 cm. The barrel counter system has a polar angle coverage of $|\cos\theta| < 0.83$ and an azimuthal angular coverage of 93% of 2π. The signal is read out at both ends of a strip with the help of photomultiplier tubes. The barrel scintillation counters are bent to follow the shape of the hadron calorimeter barrel.

Two endcap disks of 16 scintillator sectors were added at $|z| = 103$ cm alongwith the installation of the forward-backward muon chamber system in the beginning of 1995.

A time resolution of 460 ps was achieved using Z decays to muon pairs. The scintillation counters provide an efficient way of discriminating the di-muon events coming from the interaction point and causing two nearly coincident scintillation signals from the cosmic ray muons that cross the detector near the origin, causing scintillation signals that are 5.8 ns apart.

3.2.5 Hadron Calorimeter

The hadron calorimeter [38] is mechanically divided into a barrel, two endcaps, and an active muon filter. Over the full azimuthal angle barrel calorimeter has a polar angular coverage of $35° < \theta < 145°$ whereas the endcaps cover $5.5° < \theta, (180° - \theta) < 35°$. The detector is a fine sampling calorimeter made of uranium plates as an absorber interspersed with proportional chambers (80% Ar + 20% CO_2 mixture) as the active medium. The hadron calorimeter acts as an efficient particle filter due to a very short nuclear absorption length of uranium. Figure 3.10 shows a perspective view of the hadron calorimeter.

Barrel

The modular barrel hadron calorimeter consists of 9 rings along z-axis, each of which is divided symmetrically into 16 modules in ϕ. The innermost ring is centred at the interaction region accompanied by one ring of long modules followed by three rings of short modules on either side. The 4.725 m long hadron calorimeter barrel has an inner radius of 0.885 m for the three inner rings and 0.979 m for the remaining six outer rings while the outer radius of 1.795 m is common to all them.

Each module contains 5 mm thick uranium absorber plates with proportional chambers interleaved in between. Modules of the three central rings contain 60 chambers whereas those of the six outer rings contain 53 chambers. The barrel hadron calorimeter consists of 7968 proportional chambers. Each chamber is made of a plane of brass tubes of equal length with 0.3 mm thick walls and 5×10 mm^2 inner dimensions. The length of the tubes ranges from 347 mm to 605 mm depending on the position of the chamber inside a module. The anode wires in adjacent chamber planes run perpendicular to each other, thus alternately pointing to z and ϕ directions. This arrangement provides a 3-dimensional

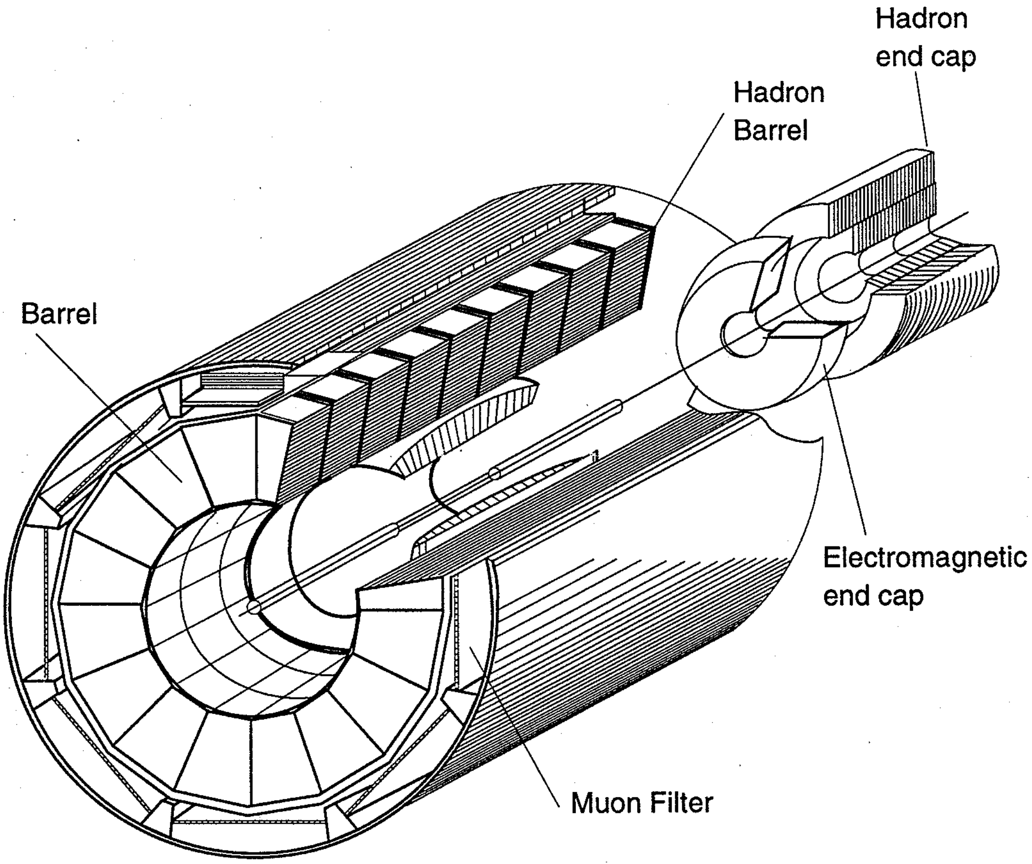

Figure 3.10: Perspective view of the hadron calorimeter.

measurement on the particle trajectories. Towers are formed by grouping the wire signals from each module which include wires from alternate layers. The segmentation is 9 in Φ and z for both kinds of modules and 10 (8) in the radial direction for the long (short) modules. The number of wires in each tower depends on the position of the tower and ranges from 3 to 28. The barrel calorimeter has a total of $\sim$ 370 K wires from which 22 K towers are formed. Each tower typically covers an angular range of $\Delta\theta = 2°$ and $\Delta\phi = 2°$. The granularity is highest at the front end of a module where higher shower densities are expected.

Endcaps

The hadron calorimeter endcaps consist of three separate rings, one outer ring (HC1) and two inner rings (HC2 and HC3). Each ring is split vertically into half-rings, resulting in a total of 12 separate modules. Within a half ring, a chamber layer consists of four full chambers or three full and two half chambers. One full chamber covers an interval $\Delta\phi = 45°$. The wires are stretched azimuthally to measure the polar angle directly. Even numbered layers are rotated by $\Delta\phi = 22.5°$ relative to the odd numbered ones. The wire signals are grouped to form towers pointing to the interaction region. The two endcaps consist of a total of 2284 chambers with 54 K wires which form $\sim$ 4 K towers. Each tower typically covers an angular range of $\Delta\theta = 1°$ and $\Delta\phi = 22.5°$

The solid angle covered by the endcaps (18% of 4π) extends the coverage of the hadron calorimetry to 99.5% of 4π.

Active Muon Filter

The active muon filter [39] is an integral part of the hadron calorimeter. The muon filter is mounted on the inside wall of the support tube and consists of eight identical octants. Each octant is made of six 1 cm thick brass (65% Cu + 35% Zn) absorber plates, interleaved with five layers of proportional chambers which are followed by five 1.5 cm thick brass absorber plates to match the circular shape of the support tube. Each octant is 4 m long, 1.4 m wide and 0.2 m thick in the radial direction. The first four layers of an octant each contains 16 chambers whereas the outermost layer contains 14 chambers. The active muon filter adds on the average 1.03 nuclear interaction length to the hadron calorimeter. The chambers use the same gas mixture as the barrel hadron calorimeter. Total number of readout channels of the active muon filter is 8064.

Energy resolution of hadrons in the calorimeter can be parametrised in the following form:

$$\frac{\Delta \mathrm{E}}{\mathrm{E}} = \frac{55\%}{\sqrt{\mathrm{E}}} \oplus 5\%$$

A total energy resolution of about 10% is obtained for charged pions of energy greater than 15 GeV when one combines informations from hadron and electromagnetic calorimeters. The jet axes can be determined with a resolution of 2.5°.

3.2.6 Muon Spectrometer

The muon spectrometer [40] consists of a barrel muon chamber, the Z chamber and forward backward muon chambers on both sides of the interaction point.

Barrel Muon Chamber

The barrel muon chamber is comprised of two ferris wheels, each having eight independent units (octants). Each octant consists of a special mechanical structure supporting five precision (P) chambers, two in the outer layer (MO), two in the middle layer (MM), and one in the inner layer (MI) as shown in figure 3.11. The barrel muon chamber is situated in between the support tube and the magnet coil. Each of the MO and MI chambers has 16 signal wires to measure coordinates along a track while each MM chamber has 24 signal wires. The precision chambers measure track coordinates in the bending plane. The chambers use a gas mixture of 38.5% ethane and 61.5% argon and operate in drift mode. Each P-chamber contains about 320 signal wires and a total of 3000 wires including field shaping, cathode and grid wires. Each signal wire in the precision chambers measures an x−y coordinate with a resolution of 110−250 μm, depending on the distance to the anode plane.

The resolution in the measurement of transverse momentum depends on (a) the intrinsic resolution of the drift chambers, (b) the multiple scattering of the muon while traversing the spectrometer and (c) the lack of internal alignment of the chamber in a single octant. The design resolution on the measurement of transverse momentum is $\frac{\sigma(p_T)}{p_T^2} \approx 0.004\ (\mathrm{GeV})^{-1}$.

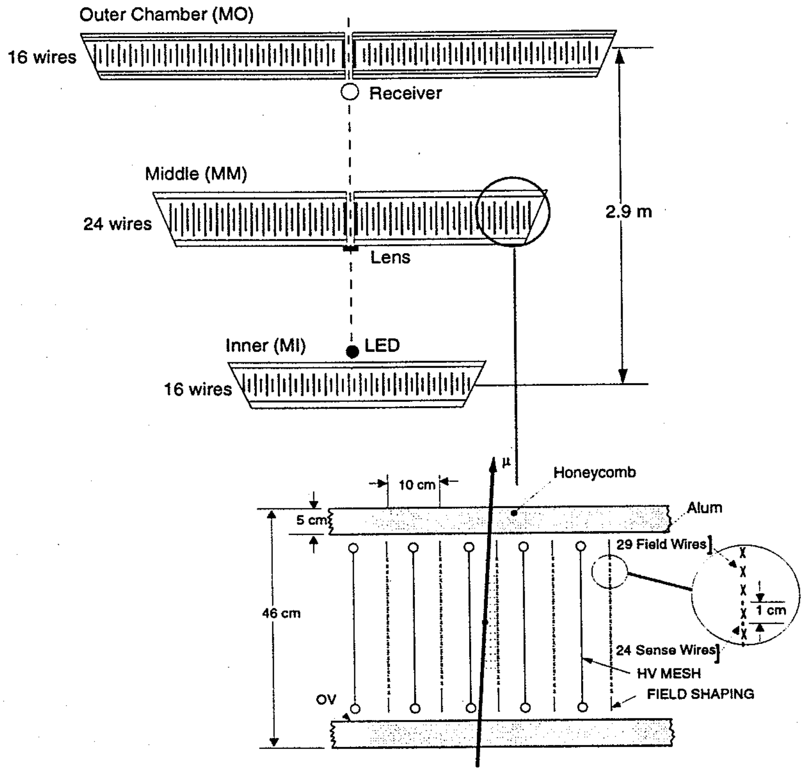

Figure 3.11: An octant of the muon spectrometer.

The Z Chamber

The top and bottom covers of MI and MO are instrumented with drift chambers to measure the z coordinate along the beam. There are a total of six Z chambers per octant each of which has a dimension of 6 $\times$ 2 m^2. The Z chambers consist of two layers of drift cells offset by one half cell with respect to each other to resolve left-right ambiguities. The

Z chamber uses a gas mixture of 91.5% argon and 8.5% methane. The position resolution obtained in the Z chambers is about 500 μm.

Forward Backward Muon Chamber

On either side of the interaction point the forward backward muon chambers [41] are mounted on the magnet doors (figure 3.12). On each side there are three layers, each of which contains 16 drift chambers. The polar angular coverages of the forward backward system are $22° < \theta < 43°$ and $137° < \theta < 158°$.

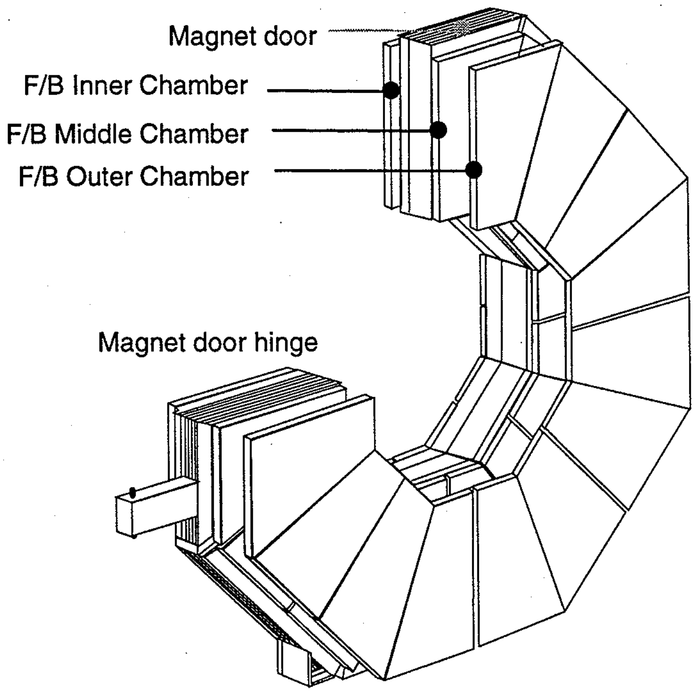

Figure 3.12: perspective view of the Forward backward muon spectrometer.

In the angular range $36° < \theta < 43°$, the muon momentum is measured from 2 central (MI,MM) and 1 inner FB chambers using the curvature in the solenoidal magnetic field. The momentum resolution degrades with θ from 2–20%. Muon momentum in the angular range $22° < \theta < 36°$, is measured using curvature in the toroidal magnetic field in three layers of FB muon chambers. The momentum resolution in this case is 20% for momentum less than 100 GeV, because of the multiple scattering in the 1 m thick magnet doors.

3.2.7 Luminosity Monitor

The luminosity monitor [42] is designed to detect electrons, positrons and photons at very small angles (31–62 mrad from the z-axis) and determine the energy and scattering angles with a high degree of accuracy. These particles mainly come from Bhabha scattering $e^+e^- \rightarrow e^+e^-(\gamma)$ which is dominated by t-channel γ exchange.

The luminosity monitor consists of calorimeter and tracking subsystems on either side of the interaction point at a distance of 2.65–2.80 m.

Each calorimeter consists of cylindrically symmetric array of 304 Bismuth Germanate (BGO) crystals. The crystals are arranged in eight rings each covering 15 mm radially, parallel to the beam pipe. Azimuthally, they are arranged in 16 sectors of 22.5° each. Each sector consists of 19 crystals which are 26 cm long and which range in cross section from 1.5×1.5 cm^2 to 1.5×3.0 cm^2. The BGO calorimeter is split into two halves which are separated during filling of the LEP ring, in order to save the crystals from severe radiation damage. The angular resolution is ~ 0.4 mrad in θ and ~ 0.009 mrad in ϕ.

The tracking system in front of the BGO array consisted of a stack of four planar multiwire proportional chambers with cathode strip readout. The chamber dimensions are $400 \times 200 \times 10$ mm^3 and each stack of four chambers has the cathode strips arranged in both r–ϕ (two chambers) and x–y (two chambers) configurations. In 1993 the above tracking system was replaced by silicon detectors (SLUM) each of which consists of three layers of single-sided sensors. Two of the three layers are concentric with the beam axis to provide the r coordinate while the other layer of strips is perpendicular to the beam axis to measure ϕ.

The combined calorimeter, and SLUM systems have provided an absolute luminosity measurement precise to 0.08% in 1993 and 0.05% in 1994.

One measures the luminosity by comparing the measured rate to theoretical calculation. The precision of luminosity measurement poses one of the main limiting factors in the determination of the electroweak parameters from cross section measurements of e^+e^- annihilation process.

3.3 Trigger System

The online trigger system decides whether an interaction of physics interest has taken place and if so, whether the event should be recorded, after a beam crossing. This operation is carried out in three levels of increasing complexity, reducing the 45 (91) kHz beam crossing rate to a mere 2–3 Hz of tape writing rate. The complexity of the system helps in minimising the dead time for data taking of the experiment. Figure 3.13 schematically shows the different levels of the online L3 trigger system and their performances.

3.3.1 First Level Trigger

The first level trigger consists of independent triggers for central tracking chamber, calorimeters, muon chambers, scintillation counters and luminosity monitor. Each of the individual triggers must take a decision to accept or reject an event within a maximum of 22 (11) μs before the next beam crossing. The combined rate of first level trigger is about 8 Hz. Calorimeter and muon chamber trigger rates are dominated by electronic noise whereas, TEC and luminosity trigger rates are closely related to luminosity. Scintillation counter trigger rate is affected by cosmic ray abundance.

For each beam crossing, informations from all the subdetectors are read by the front end electronics and one has both the main data as well as a less accurate trigger data available in digitised form. The first level trigger analyses the trigger data and either initiates the digitisation of the main data or clears the front end electronics before the next beam crossing. So negative decisions at the first level do not contribute to the dead time. After a positive decision from any of the five individual triggers, however, the system becomes ready for the next beam crossing only after the detector data are digitised and stored in multi-event buffers which takes around 500 μs. So it is the digitisation process which causes the dead time for the data acquisition.

Calorimetric Trigger

The purpose of the first level calorimetric trigger [43] is to select events with energy deposited in the calorimeters. The inputs are the analog sums of energies of several BGO crystals or hadron calorimeter towers. The barrel and endcap BGO crystals are grouped into $32\,\phi \times 16\,\theta = 512$ super blocks. The hadron calorimeter is divided into two radial layers and grouped into 16×11 (16×13) super blocks for the layer less than (greater than) about one absorption length in depth. The event is selected if at least one of the following conditions is satisfied:

- the BGO energy is greater than 25 GeV in the barrel and endcaps,
- the BGO energy is greater than 8 GeV in the barrel alone,
- the total calorimetric energy exceeds 25 GeV in the barrel and endcaps,
- the total calorimetric energy in the barrel exceeds 15 GeV.

The $\theta - \phi$ projections are also used to search for clusters which are accepted with a threshold of 6 GeV. Electronic noise is the main source of background for the first level calorimetric trigger. Typical trigger rate is 1–2 Hz.

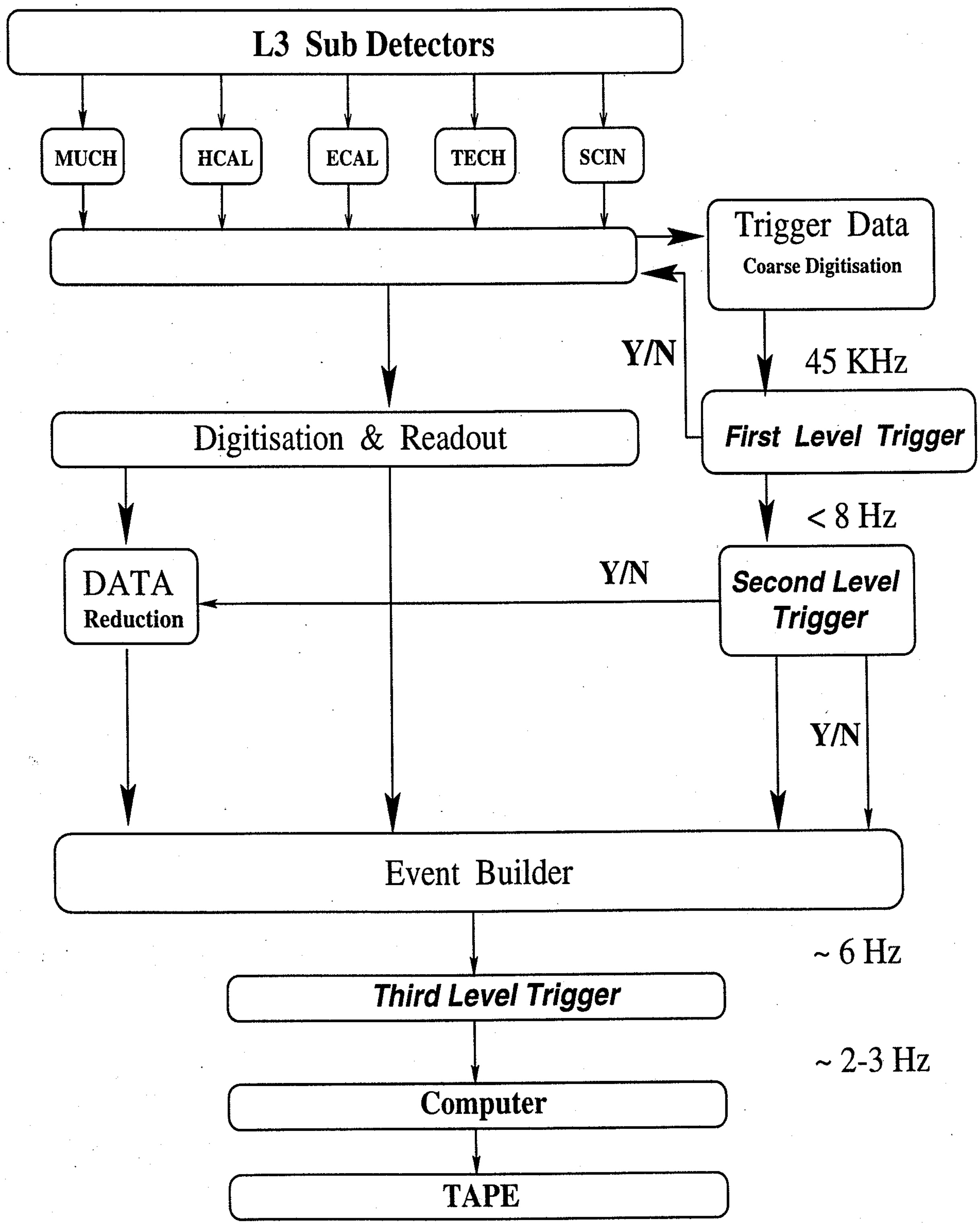

Figure 3.13: Online trigger system of L3.

TEC Trigger

The TEC trigger selects events of physics interest with charged tracks. The input to this trigger is the split off signals from 14 anode wires spread radially over each of the 24 outer sectors of the central tracking detector. Hits found in these signals are divided into 2 equal drift time bins. Logic units then scan each bin and its adjacent bins looking for tracks while allowing for the θ dependent chamber coverage and efficiency. The transverse momentum threshold is 150 MeV. Events where at least two tracks are found with an acolinearity less than 60° are selected. The TEC trigger rate varies between 1 to 4 Hz depending on the beam conditions.

Muon Trigger

The muon trigger selects events with at least one charged particle penetrating the muon chambers. If hits in the muon chambers can be formed into a track of transverse momentum greater than 1 GeV, the trigger selects the event for further analysis. Measurements should be available from at least 2 P-layers and 3 Z-layers. The requirement of one good scintillation counter hit within 15 ns of the beam crossing removes cosmic muons. The typical trigger rate is less than 1 Hz.

Scintillation Counter Trigger

Trigger information from the scintillation counters is used to select high multiplicity events and to reject cosmic events. Selection of high multiplicity events requires 5 scintillation counter hits spread by over 90°. The typical trigger rate is 0.1 Hz which is practically free of backgrounds.

Luminosity Trigger

The input to the luminosity trigger is the analog sum of energies from the luminosity monitor dividing the detector on either side of the interaction point into 16 ϕ sectors. Bhabha events are triggered if any of the following three threshold conditions are satisfied

- two back-to-back (within $\pm$ 1 segment) energy depositions with energy $\geq$ 15 GeV,
- total energy on one side greater that 25 GeV and on the other side greater than 5 GeV,
- total energy in either end greater than 30 GeV.

The latter trigger is used to check the efficiency of the earlier two and is pre-scaled by a factor 20. As the statistical error does not dominate the luminosity determination the first two triggers are pre-scaled by a factor of two from 1991 onwards.

The typical trigger rate is 1.5 Hz which depends on the delivered luminosity, and hence can change drastically in bad beam conditions.

3.3.2 Second Level Trigger

The second level trigger [44] tries to reject background events from the sample selected by the first level. The inputs to the second level trigger are the coarse digitised data used at the first level, the result from the first level and additional informations from combined energy clusters in the calorimeters, loosely reconstructed tracks and the interaction point. The second level trigger spends about 8 ms per event without inducing any dead time and hence improves on the first level result using the correlation among the signals from various subdetectors. The second level trigger efficiently rejects events induced by electronic noise, beam-gas, beam-wall interactions, and synchrotron radiation. All data are passed to an event builder memory. In case of a positive decision, the input to the second level trigger and all the second level results are forwarded to the third level trigger. On a negative second level decision event builder memories are reset. An event passes unaffected through the second level if it is selected by at least two independent triggers in the first level. The rejection power of second level trigger is typically 20 to 30% averaged over all first level triggers.

3.3.3 Third Level Trigger

Unlike the first and the second level triggers, the third level [45] accesses the fully digitised data with finer granularity and better resolution. The principle of operation is similar to that of the second level but now based on recalculated and calibrated energies, fully reconstructed muon tracks, reconstructed vertex from TEC tracks which match the calorimetric clusters. The time available to the third level trigger to analyse an event is about 10 times that spent by the earlier levels. As in the second level, events, selected independently by more than one first level triggers, pass unhindered through this level. Typical trigger rate at the third level is 2–3 Hz. On a positive third level trigger the data is transferred to the main acquisition system which is subsequently written to tapes.

Chapter 4

Simulation and Reconstruction

Simulation of detector response using known physical processes and reconstruction of final state particle and energy flow from the observed detector signals are the most important aspects of physics analyses of a high energy physics experiment. Figure 4.1 schematically shows the various stages through which analyses proceed in a typical experiment to obtain physics results using raw detector data and simulated Monte Carlo data. Events are reconstructed from detector signals for both kinds of data in a similar manner.

4.1 Monte Carlo Simulation

Monte Carlo simulations play an important role all along the lifetime of an experiment. Optimisation of detector geometry is achieved from the set physics goals with the help of simulations during the preparatory phase of the experiment. Much of the understanding of physics is gained through a detailed Monte Carlo simulation of relevant physics processes. When the experiment is underway, Monte Carlo simulations are used to establish selection criteria of a physics analysis by optimising selection efficiency and signal-to-background ratio. Detector effects like acceptance and resolution are studied using simulations in order to correct observed distributions and to extract physics results.

In the L3 experiment, Monte Carlo simulation has been carried out as a two step process

(a) *Event generation*, where simulation of physics processes of interest are carried out,

(b) *Detector Simulation*, where the generated particles are traced through detector media and response of the detector is simulated.

4.1.1 Event Generation

Event generation is the part of the simulation where events are produced with a distribution according to a physical theory. For each generated event, the type, energy-momentum

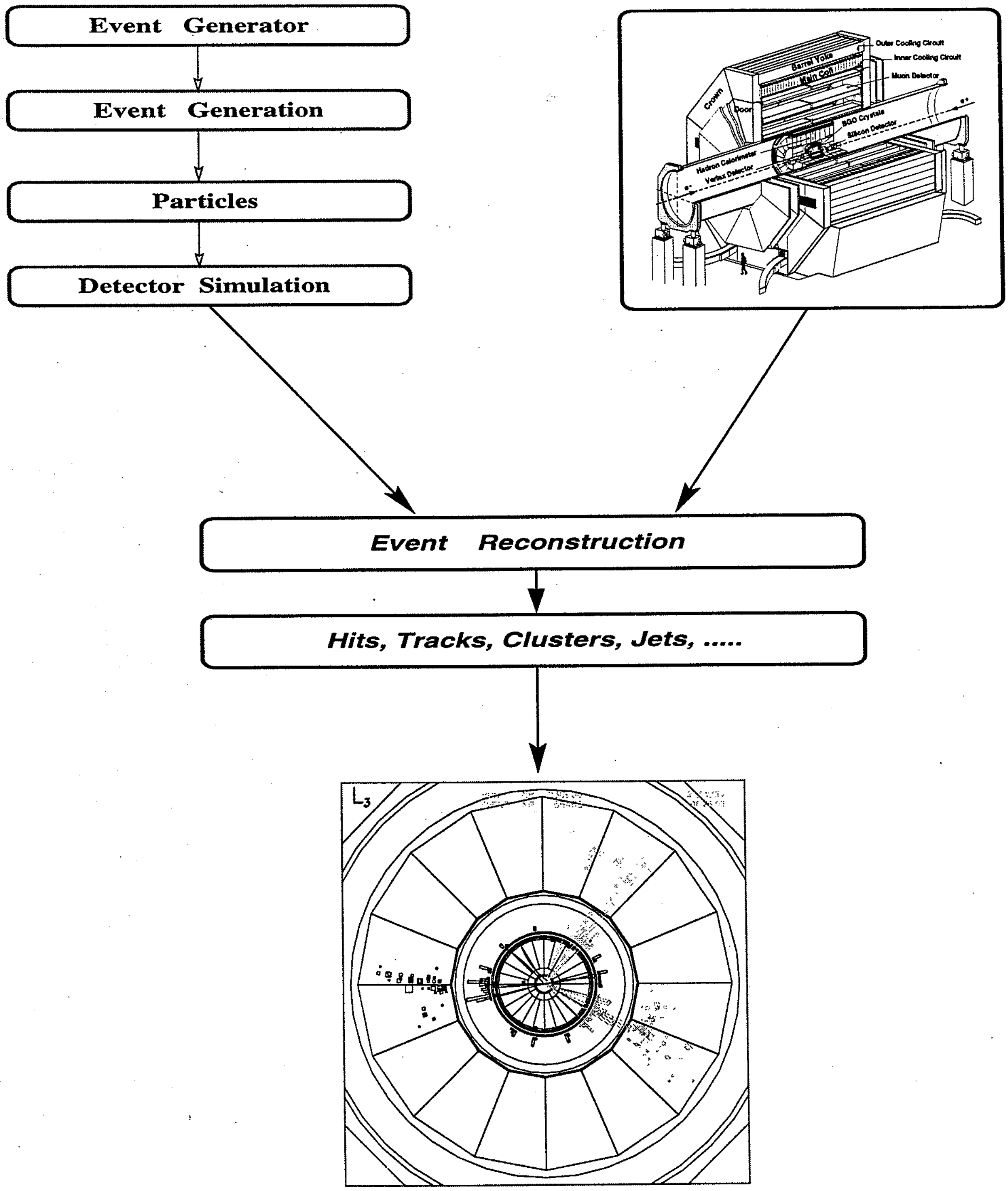

Figure 4.1: Reconstruction of events from raw detector signals and detector simulated Monte Carlo signals within the same framework. The reconstructed objects such as, tracks, clusters, jets are used to extract physics results.

and space-time four vectors of all the particles in the final state are stored in data structure for subsequent use in detector simulation and in physics studies.

As described in Section 2.3.3, the process $e^+e^- \to$ *hadrons* involves several steps

(a) e^+e^- interaction and production of quark-antiquark pair,

(b) perturbative QCD evolution,

(c) transition of partons into hadrons and,

(d) decays of unstable hadrons into stable particles.

The first two steps are analytically calculable by perturbative electroweak theory and quantum chromodynamics respectively. But the phase, where partons transform into observable hadrons, cannot be described by any perturbative calculation. Different phenomenological models are used to describe the fragmentation process which have been discussed in Section 2.3.5.

QCD Event generators

Several QCD generators have been developed to describe the complicated QCD physics in e^+e^- interactions. They implement different approaches to perturbative QCD with different models of fragmentation. Each generator has its own set of parameters to describe shower development and fragmentation. The parameters are tuned [46] using data by a particular experiment. Tests of QCD thus depend on these parameters. QCD event generators which are in wide use and in particular studied in the analyses presented here are the following:

(a) *JETSET*:

The Monte Carlo programme JETSET [47,48] simulates e^+e^- annihilation into quark-antiquark pair and subsequent quark and gluon branchings. Both parton shower (PS) and $\mathcal{O}(\alpha_s{}^2)$ matrix element (ME) options are available. The parton shower is based on improved leading logarithm approximation with angular ordering and azimuthal correlations. JETSET contains a description of the full γ/Z exchange together with first order initial state radiative correction. The first gluon branching is modified using the first order matrix element to reproduce the 3-jet rate. String fragmentation is used to model the hadronisation process, although, independent fragmentation can also be selected. JETSET incorporates decays of unstable particles in great detail. Description of experimentally observed effects like Bose-Einstein condensation is incorporated in JETSET.

Prompt photons can be emitted off quarks (antiquarks) in the final state as part of the shower evolution algorithm in JETSET. The $q\to qg$ and $q\to q\gamma$ branching implementations are closely analogous. But there are some differences as discussed in Section 2.5.

The string fragmentation model in JETSET PS uses the Lund symmetric function [14] for light quarks, which is characterised by the parameters a and b:

$$f(z) \sim z^{-1}(1-z)^{a} \exp\left(-\frac{bm_T^2}{z}\right).$$

For heavy quarks, charm and bottom, the Peterson fragmentation function [49], characterised by ϵ_Q, is used:

$$f(z) \sim z^{-1}\left(1-\frac{1}{z}-\frac{\epsilon_Q}{1-z}\right)^{-2},$$

where z is the light cone variable and m_T is the transverse mass. In addition, one smears the hadronic transverse momenta (p_T) with respect to the jet direction using a parameter σ_q.

$$f(p_T) \sim \exp\left(-\frac{p_T^2}{\sigma_q^2}\right).$$

The parameters which affect hadronic event structure most are the parton shower scale Λ_{LLA}, the parton shower cutoff parameter Q_o and the fragmentation parameters a, b, ϵ_Q and σ_q.

(b) *ARIADNE*:

The formation of perturbative QCD shower can be formulated either in terms of quarks and gluons radiating additional partons, as implemented in JETSET and HERWIG programmes, or in terms of the colour dipole system formed by the initial parton configuration. ARIADNE [50] adopts the second approach. When a gluon is emitted from a dipole, the subsequent emission of a soft gluon is given by two independent dipoles, one stretched from the quark to the gluon and the other from the gluon to the antiquark. Emission of another gluon is achieved by three independent dipoles and so on. Angular ordering and the ordering in transverse momentum are automatically achieved in this manner. The concept of electromagnetic dipole radiation is also incorporated in detail in this programme. ARIADNE is interfaced to JETSET for the hadronisation of the generated perturbative cascade using string fragmentation.

Table 4.1 lists the tuned L3 parameters for JETSET 7.4 PS, JETSET 7.4 ME and ARIADNE 4.6 Monte Carlo Programmes.

Parameter	JETSET 7.4 PS	JETSET 7.4 ME	ARIADNE 4.06
Λ (GeV)	$0.311 \pm 0.022 \pm 0.026$	$0.152 \pm 0.005 \pm 0.005$	$0.254 \pm 0.013 \pm 0.020$
σ_Q (GeV)	$0.411 \pm 0.019 \pm 0.028$	$0.430 \pm 0.015 \pm 0.021$	$0.384 \pm 0.017 \pm 0.018$
b (GeV^{-2})	$0.886 \pm 0.060 \pm 0.104$	$0.310 \pm 0.014 \pm 0.007$	$0.772 \pm 0.034 \pm 0.067$

Table 4.1: Tuned L3 Parameters for the JETSET 7.4 Parton Shower, JETSET 7.4 Matrix element and ARIADNE 4.06 programmes.

(c) *HERWIG*:

The parton shower generator, HERWIG [51], incorporates a detailed simulation of QCD interference phenomena and spin effects. The parton shower evolution takes into account the correlation between the parton 4-momenta due to spin and the coherent emission of soft gluons. The treatment of soft gluon emission is based on the Coherent Parton Branching formalism [52] which is an extension of the leading logarithm approximation (LLA). The parton shower simulation is accomplished in three stages. Parton branchings are generated first. Then all the partons are assigned four-momenta. Azimuthal correlations between the partons inside a shower are defined in this stage as well. The gluons are split non-perturbatively into $q\overline{q}$ pairs and the overall event is assembled which subsequently undergoes hadronisation. HERWIG incorporates cluster fragmentation to describe hadronisation of the parton shower. Radiation of photons off quarks (antiquarks) in the final state is incorporated in this programme. HERWIG 5.8 does not contain description of initial state radiation.

Event shape variables are most sensitive to the parton shower scale parameter Λ_{MLLA}, the effective gluon mass, and the cluster mass CLMAX, which is a threshold parameter determining whether the clusters decay into hadrons or into lower mass clusters.

Table 4.2 lists the optimised L3 parameters for the HERWIG 5.8 Parton Shower programme.

Parameter	HERWIG 5.8 Parton Shower
Λ_{MLLA} (GeV)	$0.166 \pm 0.002 \pm 0.015$
CLMAX (GeV)	$2.968 \pm 0.055 \pm 0.105$
CLPOW	$1.569 \pm 0.020 \pm 0.219$

Table 4.2: Tuned parameters for the HERWIG 5.8 Parton Shower programme.

(d) *COJETS*:

COJETS [53] is based on leading logarithm calculations. Multiple initial state radiation is included. The branchings in the parton shower are incoherent. Final partons are transformed into hadrons by the Field-Feynman independent fragmentation model [12]. Unstable particle decay modes are specified in a table, which can be changed by the user. COJETS has four free parameters in its longitudinal fragmentation function and one free parameter to control the transverse momentum spectra in the fragmentation cascade. Since quarks and gluons fragment independently, these parameters can have different values for quark and gluon jets. The other important parameters of COJETS are the parton shower scale parameter, Λ_{LLA} and the parton shower termination parameter, Q_o.

The parameters tuned using L3 data for the COJETS 6.23 Monte Carlo programme are given in table 4.3.

Parameter	COJETS 6.23
$b_q(GeV^{-}1)$	43.0 ± 5.0
$b_g(GeV^{-}1)$	100.0 ± 20.0
d_q (GeV)	2.1 ± 0.5
d_g (GeV)	2.1 ± 0.5

Table 4.3: Tuned L3 parameters for the COJETS 6.23 programme.

4.1.2 Detector Simulation

Detector simulation is an indispensable tool to optimise detector and trigger designs. All measurements in high energy physics experiments get affected by the finite resolution of detectors and their limited acceptance. These effects, can only be studied by simulating response of the detector for a process with known final state and then reconstructing back the event from the detector signals.

The L3 detector simulation programme SIGEL3 describes the experimental setup and response of the L3 detector using the general purpose detector simulation programme, GEANT3 [54].

GEANT3 provides a framework to define sophisticated detector geometry through geometrical volumes organised in a hierarchical tree structure. It provides an elaborate simulation of physical processes such as decay, energy loss, multiple scattering, nuclear interaction, bremsstrahlung, pair production, photo-fission and so on. For simulating the complicated physics of hadronic interactions, GEANT3 can use specific packages of hadronic shower development, such as GHEISHA [55].

The physical properties such as material constants and magnetic field are associated with the geometrical structure. Particles are tracked step by step through the detector setup. The response of each active medium is simulated in detail while the particles traverse the active materials of the detector.

SIGEL3 represents the complete L3 detector describing the details of each subdetector geometry down to the level of individual readout channels. Examples illustrating the complexity of this geometry are the hadron calorimeter, with 426904 brass cells grouped into $\sim$ 26000 towers, and the electromagnetic calorimeter, with 10734 BGO crystals of different shapes and a thin walled carbon fibre support structure. Both the calorimeters are fully described. Simulation of electromagnetic and hadronic showers in complex, non-uniform media needs tracking of low energy particles precisely. Particles are tracked down to around 10 KeV in the BGO calorimeter and down to $\sim$ 1 MeV in the hadron calorimeter.

Results from the test beam exposures on the calorimeters in 1986 to 1987 [28] were used to fine tune the parameters in the simulation. The parameters include, the step size for particle tracking in all subdetectors, medium dependent energy cut-off values, saturation in light yield, the light collection efficiency, electronic noise in the electromagnetic calorimeter etc. Uranium noise in the hadron calorimeter was simulated according to experimentally determined spectra.

Hits in the central tracking detector and the muon spectrometer are simulated using the time-to-distance relation measured in the test beam data. Details of the response, such as multiple hits, cross talk and δ-rays are also included.

The scintillation counter ADC and TDC informations are also simulated. Pulse height are corrected for attenuation and times are corrected for the flight time of the particle and the transmission time of the scintillation light.

Simulation of Detector Imperfections

The inefficiencies caused by the imperfections in the detector components, e.g., the dead cells or noisy BGO crystals, high voltage status of the TEC wires (like disconnected sectors and inefficient wires), defective towers in the hadron calorimeter, disconnected drift cells in the muon chambers, vary over the time period of data taking. These time dependent inefficiencies of the detector response are simulated in Monte Carlo event samples in order to obtain a more reliable physics measurement.

L3 maintains an extensive data base system where informations on the status and calibration of each subdetector are stored. During reconstruction of real events, relevant informations are retrieved from the database using the date and time recorded in each event. Data from dead or noisy channels are discarded and appropriate calibrations are applied based on these informations.

During reconstruction of simulated data, where the time dependent detector status is incorporated, each event is temporarily ascribed a date and time by distributing them over a data taking interval using proper luminosity weighting. Because the detector simulation is time consuming, informations about the time dependent detector imperfections are simulated during the reconstruction of the simulated events.

4.2 Event Reconstruction

The process of event reconstruction converts the raw digitised detector signals into physically meaningful quantities. Pattern recognition algorithms then try to identify the basic objects for the physics analysis. Raw data provided by the L3 detector and the detector simulated data are reconstructed under the framework of L3 reconstruction programme, REGEL3 [56]. The reconstruction programme uses event signatures and tries to categorise them into different classes using loose selection criteria. One single event can belong to more than one class. Figure 4.2 shows the schematic view of flow of data in L3 reconstruction programme starting from raw detector signal and culminating in objects used in physics analyses.

The reconstructed data are available in three formats according to decreasing size and increasing abstraction.

(i) *Data Reconstruction* (DRE) Format:

This format retains most of the raw detector informations (hits in the central tracking chamber, channel wise calorimeter data etc.) alongwith the reconstructed objects like tracks, clusters etc.

(ii) *Data Summary* (DSU) Format:

Some of the raw detector informations are dropped to reduce the size of an event significantly. This format allows a redefinition and calibration of reconstructed tracks, clusters etc.

(iii) *Data Avanti* (DVN) Format:

Data in this format contain only the most important reconstructed objects. The event size is reduced to a minimum to allow for an easy and quick analysis. However, as all the raw detector informations are dropped, data in DVN format cannot be used for re-reconstruction.

The reconstructed objects used in physics analyses are the following,

(a) *Tracks*:

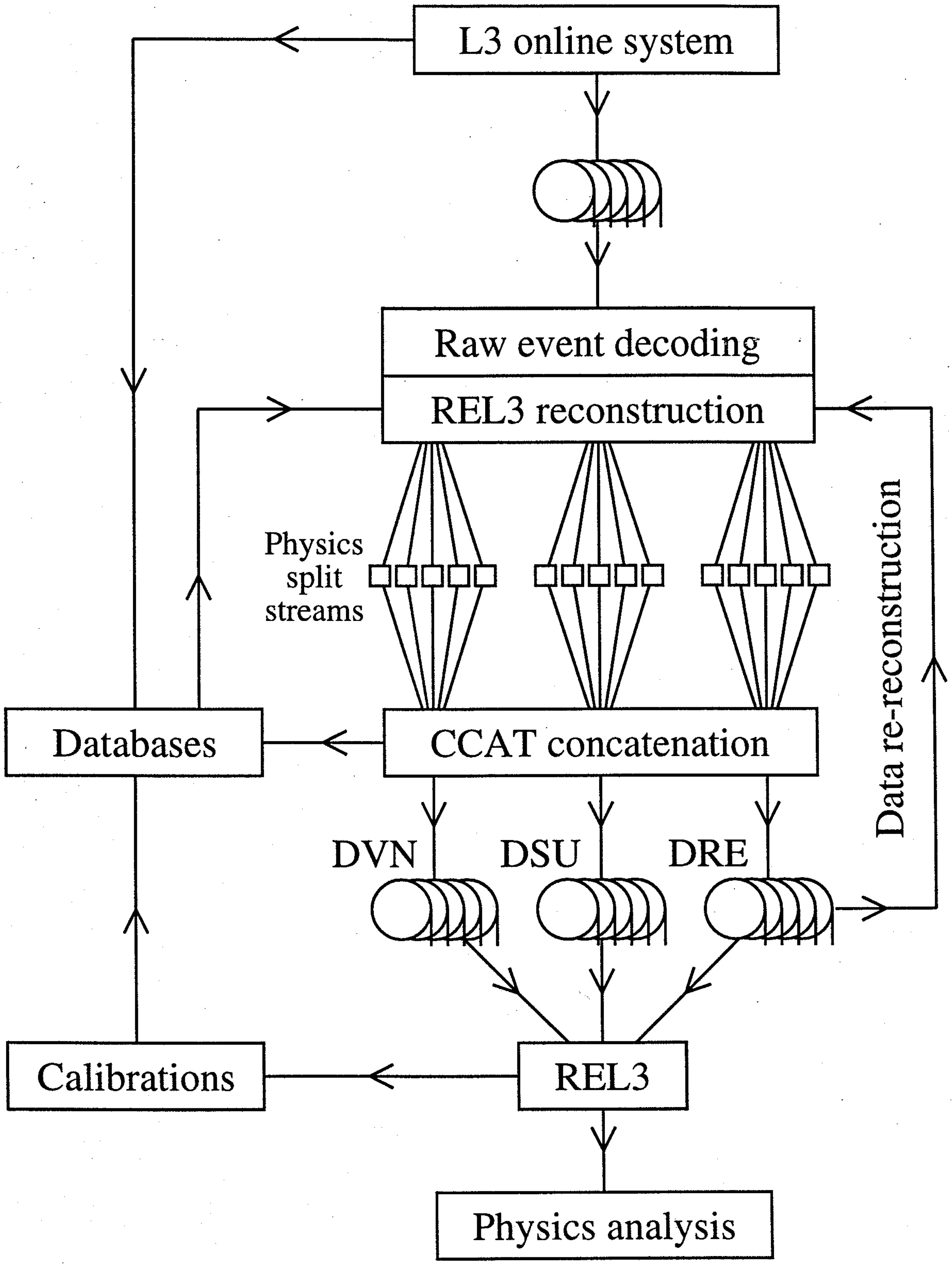

Figure 4.2: Schematic view of flow of data from online system towards physics analyses.

Hits in the central tracking chamber are combined to map to the trajectory of charged particles in the detector. The curvature of the trajectory is used to measure the transverse momentum and the sign of the charge of the particle. The parameters of each track, (a) the curvature, (b) distance of closest approach (DCA) of the track to the event vertex, and (c) the polar and azimuthal angles of the track at the vertex, are extracted from a fit to the coordinates of the hits. A reconstructed track is specified by

— polar and azimuthal angles of the track,

— length of the track (SPAN) defined from the innermost and the outermost hits,

— distance of closest approach of the track to the event vertex,

— Number of wires hit by the track,

— transverse momentum of the track,

— χ^2 of the track fit.

In the context of the present analysis a track is qualified as a *good track* if it satisfies the following requirements:

- track SPAN larger than 30,
- DCA smaller than 50 mm in the r$-\phi$ plane,
- number of wires hit greater than 30,
- transverse momentum greater than 100 MeV.

(b) *Clusters* in the electromagnetic calorimeter:

The purpose of reconstruction of objects in the electromagnetic calorimeter is to determine the energies and directions of particles interacting with the BGO material and to classify showers as electromagnetic, hadronic or caused by minimum ionising particles.

Raw ADC signal from each crystal is converted into an energy value as the first step towards reconstruction of data from the electromagnetic calorimeter. The conversion accounts for the changing response of each crystal, due to temperature variations and intrinsic losses associated with aging and radiation damage. Geometrical clusters are then formed by combining adjacent crystals with energy greater than 10 MeV into groups. Clusters with a total energy less than 40 MeV are not considered.

The next step is to identify energy deposits that are characteristic of single particles within a geometrical cluster. Local maxima within a geometrical cluster are first identified which are referred to as *bump crystals.* Bump crystals should have energy larger than 40 MeV. Each non-bump crystal is then associated to its nearest bump crystal in the same geometrical cluster. If a crystal is equidistant to more than one bump crystal, it is assigned to the more energetic one. A bump crystal with all its associated neighbours is referred to as a *bump*. If two bumps are overlapping, no attempt is made to determine the actual sharing of the energy between the two bumps.

Electrons and photons lose their entire energy in the electromagnetic calorimeter giving rise to characteristic electromagnetic showers. Hadrons lose their energy dominantly through nuclear interactions in the electromagnetic calorimeter resulting in diffuse deposits with large fluctuations. Muons produce small signals that are almost independent of their energy. So, a study of the shower shape enables identification of electrons and photons from muons and hadrons.

The quantities of interest of a cluster in the electromagnetic calorimeter are the following:

- number of crystals with significant energy depositions,
- energy of the bump crystal (E_1),
- energy in 3×3 (E_9) and 5×5 (E_{25}) crystal matrices around the bump crystal,
- χ^2 of the shower shape fit assuming the cluster to be of electromagnetic origin,
- variance of the energy distribution.

(c) *Clusters* in the hadron calorimeter:

Reconstruction of the clusters in the hadron calorimeter starts from the individual tower signals. A tower is accepted only if its energy deposit is greater than 9 MeV. This condition removes most hits coming from uranium noise. The towers are then grouped into clusters using sophisticated pattern recognition algorithms which are based on association of nearby towers. Towers which are nearby either in radial or in angular direction can form a cluster. The pattern recognition algorithm discriminates between clusters originating from interacting hadrons and those caused by minimum ionising muons. A muon traversing the hadron calorimeter deposits energy which is localised near its track.

(d) *Muons*:

The search for tracks in the barrel part of the muon chamber starts from the separate hit signals in the P and Z chambers. The first step is to combine the hit patterns in a given chamber into segments. Subsequently, a set of P segments is matched with the Z segments in the same octant. A muon candidate is a track reconstructed in the muon chambers with at least two P segments and one Z segment. The relevant parameters of a track are:

- number of P or Z segments,
- momentum of the track,
- DCA after back tracking to the nominal event vertex,
- time of flight registered by the associated scintillation counters.

(e) *Smallest Resolvable Clusters*:

Event reconstruction is aimed at providing a detailed knowledge of the particle content of a given event. To fulfil this objective it is often necessary to combine informations from different subdetectors. This procedure is known as *global reconstruction.*

The first step is to associate tracks in the central tracking chamber with energy depositions in electromagnetic or hadron calorimeter, based on angular proximity. Subsequently, the unmatched clusters in the electromagnetic calorimeter are matched geometrically with hadron clusters in the hadron calorimeter if there is energy deposit in the front layer of the hadron calorimeter. Finally, muon tracks are matched with the closest energy depositions in the calorimeters.

The resulting objects are the so-called *smallest resolvable clusters* (SRC's). On the basis of subdetector informations, each SRC is classified as being of electromagnetic, hadronic or mixed origin. The SRC's are used in the physics analysis to derive quantities such as total visible energy, energy imbalances along and transverse to the beam direction which contain global event information.

(f) *Jets*:

Reconstruction of jets are accomplished from reconstructed electromagnetic and hadronic clusters and muons. The most energetic cluster is selected as the seed and standard algorithm combines nearby clusters, not already assigned to any other seed, to the seed under consideration using angular proximity. A jet is characterised by the following quantities,

- energy and direction,
- thrust,
- invariant mass,
- multiplicity.

Figure 4.3 summarises the reconstruction chain within the REGEL3 framework starting from reconstruction of objects in individual subdetectors towards creation of smallest resolvable clusters and jets.

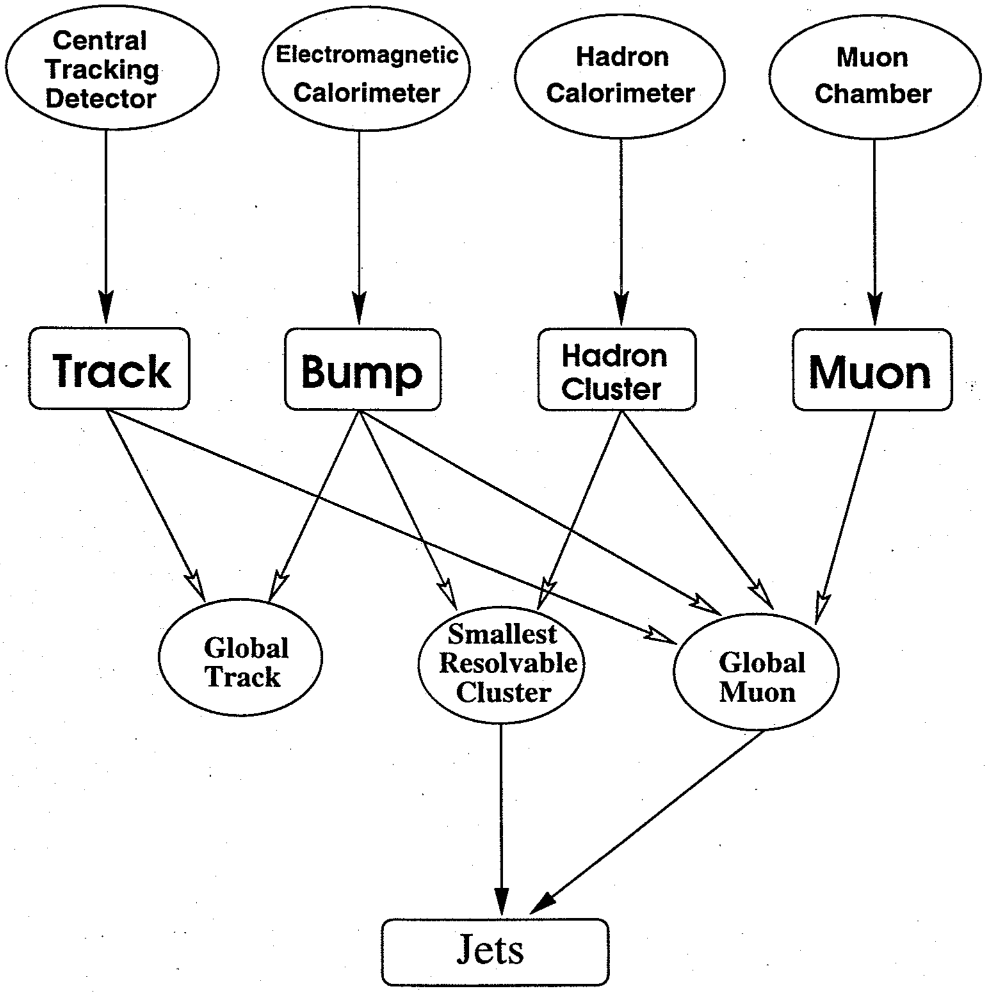

Figure 4.3: Reconstruction of objects in the REGEL3 framework, starting from reconstruction of objects in individual subdetectors towards creation of smallest resolvable clusters and jets.

Chapter 5

Energy Calibration

A particle traversing a calorimetric system produces showers of particles through interactions with the medium. The electromagnetic component of the shower is generated by successive bremsstrahlung processes and photon conversions to electron-positron pair until the energy of the charged secondaries has been degraded to the regime dominated by the ionisation loss. Showers initiated by strongly interacting particles are very complex with about half the energy going into multi-particle production and the other half carried by a few high energy leading particles. The basic processes are coherent elastic, incoherent elastic and incoherent inelastic reactions. The resulting cascade is mostly composed of nucleons and pions of which roughly 1/3 are π° each of which subsequently decays into a pair of photons. The shower therefore, has an electromagnetic component followed by the hadronic component.

The characteristic feature of the hadronic events in $e^{+}e^{-}$ interactions is a large number of charged and neutral particles in the final state. These particles are dominantly produced at large scattering angles. In experiments with hermetic detectors, therefore, a large fraction of the incident energy is visible in hadronic events. This feature can be utilised to scale the total visible energy to the centre of mass energy for the final energy calibration. The excellent energy and spatial resolutions of the L3 electromagnetic and hadron calorimeters allow us to estimate the energy of the particles traversing the detector precisely from the energy deposited in the calorimeters. Hence the total visible energy of the event can be estimated using simple weight factors for different detector regions. These factors in the L3 environment are known as G-factors [57]. An accurate measurement of the energy of an individual particle or the total energy of an event rests on a precise determination of the G-factors. This has important implications in all the physics analyses.

5.1 Energy Determination

The energy E_{particle} of a particle traversing a calorimetric system can be reconstructed as a function of the energy deposited in the electromagnetic and hadron calorimeters and is given by

$$E_{\text{particle}} = f(E_{\text{em}}, E_{\text{hcal}}) .$$

The function f depends on the physical process which triggers the shower and also on the characteristic of the detector.

If the shower generated is purely electromagnetic most of the energy is deposited in the electromagnetic calorimeter and one can write

$$E_{\text{particle}} = \alpha E_{\text{em}} .$$

If the electromagnetic calorimeter were calibrated using some absolute method, then, for an electromagnetic shower the factor α could be set to unity.

A hadronic shower has both hadronic and electromagnetic components of energy and hence the simplest form of energy of a hadronic shower is a linear combination

$$E_{\text{particle}} = \alpha E_{\text{em}} + \beta E_{\text{hcal}}$$

where the difference in the resolutions of the electromagnetic and hadron calorimeters has been taken into account in the factors α and β which have to be determined experimentally.

5.2 Energy Measurement From ASRC And ECLU

The L3 calorimeter system has been divided into a number of geometrical regions as shown in figure 5.1. Regions 1, 3, 7, and 9 are associated with the electromagnetic calorimeter whereas regions 2, 4, 6, 8 and 10 belong to the hadron calorimeter. Regions 11 and 12 refer to the muon chamber and the central tracking detector respectively. Region 3 actually corresponds to the front part of the hadron calorimeter and measures the electromagnetic energy in the gap region between the BGO barrel and the endcaps. The momentum of the muon tracks as measured in the muon chamber (region 11) can be optionally added in the total energy determination. Energy measured neither in luminosity monitor nor in active lead ring (ALR) is considered for the total energy determination. As is evident from figure 5.1 a particle passing through the detector can deposit energy only in neighbouring regions.

We define the energy of an ASRC as

$$E^{\text{cluster}} = \sum_{i} G_i E_i^{\text{cluster}}$$

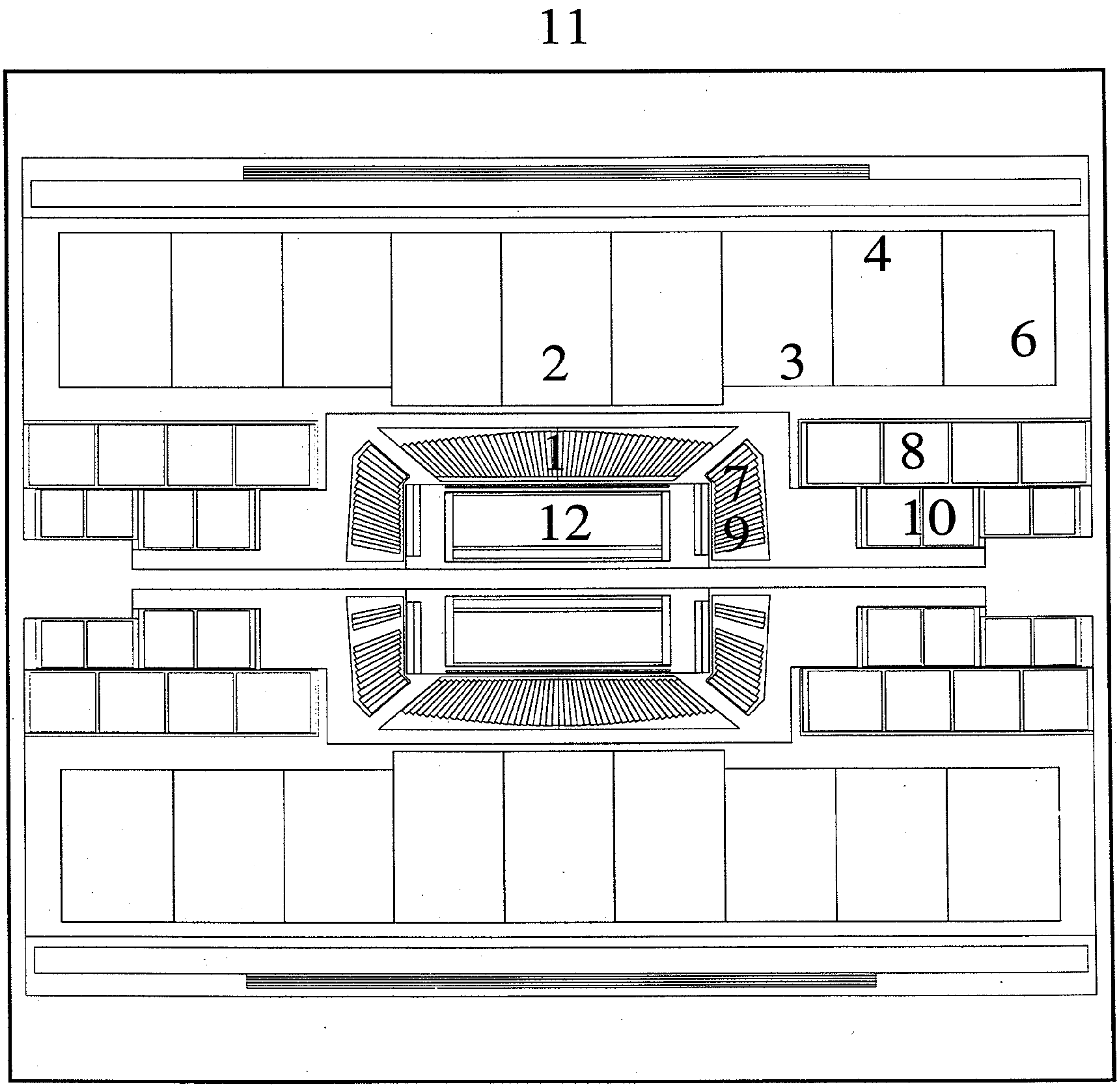

Figure 5.1: The different geometrical regions of the L3 Calorimeter system. Regions 1, 3, 7, and 9 are associated with the electromagnetic calorimeter whereas regions 2, 4, 6, 8 and 10 belong to the hadron calorimeter. Regions 11 and 12 correspond to the muon chambers and the tracking chamber respectively.

where the sum runs over the detector regions where the cluster has deposited its energy. $E_i^{cluster}$ is the raw energy in region i and the G_i is the G-factor for the corresponding region.

The total energy of an event, which is independent of the definition of a cluster, can thus be expressed as the sum over all the cluster energies or equivalently as the sum over the total energies measured in individual regions as given by

$$E_{tot} = \sum_c E^c = \sum_c \sum_i G_i \cdot E_i^c = \sum_i G_i \sum_c E_i^c = \sum_i G_i \cdot E_i$$

where $E_i = \sum_c E_i^c$ is the total raw energy deposited in the detector region i. The numerical values of the G-factors are determined by minimising the total energy resolution on hadronic events while constraining the mean visible energy to the centre of mass energy.

We extend these ideas to the case where the tracks measured in the central tracking chamber and the non-negligible correlations among the energy measured in neighbouring detector parts are included in the definition of total energy.

We redefine the clusters, which we call ECLU's, using angular association of the standard ASRC components, track components (ATRK's) and muons. We:

- group all possible pairs whose angular separation is compatible with resolution,
- combine each combination with energy cluster from different detector regions to construct *supercluster*,
- resolve all ambiguities so that no energy cluster is shared by more than one *supercluster*,
- compute the energy and direction of the *supercluster* (ECLU) using correlation in energy measurements among neighbouring detector regions.

The criteria we use for the association of constituents into seeds or superclusters is a cut on the distance between constituents, D, defined as

$$D^2(i,j) = \frac{\Delta_{ij}^2 \phi}{S_{ij}\phi} + \frac{\Delta_{ij}^2 \cos\theta}{S_{ij}\cos\theta}$$

where $\Delta_{ij}x = x_i - x_j$ and $S_{ij}x = \sigma_x^2(i) + \sigma_x^2(j)$, with σ corresponding to the estimated detector resolution for each constituent class. The cut value has been chosen to provide a similar cluster multiplicity for both ASRC and ECLU algorithms.

The total energy of an event can then be written as

$$E_{tot} = \sum G_i \cdot E_i + \sum_{jk} A_{jk} \cdot C(E_j, E_k)$$

where the sum includes informations from all the 12 detector regions. $C(E_i, E_j)$ is the correlation function which has to be parametrised to have the best energy resolution. The correlation coefficients A_{jk} have non vanishing values only when connecting neighbouring regions.

The simplest form of the correlation function is given by

$$C(E_i, E_j) = E_i \cdot E_j$$

although other forms like

$$C(E_i, E_j) = \frac{E_i \cdot E_j}{E_i + E_j}$$
$$C(E_i, E_j) = \sqrt{E_i \cdot E_j}$$

are applicable as well. The simplest form has been found to provide the best energy resolution.

The total energy of an event can be rewritten as

$$\begin{aligned} E_{tot} &= \sum_i G_i \cdot E_i + \sum_{jk} A_{jk} E_j \cdot E_k \\ &= \sum_i \widetilde{G}_i \cdot E_i \end{aligned}$$

where we have recast the total energy in the usual form making the G-factors energy dependent,

$$\widetilde{G}_i = G_i + \sum_j A_{ij} \cdot E_j$$

The fact that total energy now is a nonlinear function of input energies introduces a potential problem of energy scale. Scaling all measured energies by a factor α or equivalently changing the centre of mass energy from E_{cm} to αE_{cm} does not reproduce the expected scaling in total energy

$$\begin{aligned} E'_{tot} &= \alpha \sum_i G_i \cdot E_i + \alpha^2 \sum_{jk} A_{jk} E_j \cdot E_k \\ &\neq \alpha E_{tot} \end{aligned}$$

One observes that the coefficients A_{ij} carry dimensions of $(\text{energy})^{-1}$, hence they could only be correct at a particular energy scale.

The energy of the supercluster has the general expression

$$E^c = \sum_{i=1} \tilde{G}_i \cdot E_i^c + \sum_{jk} \tilde{A}_{jk} \cdot \tilde{C}(E_j, E_k)$$

where E_i^c stands for the sum of uncorrected energy of all the constituents of the supercluster which are in the detector region i. The correlation function $\tilde{C}$ has been chosen as

$$\tilde{C}(E_j^c, E_k^c) = \frac{E_j^c \cdot E_k^c}{(E_j^c + E_k^c)}.$$

The inclusion of nonlinearities in the definition of total and cluster energy leads to the following consequence: $E_{tot} \neq \sum_c E^c$. This inconsistency is solved with the introduction of an overall multiplicative factor on E^c. The final supercluster energies, $\widetilde{E^c}$, are defined as

$$\widetilde{E^c} = K \cdot E^c$$

where

$$K = \frac{E_{tot}}{\sum_c E^c}.$$

5.3 Selection of Hadronic Events

The hadronic events are characterised by a large number of final state particles with most of the energy visible in the detector. The Hadronic events are recorded primarily from calorimetric energy trigger with a trigger efficiency exceeding 99.9%.

The selection of events of the type $e^+e^- \rightarrow$ hadrons is based on the energy measurements in the electromagnetic and hadron calorimeters. Events are accepted if

$$0.6 < \frac{E_{vis}}{\sqrt{s}} < 1.4 \quad , \quad \frac{|E_{||}|}{E_{vis}} < 0.40 \quad , \quad \frac{|E_{\perp}|}{E_{vis}} < 0.40 \quad , \quad N_{cluster} > 12$$

where E_{vis} is the total energy observed in the calorimeters; $E_{||}$, $E_{\perp}$ are the energy imbalances along and transverse to the beam direction and $N_{cluster}$ is the number of clusters with energy larger than 100 MeV. A study of simulated events reveals that 98% of hadrons are selected by these cuts with a small background of 0.2% from $(\tau^+\tau^-)$ and four fermion final states from 2 photon processes.

5.4 Determination of G-factors

We calculate the average raw energies in each geometrical region over a reasonably large number of hadronic events to calculate the average total energy and the variance. For

ARSC's the quantities are given by

$$\begin{aligned}
\overline{\mathrm{E}} &= \sum_{\mathrm{i}} \mathrm{G_i}\overline{\mathrm{E}}_{\mathrm{i}} \\
\sigma^2 &= \overline{(\mathrm{E}-\overline{\mathrm{E}})^2} \\
&= \sum_{\mathrm{i,j}} \mathrm{G_i G_j}(\overline{\mathrm{E_i E_j}} - \overline{\mathrm{E}}_{\mathrm{i}}\,\overline{\mathrm{E}}_{\mathrm{j}})
\end{aligned}$$

where $\overline{\mathrm{E}}_{\mathrm{i}}$ is the average energy in region i. Similar relations hold good for ECLU.

The G-factors are fitted to minimise the function

$$\mathrm{M} = \left(\frac{\sigma}{\overline{\mathrm{E}}}\right)^2 + \lambda\left(\frac{\sqrt{\mathrm{s}}}{\overline{\mathrm{E}}} - 1\right)^2$$

where the first term denotes the energy resolution and the second term imposes energy-momentum conservation. λ is the Lagrange's multiplier and has been assigned a large value.

Total visible energy, and thus the selection of hadronic events, depends on the values of G-factors. The initial set of values of the G-factors thus affects the minimisation process and the subsequent values. The dependence of the final G-factors on the input set may be reduced to a minimum by dividing the whole event sample in a number of sub-samples each containing a reasonable number of events ($\geq$ 1000) and applying the G-factors estimated from one sub-sample for the selection of hadron events in the next sub-sample in an iterative process. It has been observed that reliable values of the G-factors could be obtained even with a relatively small sample.

We have used two types of simulated events which are used in L3 analyses, (a) Ideal and (b) Real Detector simulated, Monte Carlo events. For the ideal Monte Carlo (IMC) events intrinsically the energy resolution is better than the corresponding energy resolution for data. So instead of minimising the energy resolution as described above we used the average energy values and the G-factors for individual regions for each iteration from data to constrain the G-factors for ideal Monte Carlo event sample assuming the following relation to hold good in each detector region.

$$\mathrm{G_i^{IMC}} = \mathrm{G_i^{Data}} \frac{\overline{\mathrm{E_i^{Data}}}}{\overline{\mathrm{E_i^{IMC}}}}$$

where fluctuation in energy measurements may render a different set of values of G-factors for ideal Monte Carlo.

For the real detector simulated Monte Carlo (RMC) we adopt the same procedure as that used in the case of real data.

In the case of determination of linear G-factors we may consider various options depending on the inclusion of muons in the energy determination. One may also try to separate the electromagnetic clusters for a more accurate determination of the energy of electrons and photons. The options used in this analysis are the following:

(a) *Calorimetric Option*: Only the calorimetric clusters having energy $\geq$ 100 MeV determine the total energy of an event. The muons detected in the muon chambers are not included.

(b) *Muon Option*: Calorimetric clusters as well as the energy from reconstructed muons are used

$$E = \sum_{i=1}^{10} G_i E_i + P_\mu$$

the estimated loss of energy of muon in the calorimeters can be optionally subtracted which is double counted in this case as muon energy determined from the muon chamber is corrected for this loss. This options offers the best energy resolution.

(c) *Electromagnetic Option*: For pure electromagnetic shower triggered by an electron or a photon almost all the energy is deposited in the electromagnetic calorimeter alone. As the L3 electromagnetic calorimeter is calibrated using an absolute method, for an electromagnetic cluster, the G-factors for the detector regions are set to unity and the energy deposited in other regions are neglected. This provides a much more accurate determination of the energy of an electron or a photon which could be very important in analyses involving electrons or photons exclusively. Nevertheless, the electromagnetic option results in a slightly worse energy resolution. The electromagnetic clusters are selected using the following loose criteria

1. $E_{ecal} > 0.5$ GeV
2. $E_{hcal}/E_{ecal} < 0.1$
3. $E_9/E_{25} > 0.95$

where $E_{ecal}(E_{hcal})$ is the electromagnetic (hadronic) energy of the cluster and $E_9(E_{25})$ is the energy measured in the 3×3 (5×5) crystal matrix around the central crystal.

5.5 Performance of ASRC and ECLU

The new algorithm shows several improvements over the standard energy flow algorithm. Figure 5.2 shows the visible energy distributions of the data sample using the two algorithms. The smooth curves shown on the figure are the results of fits to the observed distributions to a sum of Gaussians,

$$f\left(\frac{E_{vis}}{\sqrt{s}}\right) = \sum_{i=1}^{N} \frac{\omega_i}{\sqrt{2\pi}\,\sigma_i} \exp\left[-\frac{(E_{vis}/\sqrt{s} - \mu_i)^2}{2\sigma_i^2}\right]$$

The observed distributions for ASRC's are explained well by a sum of two Gaussians. For ECLU's a better description is found with a fit to a sum of three Gaussians. Tables 5.1 and 5.2 summarise the energy resolutions obtained from both of these methods for data and real detector simulated Monte Carlo. Figure 5.3 shows similar distributions when the thrust vector of the event is restricted to the central part of the detector ($|\cos\theta_{\text{thrust}}| <$ 0.74. The corresponding resolution parameters are listed in tables 5.3 and 5.4. One observes that the energy resolution, which could be parametrised by the rms spread of the distributions, improves from $\sim 13\,\%$ ($11\,\%$) in the ASRC algorithm to $\sim 10\,\%$($8\,\%$) in the ECLU algorithm, where the numbers in the parenthesis refer to events in the central part of the detector.

Year	Method	RMS Value		Results from the fit					
				w_i		μ_i		σ_i	
		Data	MC	Data	MC	Data	MC	Data	MC
1991	ASRC	0.124	0.124	0.72	0.83	1.011	1.008	0.105	0.112
				0.28	0.17	0.967	0.952	0.173	0.182
	ECLU	0.095	0.091	0.60	0.58	0.988	0.990	0.054	0.052
				0.40	0.42	1.018	1.021	0.133	0.123
1992	ASRC	0.129	0.127	0.69	0.79	1.013	1.009	0.109	0.114
				0.31	0.21	0.965	0.959	0.174	0.180
	ECLU	0.095	0.096	0.61	0.56	0.992	0.990	0.055	0.054
				0.39	0.44	1.014	1.013	0.135	0.131
1993	ASRC	0.129	0.128	0.68	0.78	1.013	1.008	0.110	0.115
				0.32	0.22	0.970	0.963	0.172	0.180
	ECLU	0.096	0.094	0.60	0.59	0.990	0.989	0.055	0.053
				0.40	0.41	1.015	1.017	0.135	0.131
1994	ASRC	0.129	0.127	0.71	0.77	1.010	1.005	0.112	0.114
				0.29	0.23	0.968	0.983	0.178	0.180
	ECLU	0.096	0.094	0.60	0.59	0.989	0.990	0.054	0.054
				0.40	0.41	1.018	1.013	0.136	0.131

Table 5.1: Resolution in $E_{vis}/\sqrt{s}$ obtained with ASRC and ECLU definition for data and real detector simulation. w_i, μ_i and σ_i are the results of fits to a sum of two Gaussians as described in the text.

Figures 5.4 and 5.5 compare Data and Monte Carlo for the scaled average visible energy as a function of orientation of event thrust direction and cluster multiplicity respectively for both the algorithms. One finds a better agreement between data and Monte Carlo in case of ECLU. The dependence on the event orientation as well as on cluster multiplicity are reduced as well. Figure 5.6 shows a comparison of cluster multiplicity distribution between data and Monte Carlo for the two methods of energy determination. There is a reasonable agreement for both the algorithms between data and Monte Carlo. A small shift of the data to the higher multiplicity observed in the case of ASRC's holds for ECLU

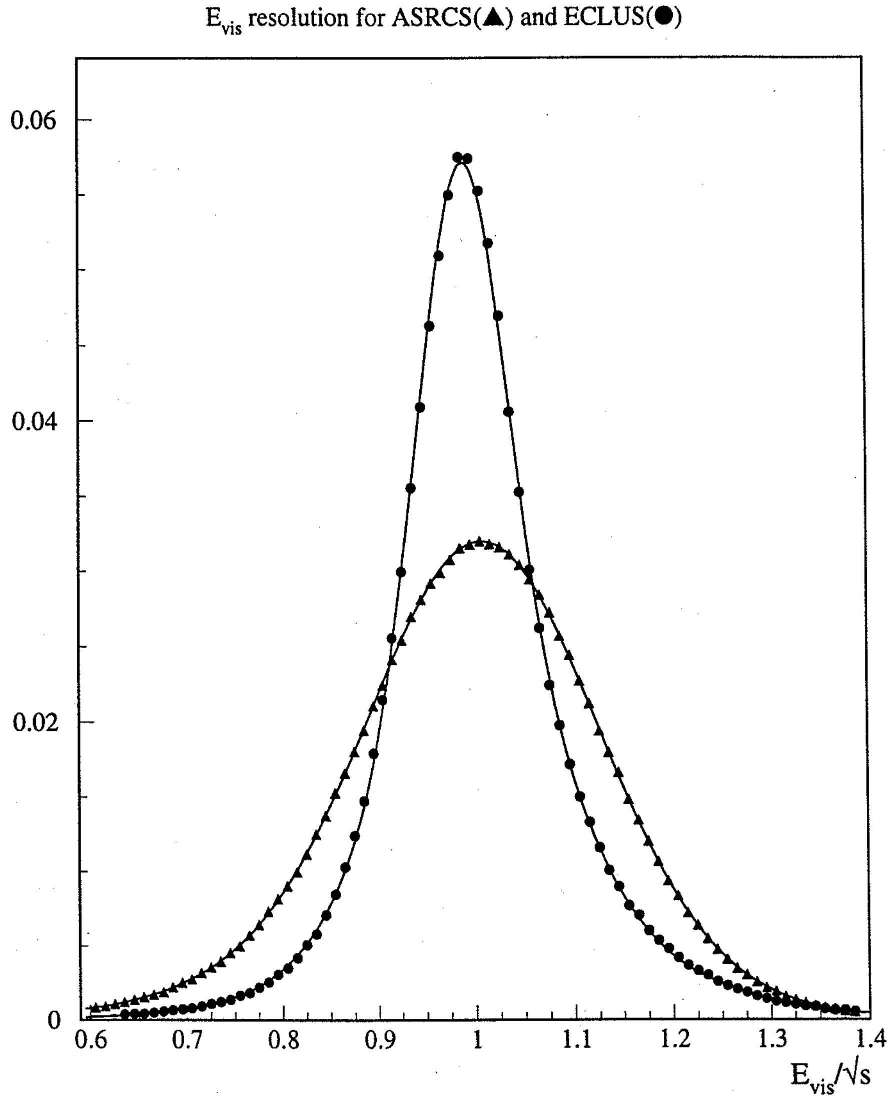

Figure 5.2: Distribution of scaled visible energy for ASRC's and ECLU's. The points correspond to data and the smooth curves are from fits to the distributions to a sum of Gaussians.

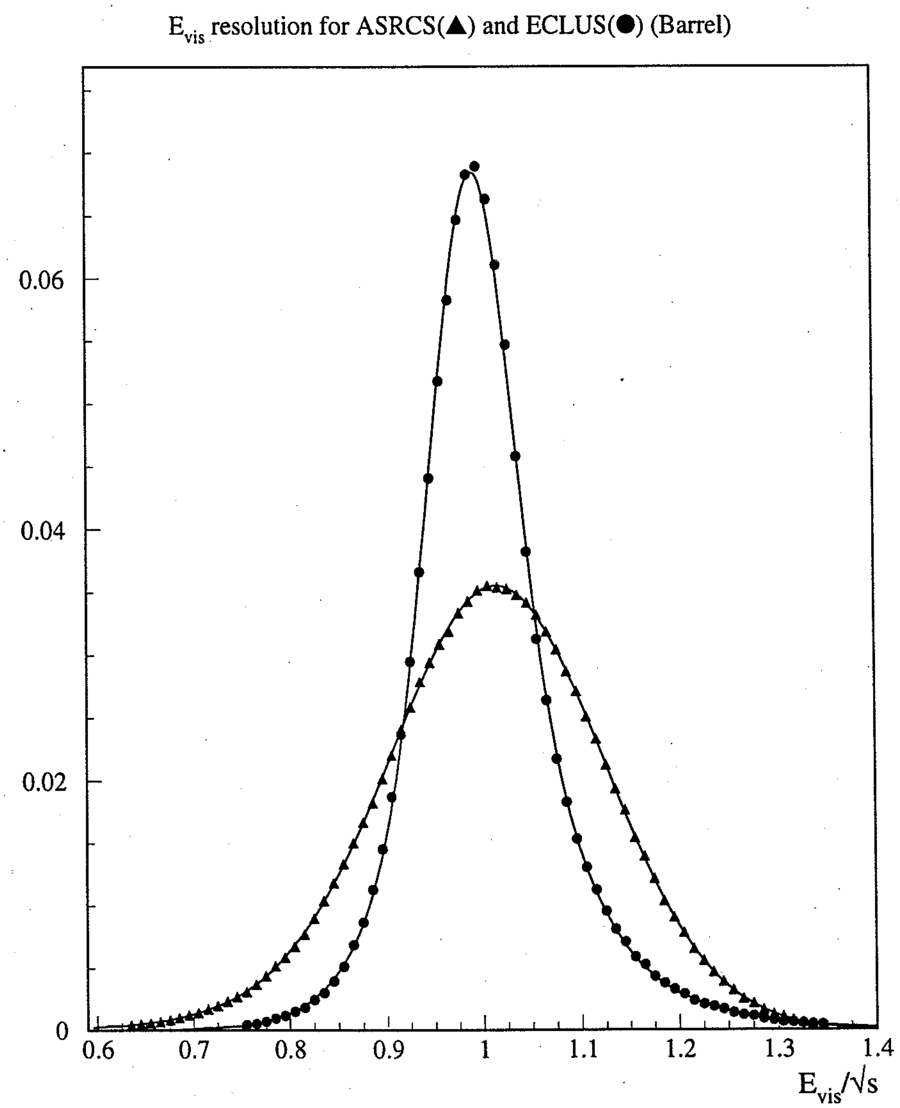

Figure 5.3: Distributions of scaled visible energy for ASRC's and ECLU's for events contained in the central region of the detector ($|\cos\theta_{\mathrm{thrust}}| < 0.74$). The points correspond to 1994 data and the smooth curves are from fits to the distributions to a sum of Gaussians.

Year	Results from the fit					
	w_i		μ_i		σ_i	
	Data	MC	Data	MC	Data	MC
1991	0.45	0.44	1.000	1.015	0.086	0.099
	0.35	0.47	0.985	0.987	0.043	0.048
	0.20	0.09	1.030	1.031	0.165	0.192
1992	0.47	0.44	1.000	1.000	0.085	0.091
	0.33	0.37	0.989	0.989	0.044	0.046
	0.20	0.20	1.022	1.024	0.167	0.162
1993	0.44	0.42	1.001	1.003	0.089	0.088
	0.36	0.39	0.988	0.986	0.045	0.045
	0.20	0.19	1.025	1.025	0.168	0.162
1994	0.46	0.45	0.998	0.999	0.084	0.085
	0.33	0.35	0.986	0.988	0.043	0.044
	0.22	0.21	1.030	1.022	0.166	0.159

Table 5.2: Resolution in $E_{vis}/\sqrt{s}$ obtained with ECLU definition for data and real detector simulation. w_i, μ_i and σ_i are the results of fits to a sum of three Gaussians as described in the text.

Year	Method	RMS Value		Results from the fit					
				w_i		μ_i		σ_i	
		Data	MC	Data	MC	Data	MC	Data	MC
1991	ASRC	0.110	0.114	0.82	0.90	1.019	1.012	0.101	0.108
				0.18	0.10	0.956	0.946	0.139	0.155
	ECLU	0.077	0.077	0.70	0.68	0.988	0.989	0.049	0.049
				0.30	0.32	1.029	1.028	0.112	0.109
1992	ASRC	0.114	0.118	0.82	0.88	1.021	1.014	0.104	0.110
				0.18	0.12	0.948	0.940	0.145	0.157
	ECLU	0.077	0.080	0.69	0.66	0.992	0.990	0.050	0.050
				0.31	0.34	1.024	1.018	0.113	0.114
1993	ASRC	0.114	0.117	0.85	0.90	1.022	1.012	0.106	0.111
				0.15	0.10	0.939	0.947	0.140	0.160
	ECLU	0.078	0.077	0.70	0.70	0.991	0.989	0.050	0.049
				0.30	0.30	1.029	1.027	0.113	0.113
1994	ASRC	0.115	0.117	0.91	0.90	1.017	1.006	0.108	0.111
				0.09	0.10	0.911	0.957	0.142	0.162
	ECLU	0.078	0.079	0.69	0.67	0.989	0.990	0.049	0.050
				0.31	0.33	1.030	1.022	0.113	0.113

Table 5.3: Resolution in $E_{vis}/\sqrt{s}$ obtained with ASRC and ECLU definition for data and real detector simulation for events contained in the central region of the detector ($|\cos\theta_{thrust}| < 0.74$). w_i, μ_i and σ_i are the results of fits to a sum of two Gaussians as described in the text.

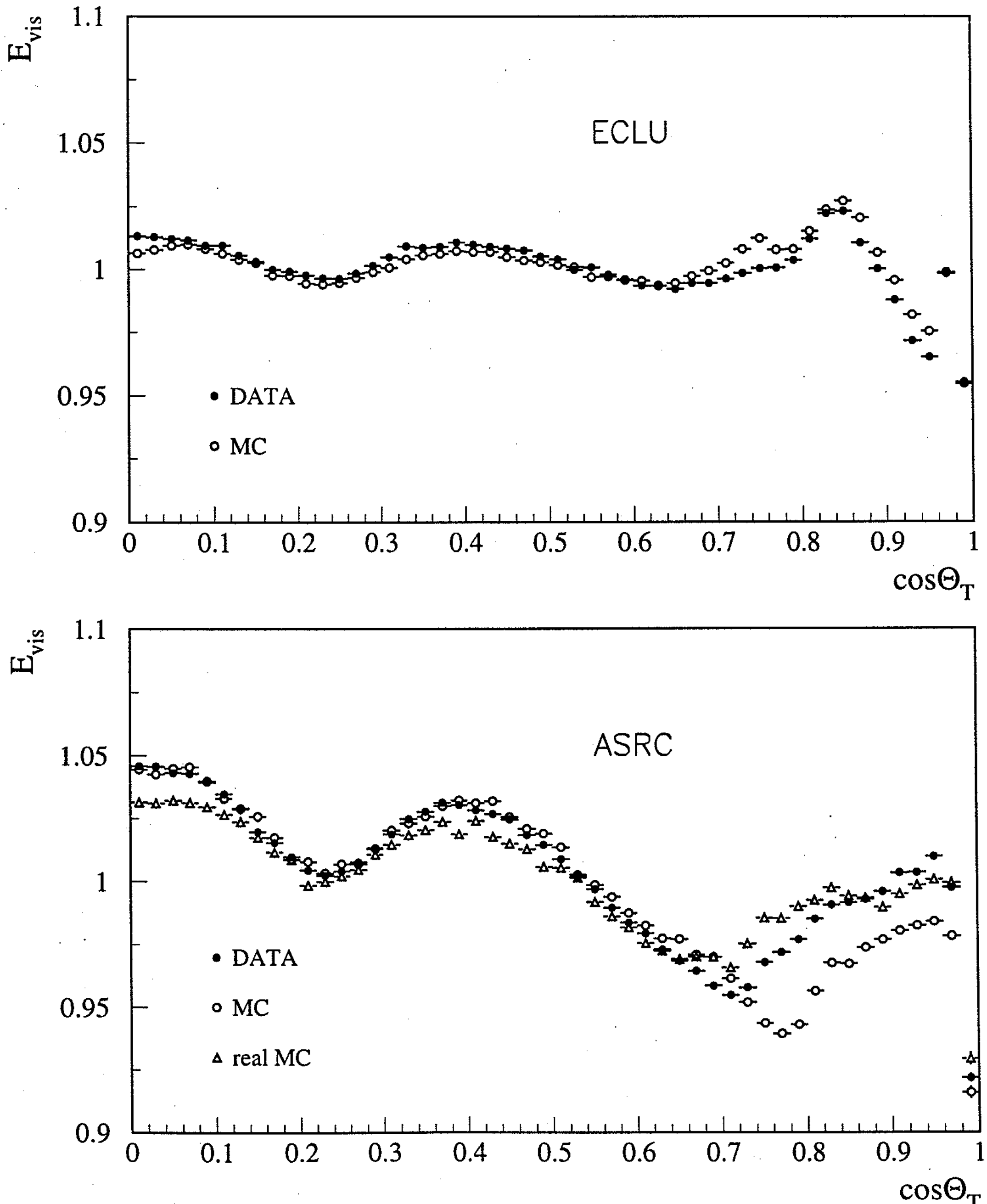

Figure 5.4: Average visible energy as a function of the orientation of the event ($\cos\theta_{\mathrm{thrust}}$) for data and Monte Carlo.

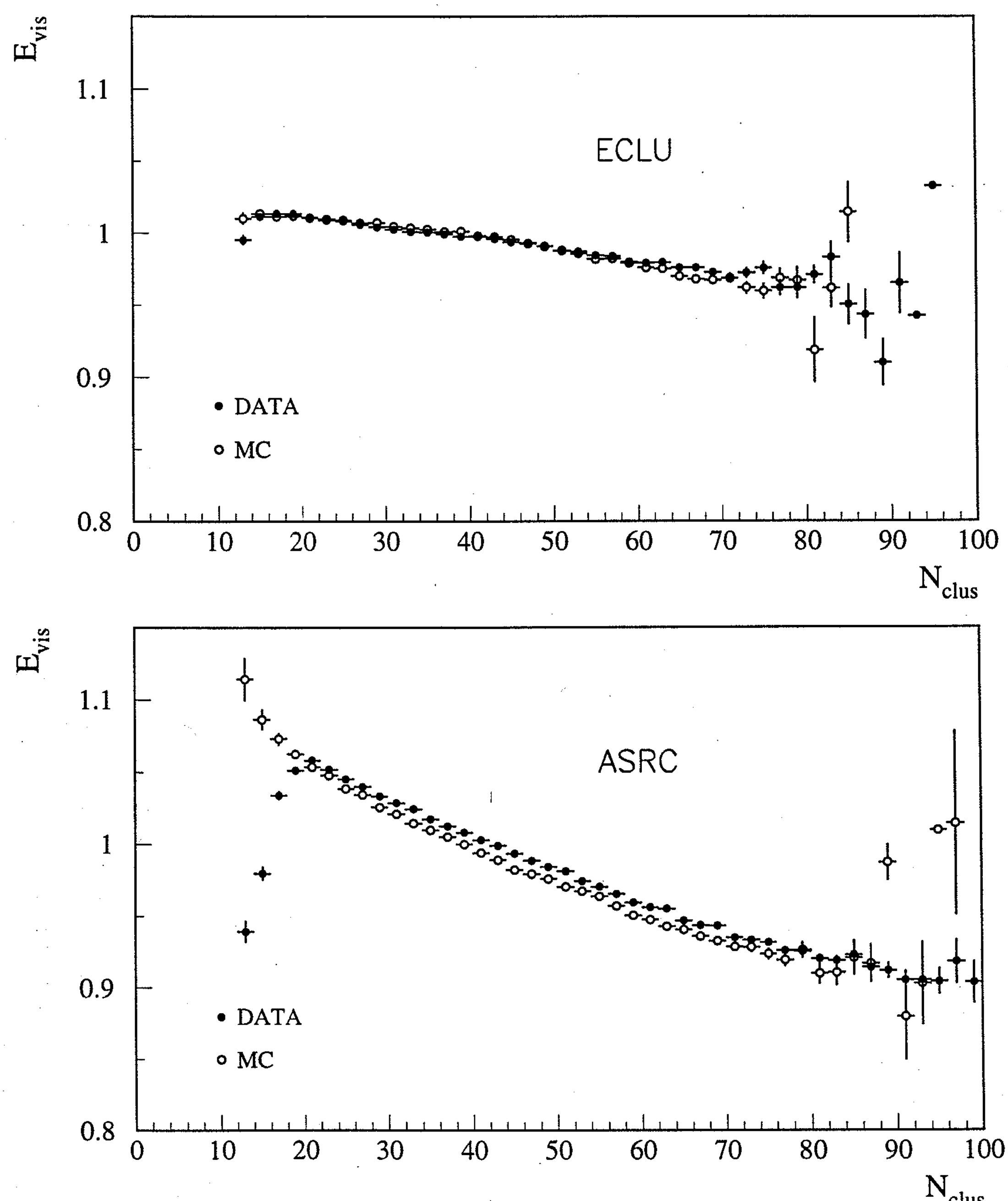

Figure 5.5: Average visible energy as a function of the cluster multiplicity of the event for data and Monte Carlo.

Year	Results from the fit					
	w_i		μ_i		σ_i	
	Data	MC	Data	MC	Data	MC
1991	0.46	0.35	0.997	1.008	0.072	0.087
	0.39	0.56	0.987	0.988	0.040	0.046
	0.15	0.09	1.054	1.060	0.131	0.133
1992	0.48	0.39	0.996	0.993	0.071	0.080
	0.36	0.45	0.992	0.991	0.039	0.043
	0.16	0.16	1.043	1.041	0.131	0.131
1993	0.44	0.43	0.998	0.996	0.074	0.074
	0.41	0.42	0.990	0.988	0.041	0.041
	0.15	0.15	1.052	1.051	0.130	0.131
1994	0.45	0.46	0.998	0.994	0.075	0.074
	0.42	0.37	0.988	0.991	0.040	0.040
	0.14	0.17	1.058	1.043	0.134	0.130

Table 5.4: Resolution in $E_{vis}/\sqrt{s}$ obtained with ECLU definition for data and real detector simulation for events contained in the central region of the detector ($|\cos\theta_{thrust}| < 0.74$). w_i, μ_i and σ_i are the results of fits to a sum of three Gaussians as described in the text.

as well. The mean multiplicity is shifted towards a smaller value for ECLU. This is mainly due to the treatment of the small angle region considered in the algorithm where several clusters are recombined to take care of the detector resolution in that region. Figure 5.7 shows a comparison of average cluster multiplicity as a function of the orientation of the thrust axis. The agreement between data and Monte Carlo is much better in the case of ECLU's.

A sample of Monte Carlo events generated using the WW generator at $\sqrt{s} = 175$ GeV and passed through the L3 detector simulation was studied where the produced W's decay hadronically. The resulting clusters are grouped together into four jets using the Durham algorithm. The y_{cut} in the algorithm is adjusted in such a way so as to always produce 4 jets in the final state. The resulting 4 jets can be combined in three possible ways to reconstruct the W pair. We have chosen a pair by performing a kinematic fit for each of these combinations restricting the masses of the two pairs to be the same and selecting the combination which gives the best χ^2. The measured mass distributions of the selected pair using the two algorithms of energy determination are shown in figure 5.8. A clear improvement in the mass resolution could be observed in the case of ECLU's. Both the distributions show long tail towards low mass. A fit to a Gaussian around the peak has been performed which shows that the resolution in the measured mass distribution improves from 8.9 GeV for ASRC to 5.0 GeV for ECLU's. However, one obtains similar resolution in W mass from both the algorithms after performing the kinematic fit.

The errors estimated on the G-factors can be propagated onto a global variable, such

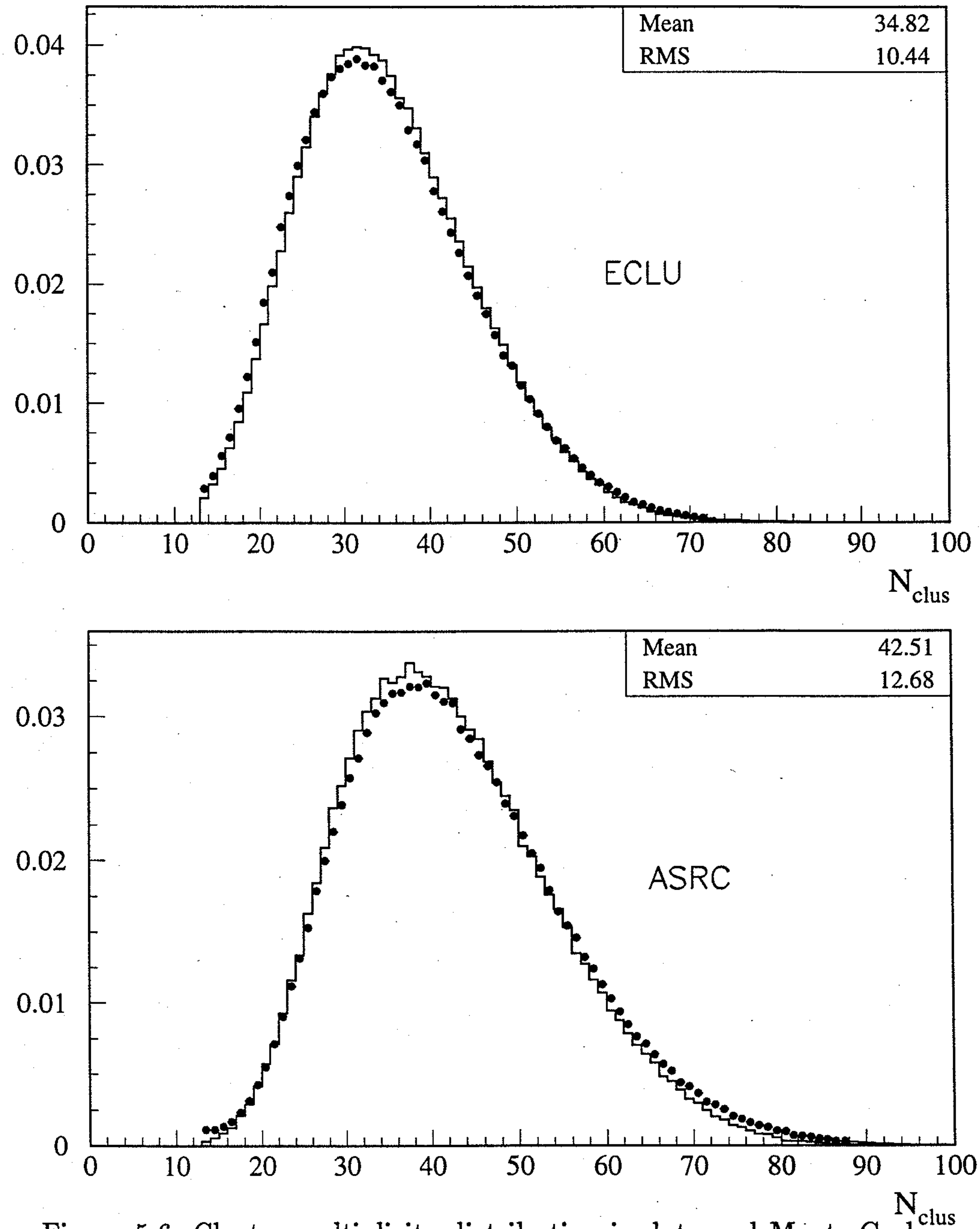

Figure 5.6: Cluster multiplicity distribution in data and Monte Carlo.

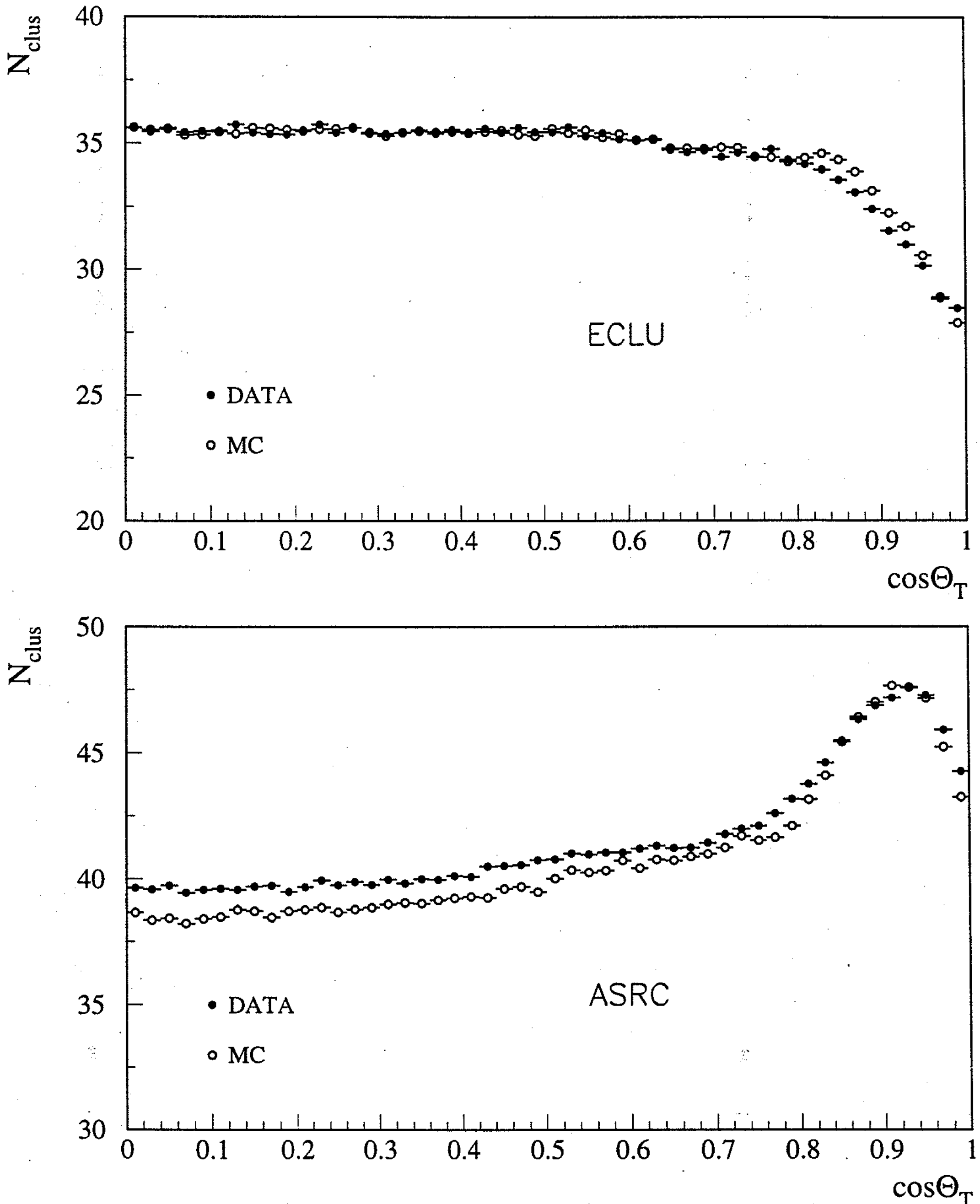

Figure 5.7: Average cluster multiplicity as a function of the orientation of the event ($\cos\theta_{\mathrm{thrust}}$) for data and Monte Carlo.

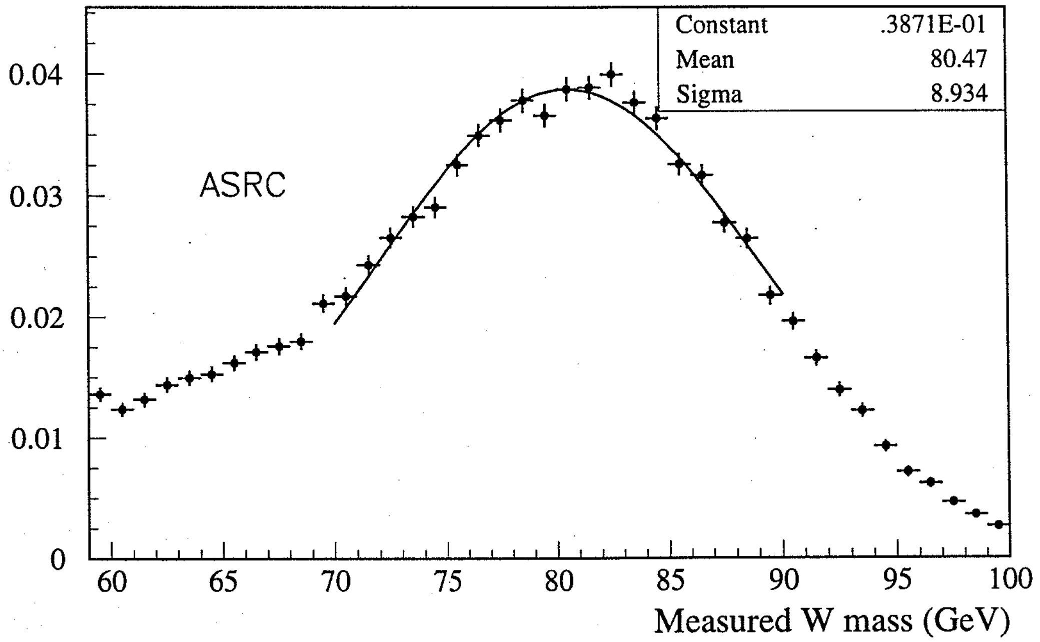

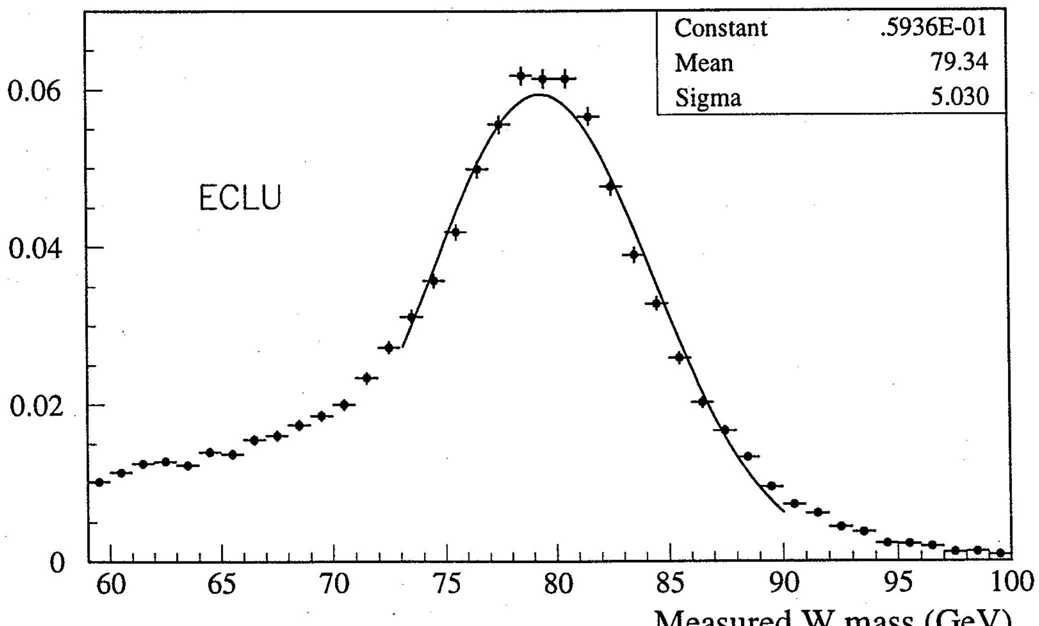

Figure 5.8: Distributions of measured W mass from the WW generator at $\sqrt{s} = 175$ GeV where the W's decay hadronically. The smooth curves are results of fits to a Gaussian in the region around the peak.

as visible energy. The estimated error on the average visible energy due to G-factors is about 0.1 %. This value, to a very good approximation, is independent of year and is the same for both ASRC and ECLU algorithms.

A large amount of hadronic events collected during 1991–1995 LEP running period has made the procedure of determination of G-factors independent of statistical uncertainty. The main source of uncertainty comes from the spread in the average energy collected in the different detector regions. This occurs due to changes in the detector status with time, degradation of calibration etc. On the other hand, during the second phase of running of LEP, only small samples of hadronic events are available for performing calibration which are collected within a short period when the detector conditions and calibration are expected to remain the same. This necessitated a study of the dependence of the errors on G-factors upon statistics which becomes dominant in the second phase of operation of LEP.

We have studied, using the 1994 data sample, the behaviour of the fitting procedure on small number of hadronic Z decays. We observe that for samples of ($\geq$ 1000) events the error propagated to the average visible energy is bounded by the expression

$$\sigma_{\rm g}(\overline{\rm E})/\sqrt{\rm s} \leq 0.1/\sqrt{\rm N}$$

which is applicable to ASRC's and ECLU's. For these samples, the statistical component of the error is expected to be dominant since they belong to the same data taking period. The accuracy obtained in the 1991–1994 G-factor determination ($\sigma_{\rm g}(\overline{\rm E})/\sqrt{\rm s} \simeq 0.1\%$) can thus be achieved even using small hadronic samples ($\sim$ 10000 events).

We have studied if the G-factors obtained at a given centre of mass energy can be used at other centre of mass energies. We found that the linear G-factors for ASRC's can be scaled from one energy to another without significant deterioration in resolution. However, for ECLU's, large extrapolation in centre of mass energy gives wrong energy measurement due to the inherent non-linearity in the energy calibration.

The small number of events required for a consistent determination of the G-factors suggests that the best procedure during the high energy phases of the running of LEP is to perform the calibration using event sample collected at high energy. For ECLU's it is absolutely needed, although for ASRC's one can use events from the calibration run at Z peak as well.

Chapter 6

Hadronic Z Decays with Isolated Photons

The analysis of hadronic events from Z decays with isolated energetic photons in the final state offers a novel opportunity to study quantum chromodynamics over a large range of reduced centre of mass energy. The high energy photons are radiated either through initial state radiation (ISR) or through quark bremsstrahlung before the first gluon branching. The development of hadronic shower, on the other hand, takes place over a larger time scale. As a consequence, hadron production takes place at a lower centre of mass energy which depends on the energy of the emitted photon.

The probability of emission of a photon by a quark at the first branching is quite low compared to the emission of a gluon as described in Section 2.5. Nevertheless, the huge statistics collected by the L3 detector during the running of LEP at $\sqrt{s} \simeq 91$ GeV allow us to select a clean sample of hadronic final states with isolated high energy photons.

At centre of mass energies around m_Z, the initial state radiation and the interference between initial and final state radiation are suppressed. The photons emitted from the initial state are strongly forward peaked and are not visible in the detector. However, ISR photons, which enter the detector are indistinguishable from the photons emitted off the quarks. Events containing such initial state radiation are considered as signal events.

The main source of background to the signal photons comes from neutral hadrons (π°, η°) decaying either into two photons unresolved in the detector or into two well separated photons only one of which is detected within the fiducial volume of the detector. In order to ensure a pure sample of events containing high energetic photon in the final state one needs to apply topological cuts on the photon candidate and to exploit the specific features of the electromagnetic calorimeter to distinguish a single photon from a multi-photon shower.

6.1 Selection of Hadronic Events from Z Decays

Hadronic events are characterised by a large number of charged and neutral particles. Also a large fraction of the total energy is visible in the detectors. One can use these two criteria to distinguish hadronic Z decays from other Z decay modes which may appear as potential backgrounds at $\sqrt{s} \simeq 91$ GeV. The events used in the study have been collected by the L3 detector during the running period of LEP from 1991 to 1994. The corresponding integrated luminosity is 110.9 *ipb*. The bulk of the data (90.2 *ipb*) corresponds to $\sqrt{s} =$ 91.2 GeV and the remaining part comes from the LEP energy scan ($\sqrt{s}$: 88 to 93 GeV).

6.1.1 Online Trigger

An event must be accepted by the online trigger system, in order for it to be recorded for further analysis. Hadronic events are identified by the logical OR of the level 1 energy, TEC, and scintillation counter triggers. These three triggers have efficiencies of 99 %, 95 % and 95 % respectively. The energy trigger requires either a total energy of at least 25 GeV in the calorimeters, or a minimum energy of 15 GeV in the central region ($42° < \theta < 138°$) of electromagnetic and hadron calorimeters or 8 GeV in the electromagnetic calorimeter alone. The requirement of the TEC trigger is at least two tracks identified with a maximum acolinearity of 60°. The scintillation counter trigger requires a coincidence of at least 5 hits in the counters during a 30 ns interval, which must extend over an azimuthal angular region of at least 90°.

To be recorded as a hadronic event, an event must be selected by at least one of the first level triggers described above. The second and third levels of the trigger system filter events to reject those due to cosmic rays, electronic noise, and beam-gas interactions. The overall efficiency for selecting hadronic Z decays by the online trigger is greater than 99.9 %.

6.1.2 Offline Selection

Depending on the characteristics of an event the L3 reconstruction algorithm uses loose selection criteria to classify each event into one or more categories of Z decay which is technically known as *physics split stream*. This is done to ease the subsequent physics analysis. The hadronic Z decays fall in QQ stream. A single event at this stage can be assigned to more than one physics split stream.

Only those events are used for the analysis which were collected during the running period when all the relevant detector components were operating normally. We consider the electromagnetic and the hadron calorimeters, the tracking chamber and the luminosity monitor to be the most relevant detectors for this analysis. These detectors must be operating normally for the events we use for the analysis. In addition the global data acquisition (DAQ) system and the energy trigger should also work properly during the data taking period. One can retrieve all these informations from online databases to reject events for which the above detectors or the other relevant components did not work normally. A number of events collected over a time interval, during which detector conditions do not change, constitute a *run*. If a large number of events in a particular run are bad we call that a *bad run* and remove it from the analysis. We reject events further by demanding that the BGO should not be excessively noisy for any event.

The selection of hadronic events from Z decays is accomplished in two complementary ways using events from the QQ stream. The first method is based on the energy measurements in the electromagnetic and hadron calorimeters whereas the second method uses reconstructed tracks for energy measurement. The first method is more efficient over a larger fiducial volume. Therefore, the track based selection is used for cross checking the principal selection procedure independently and for systematic studies related to event selection.

In both the calorimeter and track based selection methods, a set of energy vectors, $\{\vec{\mathcal{E}}_{\rm i}\}$, are computed for reconstructed clusters or tracks. For the calorimeter based approach the energy vectors are reconstructed from the energy and angles of the reconstructed smallest resolvable clusters which have been introduced in Section 4.2. The energy of a smallest resolvable cluster is given by

$$\mathrm{E_{cluster}} = \sum_{\rm j} \mathrm{G_j} \cdot \mathrm{E_j^{Raw}}$$

where $\mathrm{E_j^{Raw}}$ is the raw energy in a particular detector region and $\mathrm{G_j}$ is the G-factor for the corresponding detector region. For the present analysis we have used linear G-factors with the electromagnetic option because we are concerned with the precise determination of the energy of the photon. Aspects of G-factors are described in detail in Chapter 5.

The energy vectors are then used to compute the total visible energy ($\mathrm{E_{vis}}$) and the missing energy vector ($\vec{\mathcal{E}}_{\rm miss}$) of the event as

$$\begin{aligned} \mathrm{E_{vis}} &= \sum_{\rm i} |\, \vec{\mathcal{E}}_{\rm i} \,| \\ \vec{\mathcal{E}}_{\rm miss} &= -\sum_{\rm i} \vec{\mathcal{E}}_{\rm i} \end{aligned}$$

The energy imbalances along and transverse to the beam direction can be defined as

$$\begin{aligned} \mathrm{E}_{\|} &= |\, \hat{\mathrm{z}} \cdot \vec{\mathcal{E}}_{\rm miss} \,| \\ \mathrm{E}_{\perp} &= \sqrt{(\hat{\mathrm{x}} \cdot \vec{\mathcal{E}}_{\rm miss})^2 + (\hat{\mathrm{y}} \cdot \vec{\mathcal{E}}_{\rm miss})^2}, \end{aligned}$$

where $\{\hat{x}, \hat{y}, \hat{z}\}$ are the three unit vectors in the orthogonal cartesian coordinate system.

With the calorimeter based approach, events are accepted as hadronic if

$$0.6 < \frac{\mathrm{E_{vis}}}{\sqrt{\mathrm{s}}} < 1.4 \quad , \quad \frac{|\,\mathrm{E}_{\parallel}\,|}{\mathrm{E_{vis}}} < 0.40 \quad , \quad \frac{|\,\mathrm{E}_{\perp}\,|}{\mathrm{E_{vis}}} < 0.40 \quad , \quad \mathrm{N_{cluster}} > 12$$

where $\mathrm{N_{cluster}}$ is the number of clusters with energy larger than 100 MeV. The cut on $\mathrm{N_{cluster}}$ removes low multiplicity $\tau^+\tau^-$, e^+e^- and $\mu^+\mu^-$ events, whereas the 2 photon events, for which total visible energy is low, are removed by the cut on $\mathrm{E_{vis}}$. Cuts on $\mathrm{E}_{\parallel}$ and $\mathrm{E}_{\perp}$ select only well balanced events.

Figures 6.1–6.4 show the distribution of each of the selection variables with all other cuts applied. The hatched regions shown are the contribution from background whereas the empty region indicates the signal. The Monte Carlo predictions are shown one on top of the other so that the final histograms can be compared directly to data. All the Monte Carlo predictions are normalised by the number of selected hadron events.

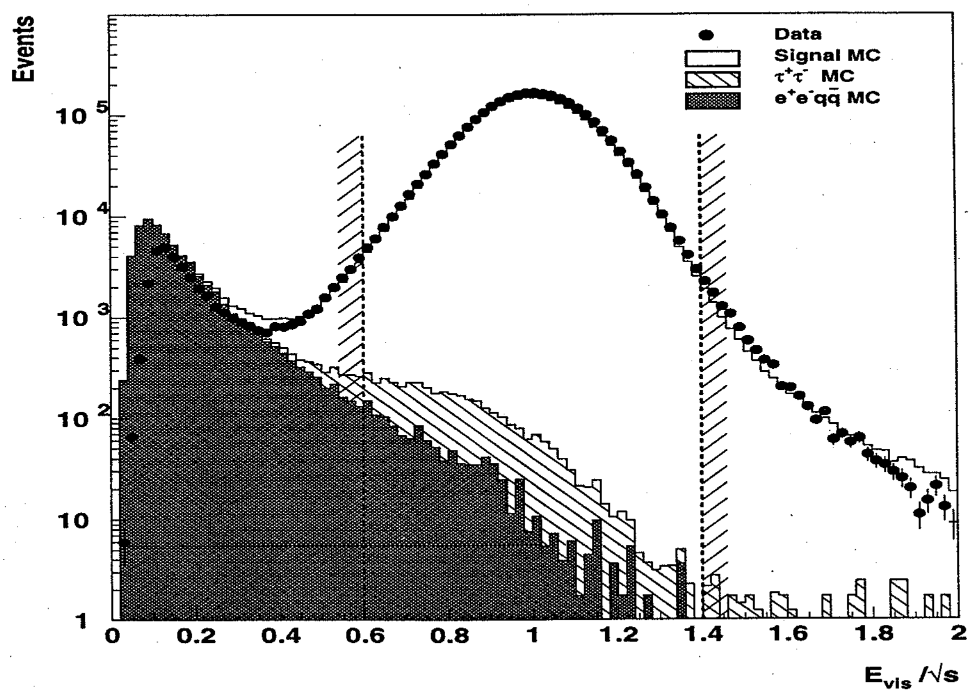

Figure 6.1: Scaled visible energy after all cuts except the one on the visible energy have been applied.

With these cuts, one obtains a total of 2990 K hadronic events from the entire data sample. A study of more than 3000 K simulated JETSET [48] Monte Carlo events reveals that 98 % of hadrons are selected by these cuts. A study of about 700 K simulated HERWIG [51] events gives a selection efficiency of 97 %. A small background of 0.2 %

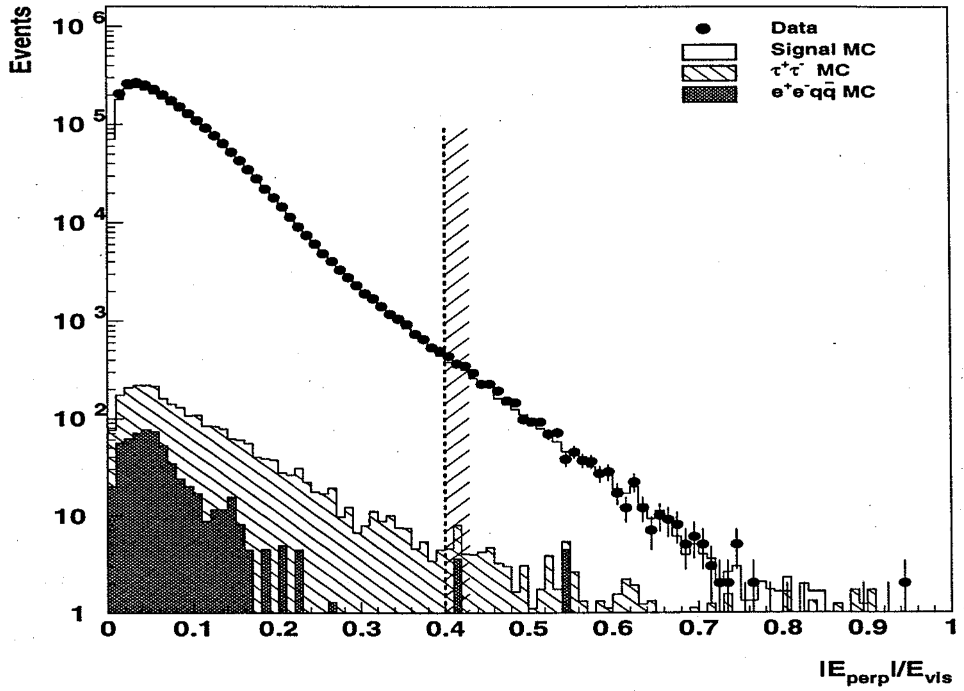

Figure 6.2: Transverse energy imbalance with all other selection cuts applied.

from $\tau^+\tau^-$ and four fermion final states from 2 photon processes has been estimated to be contained in the selected data sample from studies of KORALZ [58] and DIAG36 [59] Monte Carlo events respectively.

A large number of parameters in the Monte Carlo Programme JETSET have been optimised using L3 data. Hence JETSET is expected to provide a more reliable description of data in L3. For this reason, a much larger number of simulated JETSET events exist in L3. We, therefore, consider JETSET as the principal QCD Monte Carlo for all comparisons with L3 Data and use HERWIG only for cross checking the result and studying the effect of a different fragmentation model.

For the track based selection, the momentum vectors and consequently the absolute momentum sum (E^T_{vis}), the longitudinal ($E^T_{\parallel}$) and the transverse ($E^T_{\perp}$) momentum imbalances are determined from the momentum and direction of the reconstructed tracks. We select good charged tracks by requiring at least 40 r$-\phi$ hits (out of 62 wires), a distance of closest approach to the interaction point (DCA) of less than 50 mm in the plane perpendicular to the beam axis, and momentum transverse to the incoming beam directions of larger than 100 MeV. We select hadronic events with the following requirements,

$$0.15 < \frac{E^T_{vis}}{\sqrt{s}} \quad , \quad \frac{|E^T_{\parallel}|}{E^T_{vis}} < 0.75 \quad , \quad \frac{|E^T_{\perp}|}{E^T_{vis}} < 0.75 \quad , \quad N_{track} > 4$$

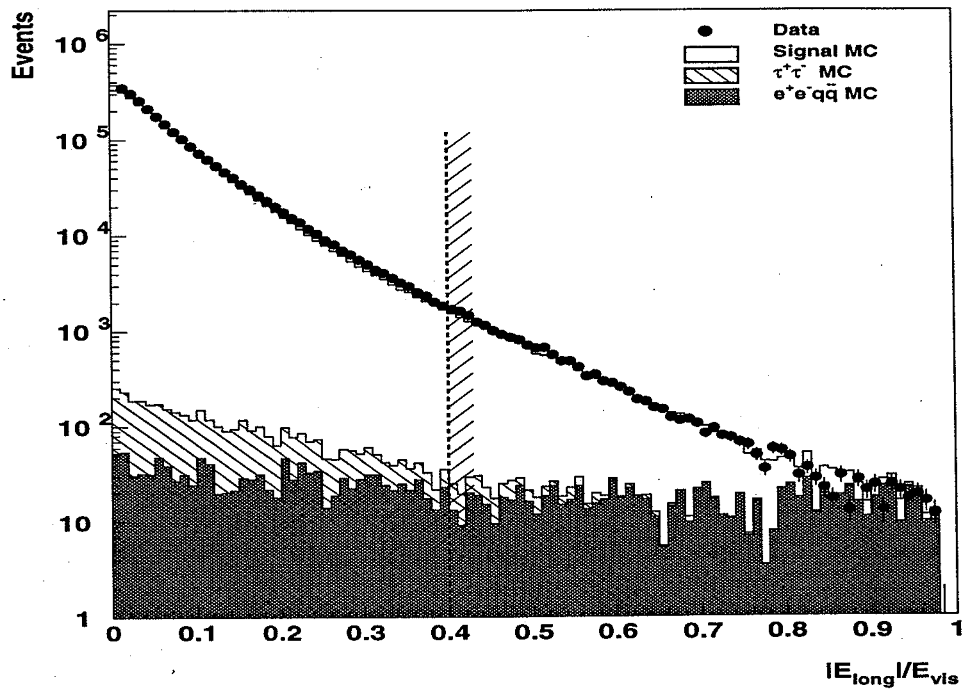

Figure 6.3: Longitudinal energy imbalance with all other selection cuts applied.

where N_{track} is the number of reconstructed charged tracks having the required qualities. For the track based selection an additional cut has been applied. The differences in azimuthal angle between azimuthally adjacent pairs of tracks are computed. The second largest of these differences must not be greater than 170°.

Table 6.1 summarises the selection of hadronic events using both track and calorimeter based selection methods for data collected by L3 during the LEP running period from 1991 to 1994.

6.2 Selection of Photon Candidates

After selecting a sample of hadronic events, next we try to identify events with one or more isolated energetic photons. The average number of photons in the final state in a multi-hadronic event is about 20. Most of them are inclusive photons coming from decays of neutral hadrons. An energetic isolated *photon* candidate is a cluster in the electromagnetic calorimeter which

- has energy larger than 5 GeV,

- lies in an efficient sector of the tracking chamber with no associated charged track,

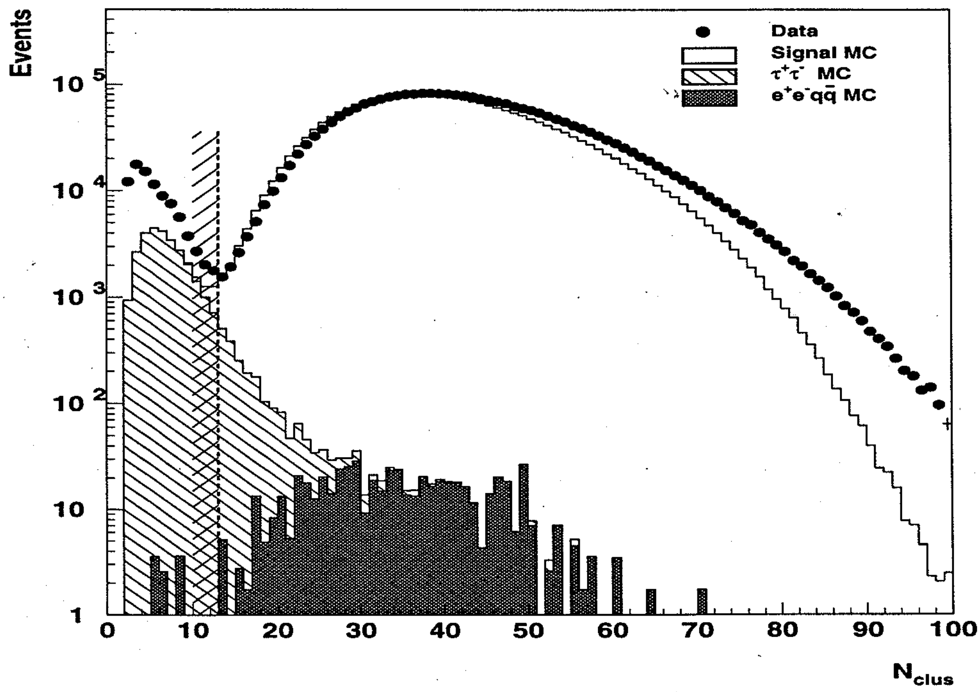

Figure 6.4: Distribution of number of calorimetric clusters with all other selection cuts applied.

Year	1991	1992	1993	1994	Total
QQ Stream Selection	378 K	734 K	763 K	1673 K	3548 K
Track Selection	248 K	546 K	572 K	1252 K	2618 K
Fraction(%)	65.6	74.4	75.0	74.8	73.8
Calorimetric Selection	296 K	628 K	645 K	1428 K	2997 K
Fraction(%)	78.3	85.6	84.5	85.4	84.5

Table 6.1: Summary of hadronic event selected for data collected during 1991–1994. The first row gives the number of events selected by the QQ stream. The next rows give the number and fraction (of the events selected by QQ stream) of event selected by the track and calorimetric methods respectively.

– has a lateral shower profile compatible with an electromagnetic shower. Clusters of electromagnetic origin are selected with a loose selection cut $E_9^c/E_{25}^c > 0.75$, where E_9^c (E_{25}^c) is the corrected energy in the 3×3 (5×5) crystal array around the central one.

– is isolated from the other clusters in the electromagnetic calorimeter. We require that no other cluster with energy ($E_{\alpha_{LI}}$) above 500 MeV is in a cone of half angle (α_{LI}) 15° around the candidate direction.

Figure 6.5 shows the distribution of the local isolation angle of the photon with respect to the nearest bump for the pre-selected sample. We select photon candidates within

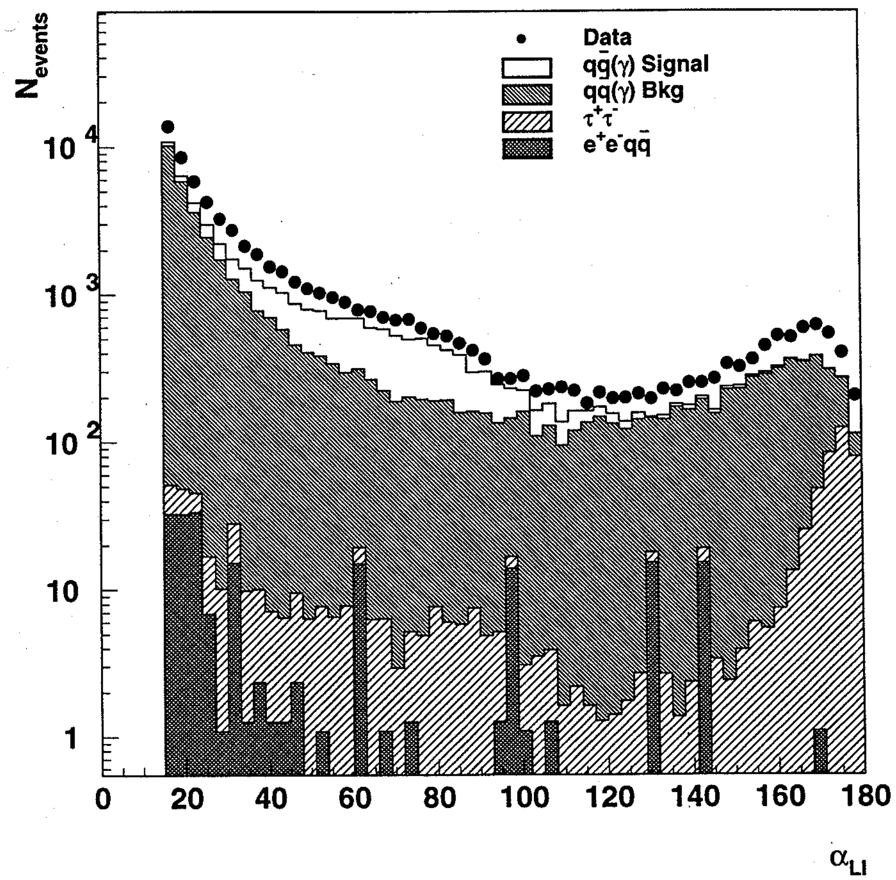

Figure 6.5: Local isolation angle of the selected bump with respect to the nearest bump.

the barrel ($42.3° < \theta < 137.7°$) and endcap ($11.6° < \theta, (180° - \theta) < 38°$) electromagnetic calorimeters.

A typical hadronic event with a high energy isolated photon which satisfies all the above mentioned conditions is shown in figure 6.6. The event is displayed in the plane transverse to the beam direction.

A bump in the electromagnetic calorimeter is matched with a track in the tracking chamber to reject bumps due to charged tracks using standard L3 reconstruction algorithm. Each of the tracks is extrapolated to the centre of gravity of the bump under consideration in the electromagnetic calorimeter where the azimuthal angular distance between the track and the bump $|\Delta\phi|$ is calculated. A bump is considered to be neutral if $|\Delta\phi| > 10\,\mathrm{mrad}$.

The clusters should lie in an efficient sector of the tracking chamber because if the tracking chamber does not work a charged bump may fake a neutral one. We use the standard information of the high voltage status of the ϕ sectors of the tracking chamber with time and reject a bump if it falls in a bad sector of the tracking chamber.

Figure 6.7 shows the correlation of the polar and azimuthal angles of the bumps in the electromagnetic calorimeter for 1994 data and the *real detector* simulated Monte Carlo events corresponding to the year 1994 where all the time dependent detector inefficiencies which are observed in 1994 data where simulated in detail.

From the above loose pre-selection of photon candidates we obtain 81177 events of which 48885 have the cluster in the barrel electromagnetic calorimeter ($|\cos\theta_\gamma| < 0.70$).

The energy spectrum of the *photon* candidates is shown in figure 6.8(a). This energy distribution of the photon can be translated into the reduced centre of mass energy distribution of the remaining hadronic subsystem after the removal of the photon as

$$\sqrt{\mathrm{s}'} = \sqrt{\mathrm{s}\left(1 - \frac{2\mathrm{E}_\gamma}{\sqrt{\mathrm{s}}}\right)}$$

where $\sqrt{\mathrm{s}}$ is the nominal centre of mass energy and $\sqrt{\mathrm{s}'}$ is the reduced centre of mass energy. The distribution of the reduced centre of mass energy is shown in figure 6.8(b).

Before we proceed further, we divide the whole data sample in different intervals of the candidate photon energy or equivalently in several reduced centre of mass energy bins which is motivated by the physics we are going to explore later on. We divide the $\sqrt{\mathrm{s}'}$ spectrum into six subdivisions so that each energy region has reasonable statistics. The energy regions and the corresponding number of pre-selected events are summarised in table 6.2. The table summarises the initial purities of the pre-selected sample as well.

The background to the direct photons is dominated by photons coming from neutral hadron (π^0 and η) decays. The pre-selected sample contains an overwhelming amount of neutral hadron contamination at this stage. To reduce this background, we need to exploit the specific characteristic of the electromagnetic calorimeter and devise other sophisticated isolation cuts.

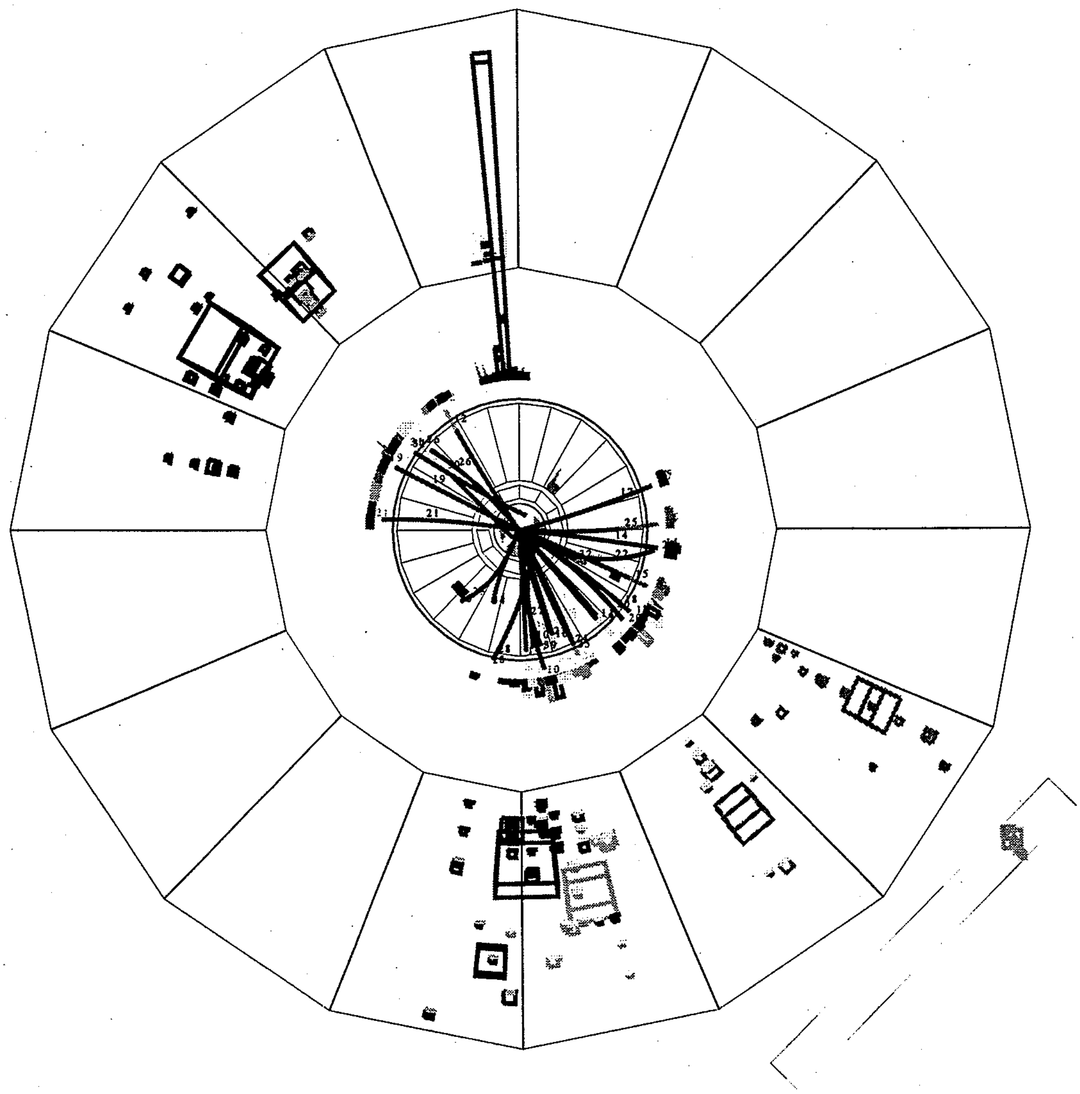

Figure 6.6: A candidate hadronic event with an energetic isolated photon in the final state is shown in the plane transverse the beam direction. Evidently, there is no charged track associated with the candidate. The candidate is fairly isolated from other particles in the events.

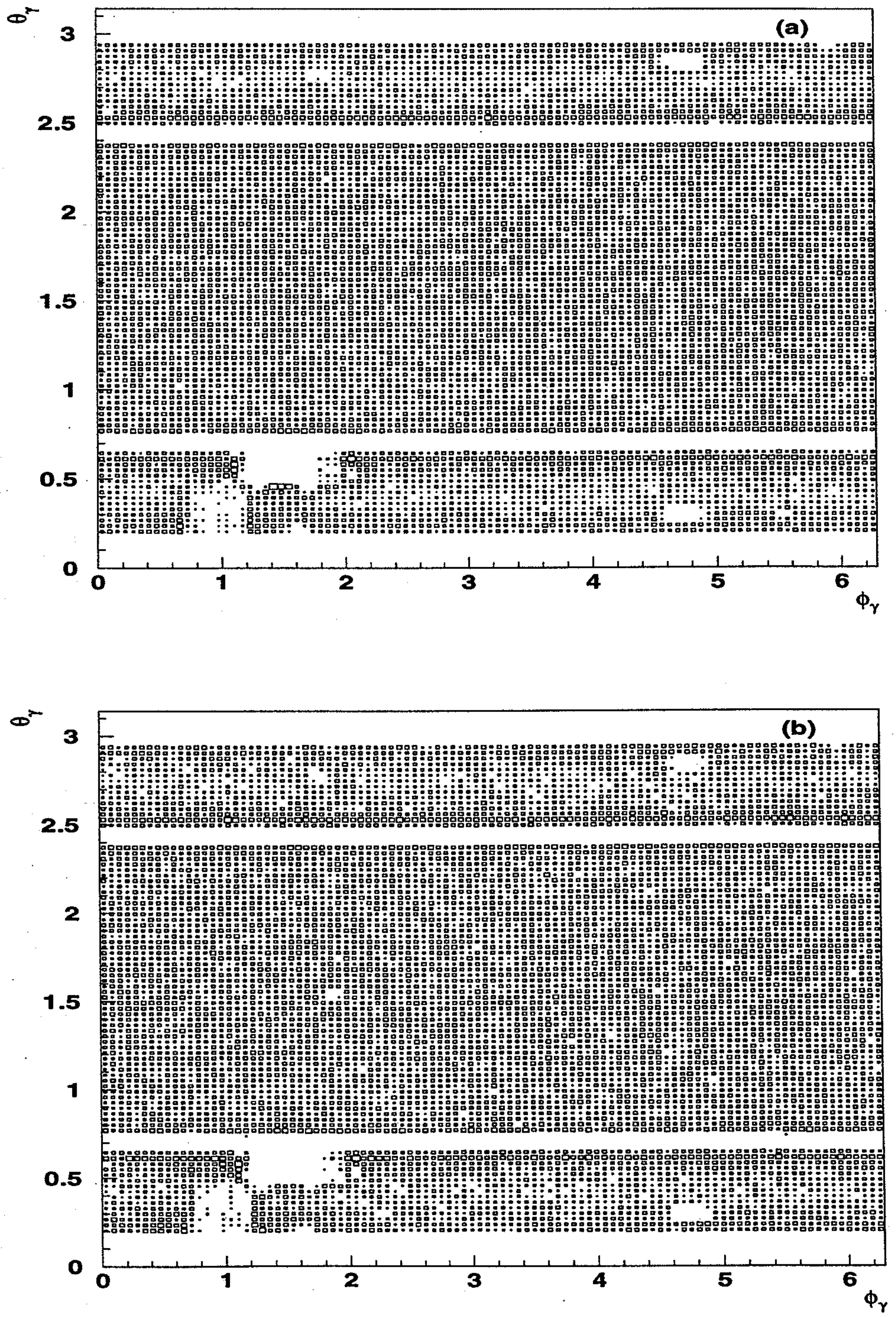

Figure 6.7: $\theta - \phi$ map of the crystals in the electromagnetic calorimeter for (a) 1994 data and (b) Monte Carlo events which are real detector simulated for the same year.

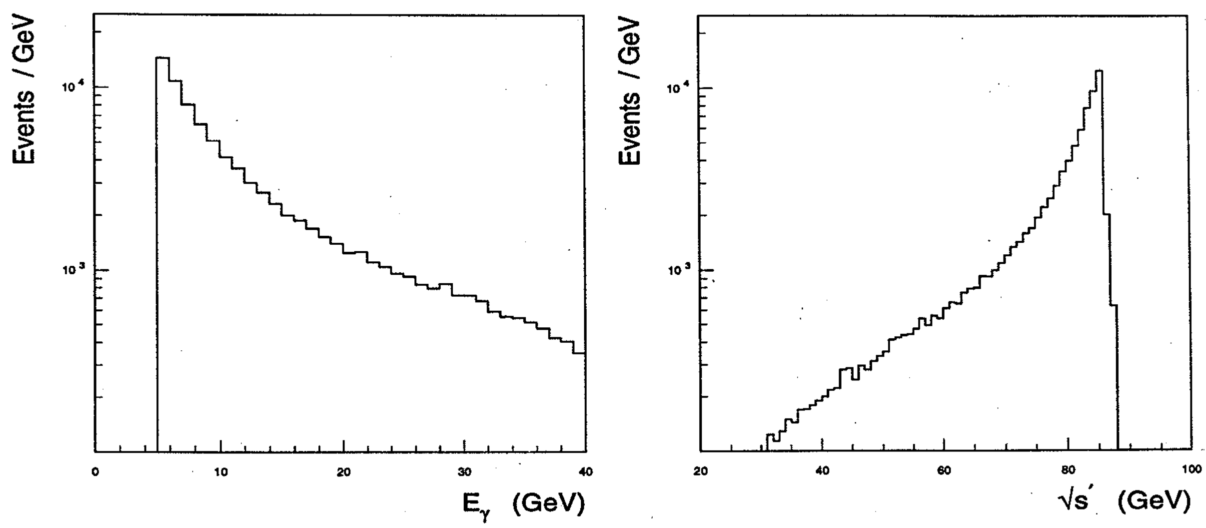

Figure 6.8: Measured distribution of (a) energy of the *photon* candidate, (b) centre of mass energy of the remaining hadronic system ($\sqrt{s'}$).

We require that the shower should be further isolated and the shower shape should be compatible with electromagnetic shower generated by a single photon.

We construct other isolation variables like the minimum angle of the candidate photon with the nearest jet, reconstructed from the remaining hadronic system using JADE algorithm [60] with $y_{cut} = 0.05$, which we call jet isolation angle, α_{JI}. Jets are reconstructed in the angular region $5^\circ < \theta < 175^\circ$. We also look into the energy ($E_{\alpha_{LI}}$) of individual clusters within the local isolation cone.

We use a shower shape discriminator, p_γ based on artificial neural network [61] to distinguish single photon shower from multi-photon ones in the electromagnetic calorimeter. The neural network study results in a uniform distribution of the discriminator (p_γ) in the region 0$-$1 for isolated single photons. Therefore application of a cut on the minimum value of p_γ gives an efficiency for selecting isolated single photons equal to $1 - p_\gamma$ which is independent of photon energy. The distribution of the discriminator peaks sharply at zero for backgrounds due to isolated neutral hadrons. Figure 6.9 shows the distribution of the shower shape discriminator, p_γ, with all other cuts applied.

We tune the cut values for the following selection variables defined above separately for photon candidates in the six different energy ranges:

(a) shower shape discriminator, p_γ,

(b) size of the local isolation cone, α_{LI},

(c) jet isolation angle, α_{JI},

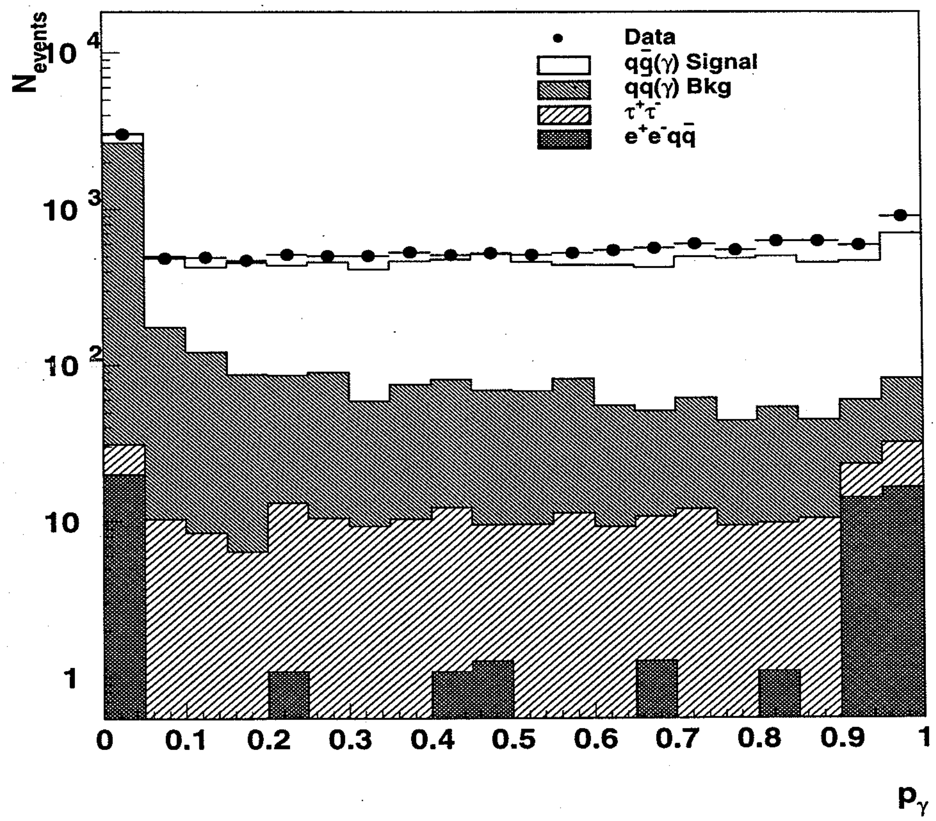

Figure 6.9: Distribution of shower shape discriminator, p_γ, with the other selection cuts applied in the finally selected event sample. The various Monte Carlo distributions are shown cumulatively so that the final histograms (solid line) represents the total Monte Carlo contribution and can be directly compared with data.

(d) energy of individual clusters within the local isolation cone, $E_{\alpha_{LI}}$.

The purity of the photon signal and the efficiency of selection are optimised using 3 million JETSET 7.4 parton shower events processed through the full L3 detector simulation programme. The isolation angles have been chosen to be energy dependent in order to optimise efficiency and purity, whereas the energy cutoff $E_{\alpha_{LI}}$ is fixed at 50 MeV and shower shape discriminator is bounded within $0.10 < p_\gamma < 0.95$ (keeping 85% of γ's passing all other cuts) for all energy points. One selects photons from ISR or FSR with efficiency between 35 % and 65 % depending on its energy whereas the purity is better than 75 % at all energies. The cuts as well as the number of events in the finally selected sample are summarised in table 6.2. The most important source of background is due to misidentified hadrons or photons coming from hadronic decays. This has been studied using JETSET 7.4 PS Monte Carlo with complete detector simulation. As observed in

$\sqrt{s'}$ (GeV)	30–50	50–60	60–70	70–80	80–84	84–86
Initial Statistics	3800	4114	7035	16791	18758	18931
Initial Purity(%)	26	26	26	14	9	6
Local Isolation Angle (α_{LI})	15°	15°	15°	15°	21°	24°
Jet Isolation Angle (α_{JI})	20°	20°	20°	20°	21°	24°
Selection Efficiency	0.63	0.55	0.51	0.46	0.40	0.35
Background Scale Factor	1.51 ± 0.2	1.18 ± 0.2	0.95 ± 0.2	1.57 ± 0.1	2.02 ± 0.1	2.45 ± 0.2
π°,η° Background (%)	23	12	8	9	9.5	14
$\tau^+\tau^-$ Background (%)	2	2	2	2	2	2
$e^+e^-q\bar{q}$ Background (%)	0	0	0	0.5	0.5	0.5
Final Statistics	913	815	1193	2326	1792	1440
Final Purity(%)	75	86	90	89	88	84

Table 6.2: Summary of event selection and background estimation.

our earlier studies [62], the absolute rate of the isolated neutral hadron background is not well described in the Monte Carlo. This has been re-estimated from data by selecting a background sample (using $p_\gamma < 0.10$) with the same energy and isolation cuts as the γ sample and then comparing with Monte Carlo. As only 10 % of the true single photons lies within $p_\gamma < 0.10$ we may assume that the signal part is well described in this isolated background enriched sample. The following expression is used to obtain the so called *background scale factor*, for different energy regions

$$F_{BG} \quad = \quad \frac{N_{Had}^{\pi^\circ,\eta^\circ}(\mathrm{Data}) - N_{FSR+ISR}(\mathrm{JETSET})}{N_{BG}^{\pi^\circ,\eta^\circ}(\mathrm{JETSET})}$$

For JETSET 7.4 PS Monte Carlo, one gets an overall normalisation factor between 0.95 ± 0.1 and 2.4 ± 0.2 depending on the reduced CM energy.

Backgrounds due to $\tau^+\tau^-$ and 2 photon events have been estimated using tau and two photon Monte Carlo samples normalised to the same number of selected hadronic events. The level of backgrounds in the six energy regions are summarised in table 6.2. The background events which pass all the selection cuts cannot be distinguished from the signal on an event by event basis and have to be subtracted statistically from the selected event sample.

6.3 Event Shape Variables

Once the photon is removed from the system the remaining hadronic subsystem is boosted in the centre of mass frame of the subsystem using the well measured energy and angle of the isolated photon. Event shape variables described in Section 2.4 are calculated after the boost. The variables studied here are event thrust (T) [16], scaled heavy jet mass ($\rho \equiv M_H^2/s$) [19] and total (B_T) and wide (B_W) jet broadenings [25] for which improved perturbative QCD calculations (resummed $\mathcal{O}(\alpha_s{}^2)$) exist.

Figure 6.10 shows uncorrected thrust distributions measured at the six energy bins compared to Monte Carlo predictions after normalising to the same number of hadrons. The different shaded areas indicate the backgrounds from fragmentation in hadronic sample, $\tau^+\tau^-$ and (e^+e^-+ hadrons). One sees reasonable agreement between the measured distribution and the expectation from Monte Carlo programmes (in this comparison, the hadronic background has been rescaled). Similar agreement is observed in other measured distributions.

6.4 Correction of Data

The measured distributions are then corrected for backgrounds and detector effects (resolution and acceptance) on a bin-by-bin basis. The background corrected distribution is obtained subtracting the shape of the background for a particular distribution from the raw distribution.

The effect of the detector resolution has been studied by comparing the event shape variables of accepted JETSET 7.4 PS Monte Carlo events before and after detector simulation. The resolution correction factor for a particular bin in the distribution of a variable is defined as

$$C^{i}_{res} = \frac{N^{i}_{Det}}{N^{i}_{Gen}}$$

where N^{i}_{Det} is the number of events that fall in the i th bin of a distribution in the Monte Carlo event sample at the detector level and N^{i}_{Gen} is the corresponding number at the particle level. These events have been selected using the event information at the detector level.

Data are corrected for detector acceptance also using JETSET 7.4 PS Monte Carlo programme. For the acceptance correction we take a ratio, at the particle level, of all the signal events to the selected events, for a particular bin of the distribution:

$$C^{i}_{acc} = \epsilon \, \frac{N^{i}_{Total\,Gen}}{N^{i}_{Selected\,Gen}} .$$

We normalise the total signal events to the number of signal events selected using

$$\epsilon = \frac{N_{Selected\,Gen}}{N_{Total\,Gen}}.$$

The fluctuations in the correction factors can be smoothened in different ways. The data, corrected for all the above effects, can be directly compared to the corresponding distribution predicted by any theoretical model at the particle level without any initial and final state radiation.

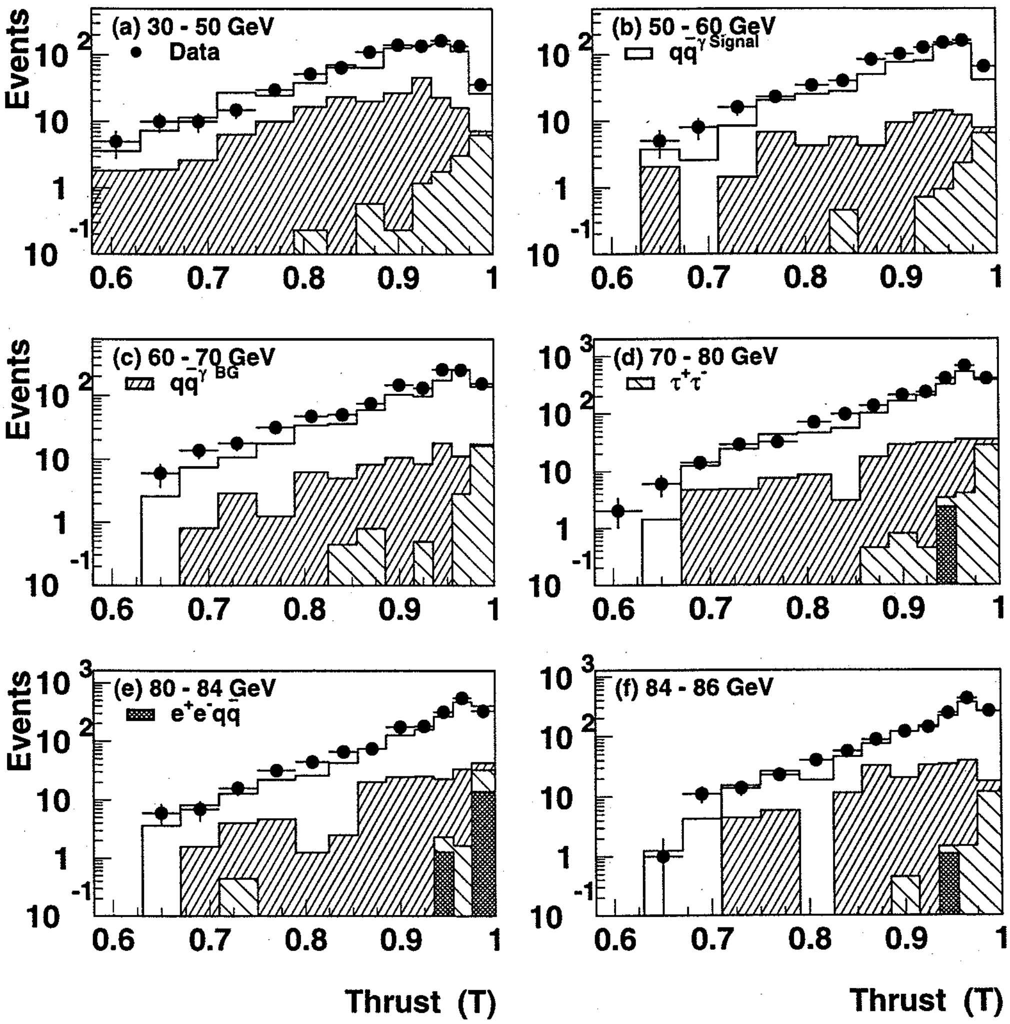

Figure 6.10: Measured thrust distributions at different reduced CM energies (a) 30–50 GeV, (b) 50–60 GeV, (c) 60–70 GeV, (d) 70–80 GeV, (e) 80–84 GeV, (f) 84–86 GeV. The solid lines correspond to the overall expectations from theory. The shaded areas refer to different backgrounds and the clear area refers to signal predicted by JETSET.

Figure 6.11 shows the corrected distributions for total jet broadening (B_T) at the six energy ranges. These distributions are compared with predictions from ARIADNE [50] 4.06, HERWIG 5.8 and JETSET 7.4 PS. Events are generated using a parameter set tuned with the L3 data at the Z peak [46]. The initial and final state radiation has been switched off. As can be seen in the figure, the data are in good agreement with QCD model predictions. This is also the case for the other event shape variables.

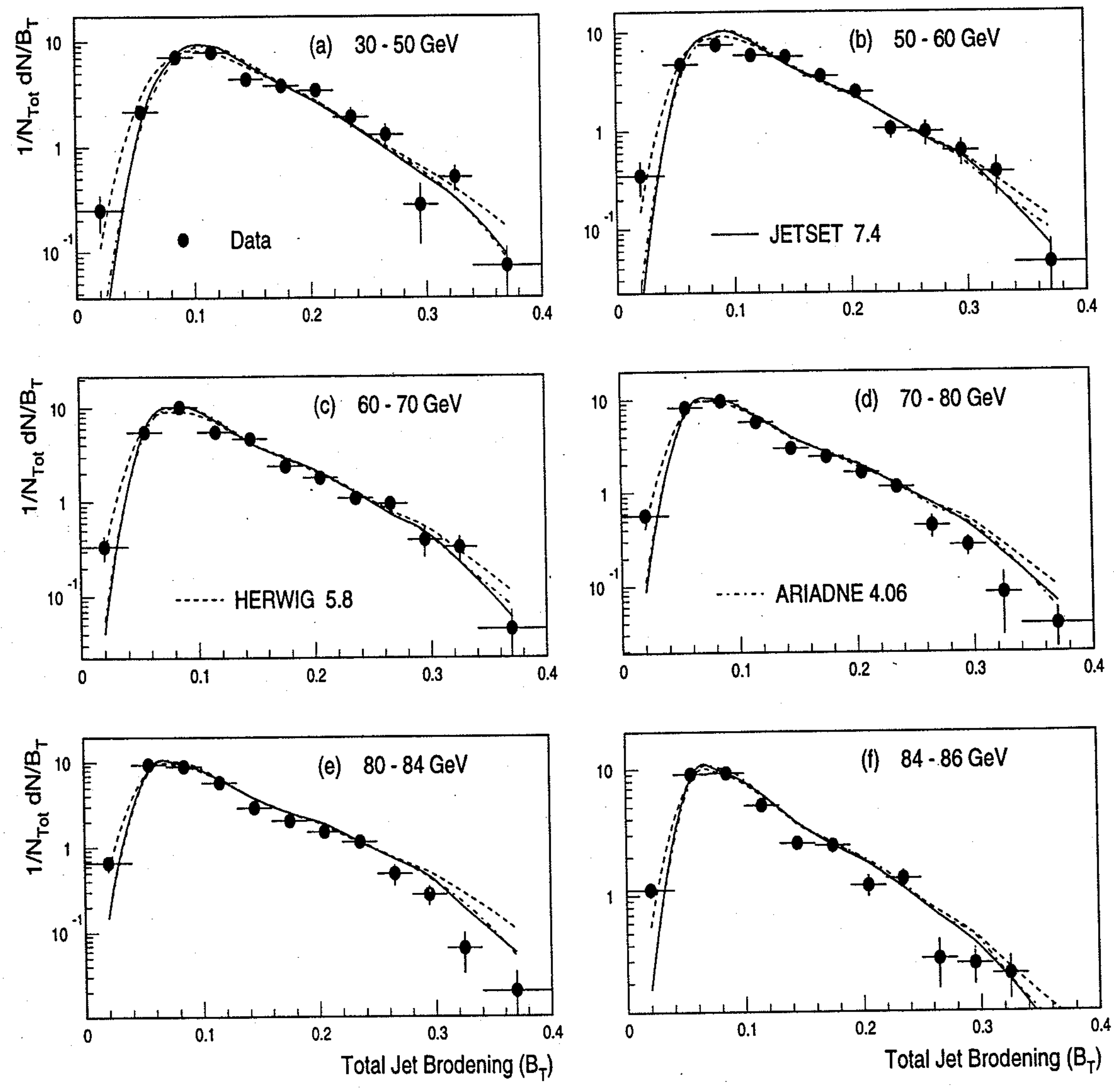

Figure 6.11: Corrected total jet broadening distributions at different reduced centre of mass energies (a) 30-50 GeV, (b) 50-60 GeV, (c) 60-70 GeV, (d) 70-80 GeV, (e) 80-84 GeV, (f) 84-86 GeV. The smooth lines correspond to the predictions of different QCD models.

6.5 Systematic Uncertainties

We have estimated the systematic errors on these measurements from a study of the variation of

1. *Background scale factors.*

   The scale factors are varied within $1\,\sigma$ to estimate the size of this effect.

2. *Selection cuts*

   The selection cuts are varied independently within certain ranges on both sides of the default values whereas possible.

   - The cut on shower shape discriminator has been varied between 0.5 and 0.15
   - Jet isolation angle has been varied between 15° and 25°.
   - Local isolation angle has been varied between 15° and 25°.
   - Energy in the local isolation cone varied between 500 MeV and 50 MeV
   - The jet isolation cut was removed and a local isolation cone of 25° for all the energy ranges was used.

3. *Correction methods.*

   The influence of this is determined by changing

   - the smoothening method for correction factors,
   - using JETSET and HERWIG fragmentation models for correcting the data
   - comparing the overall event sample with events where the isolated photon is restricted inside the central part of the detector ($|\cos\theta_\gamma| < 0.70$).

Figure 6.12 shows the spread observed for the heavy jet mass distribution at $\sqrt{s} = 60-70$ GeV when we use different smoothening methods for correcting data. This is the most significant source of experimental systematic error on physical quantities like mean value of an event shape variable.

6.6 Mean Values of Event Shape Variables

The measured mean values of thrust, scaled heavy jet mass, total and wide jet broadenings at the different centre of mass energies are summarised in tables 6.3 and 6.4 where the first error is statistical and the second one systematic. Systematic error is dominated by the error coming from variation in correction methods. We notice that different variables are affected in different ways by the correction method.

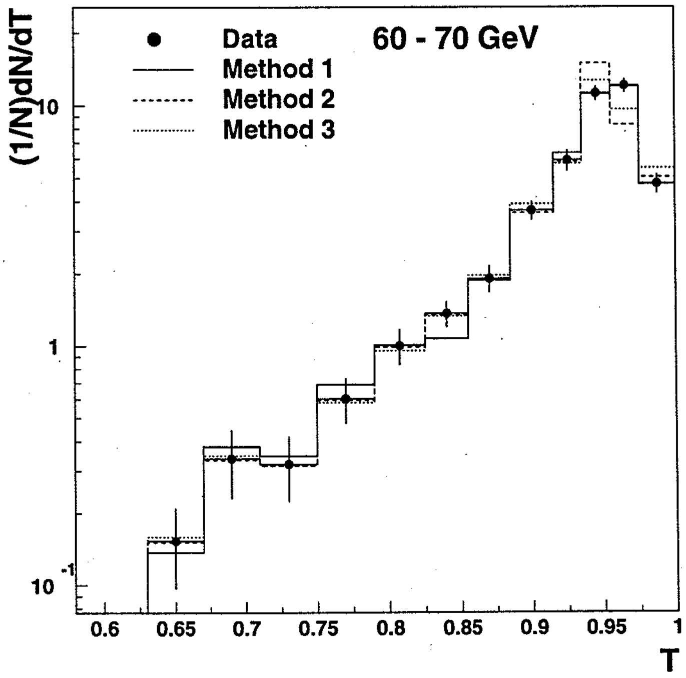

Figure 6.12: Typical spread in the distribution of heavy jet mass observed for energy range 60–70 GeV when we use different methods for smoothening the correction factors for correction of data.

$\sqrt{s}$ (GeV)	<T>	$<\rho>$
30–50	0.906±0.003±0.004	0.065±0.002±0.002
50–60	0.917±0.002±0.003	0.061±0.002±0.003
60–70	0.922±0.002±0.003	0.059±0.001±0.002
70–80	0.928±0.001±0.003	0.051±0.001±0.002
80–84	0.929±0.002±0.004	0.051±0.001±0.002
84–86	0.932±0.002±0.005	0.050±0.001±0.003

Table 6.3: Mean values of thrust (T), scaled heavy jet mass (ρ) measured at $\sqrt{s} = 30 - 86$ GeV. The first error is statistical and the second is systematic.

$\sqrt{s}$(GeV)	$< B_T >$	$< B_W >$
30–50	0.139±0.002±0.002	0.088±0.002±0.004
50–60	0.127±0.002±0.002	0.083±0.002±0.004
60–70	0.120±0.002±0.003	0.081±0.002±0.004
70–80	0.113±0.001±0.002	0.075±0.001±0.005
80–84	0.112±0.002±0.004	0.075±0.001±0.005
84–86	0.109±0.002±0.005	0.073±0.002±0.006

Table 6.4: Mean values of total (B_T), and wide jet broadening (B_W), measured at $\sqrt{s}$ = 30 – 86 GeV. The first error is statistical and the second is systematic.

Chapter 7

Hadronic Events at 161 GeV

Study of hadronic events from e^+e^- interactions at higher energies together with events at the Z peak at LEP is ideal to test the energy dependence of the strong coupling constant and the mean values of global event shape variables (defined in Section 2.4). At $\sqrt{s}$ = 161 GeV, effects of hadronisation are relatively small. But, at this higher energy well above the Z resonance, the cross section of the process $e^+e^- \rightarrow$ *hadrons* is quite low and hard initial state radiation (ISR), which was strongly suppressed at the Z peak, starts dominating. The emitted photons decrease the effective centre of mass energy to m_Z, which is known as *return to Z*. The photons dominantly go down the beam pipe, but some of them may be seen well inside the detector.

7.1 Selection of Hadronic Events

The essential requirement for selection of hadronic events which are produced at $\sqrt{s}$ = 161 GeV is the separation of these events from events produced at lower centre of mass energies due to emission of hard initial state photons. In addition to contribution from irreducible initial state radiation, the selected data sample contains W^+W^- events, the production of which is kinematically allowed at a centre of mass energy of 161 GeV. The two photon background ($e^+e^- \rightarrow e^+e^- +$ *hadrons*) too becomes significant at this energy.

For this analysis, we use events collected by the L3 detector at $\sqrt{s}$ = 161 GeV from the high energy run of LEP in 1996, which corresponds to a total integrated luminosity of 11.05 pb^{-1}. The total integrated luminosity delivered by the LEP machine was 12.3 pb^{-1} which gives a data acquisition efficiency of around 90% signifying a quite satisfactory operation of the L3 detector.

The final state particle multiplicity is high for hadronic events and a large fraction of the total energy is seen in the detector. One can make use of these two distinctive features to select a pure sample of hadronic events with very high efficiency. At the Z peak, the cross section of the process $e^+e^- \rightarrow$ *hadrons* is large compared to that of any other background processes and initial state radiation is strongly suppressed. Therefore, one obtains a sample of hadronic events with a purity of 99% at a selection efficiency of 98%. However, this is no longer true at $\sqrt{s}$ = 161 GeV. The cross section for hadron production at 161 GeV is small, as shown in table 7.1. This includes emission of hard initial state photon which brings the centre of mass energy for hadron production around Z peak. As a result, less than one-third of the hadronic events are produced at centre of mass energies around 161 GeV. The two photon and W^+W^- pair production processes become significant sources of background at this energy. Cross sections for all the relevant processes at $\sqrt{s}$ = 161 GeV are listed in table 7.1 which are used for normalisation of Monte Carlo samples.

Process	$q\bar{q}\gamma$	$\tau^+\tau^-(\gamma)$	e^+e^- + hadrons	Ze^+e^-	ZZ	W^+W^-
Cross section (pb)	146.0	12.1	8814.8	2.5	0.4	3.2

Table 7.1: Cross sections of various processes at $\sqrt{s} = 161$ GeV in e^+e^- interactions.

The selection of hadronic events is based on the energy measured in the electromagnetic and hadron calorimeters. The clusters in the calorimeters with a minimum energy of 100 MeV are used for the energy measurement. We measure the total visible energy (E_{vis}) and the energy imbalances along ($E_{\parallel}$) and transverse ($E_{\perp}$) to the beam direction. A hadronic event should satisfy the following conditions

- $N_{cluster} > 12$
- $E_{vis}/\sqrt{s} > 0.6$
- $E_{\perp}/E_{vis} < 0.4$
- $N_{track} > 1$

We require at least one well reconstructed charged track to remove cosmic ray background. About 1300 events survived the above selection cuts. We accept 96% of the hadronic events after applying these cuts to fully simulated hadronic sample. Hadronic Monte Carlo events are generated using the parton shower programme PYTHIA 5.7 [47] and passed through the L3 detector simulation program SIGEL3. The dominant sources of background come from the process $e^+e^- \rightarrow W^+W^-$ and from two photon collisions as discussed earlier. Background contributions from $e^+e^- \rightarrow \tau^+\tau^-$, $ZZ \rightarrow f\bar{f}f\bar{f}$ and $Ze^+e^- \rightarrow e^+e^-f\bar{f}$ processes are not significant.

The visible energy normalised to the centre of mass energy is shown in figure 7.1 for the events selected by all the above mentioned cuts except the one on the visible energy itself. The visible energy distribution represents a double peak structure. One of the two

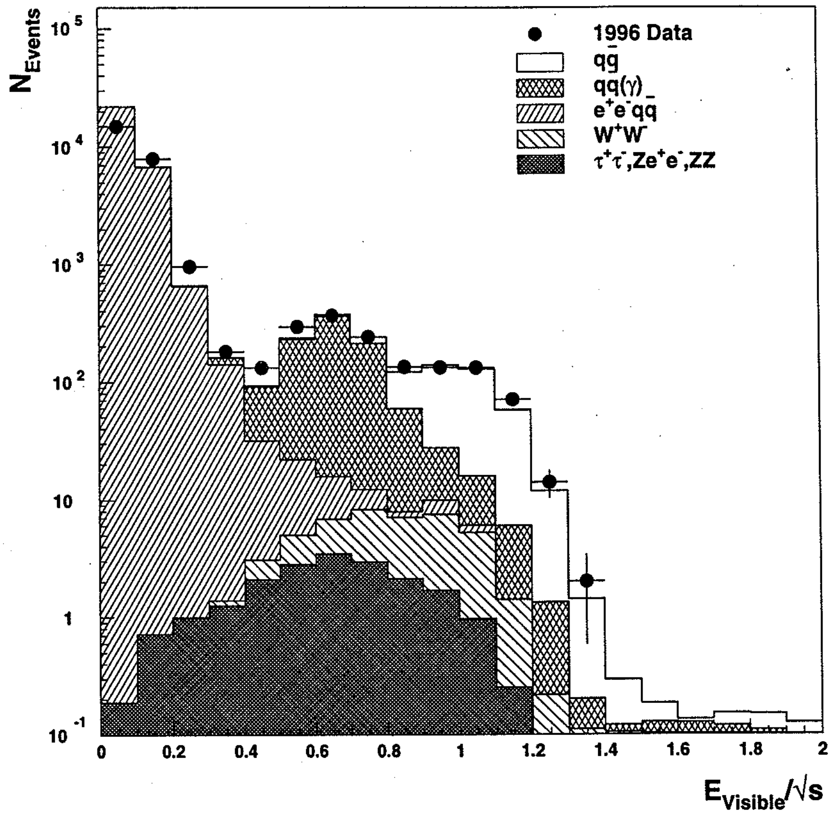

Figure 7.1: Visible energy normalised to centre of mass energy after applying all the hadron selection cuts except the cut on visible energy itself.

peaks corresponds to perfectly balanced events at $E_{vis}/\sqrt{s} = 1$ while the other corresponds to hadronic Z decays with hard photons in the initial state escaping into the beam pipe ($E_{vis}/\sqrt{s} \approx 0.5$).

At this stage, the fraction of events with hard initial state radiation in our sample is estimated from Monte Carlo to be about 67%. If we look at the energy distribution of the initial state photons at the particle level we see a huge peak at 54 GeV as shown in figure 7.2. As seen from the polar angular distribution of the photons shown in figure 7.3 most of the photons go along the beam pipe and hence remain undetected. A fraction, however, enters the detector volume. The following two conditions are applied to obtain a sample of true hadronic events produced at $\sqrt{s} = 161$ GeV,

(a) $(E_{vis}/\sqrt{s}) > 1.5\,(\mid E_{\parallel} \mid /E_{vis}) + 0.5$

(b) energy of the most energetic γ seen in the detector, $E_{\gamma} < 30$ GeV.

The first cut uses the correlation between $E_{vis}/\sqrt{s}$ and $\mid E_{\parallel} \mid /E_{vis}$, which is shown in

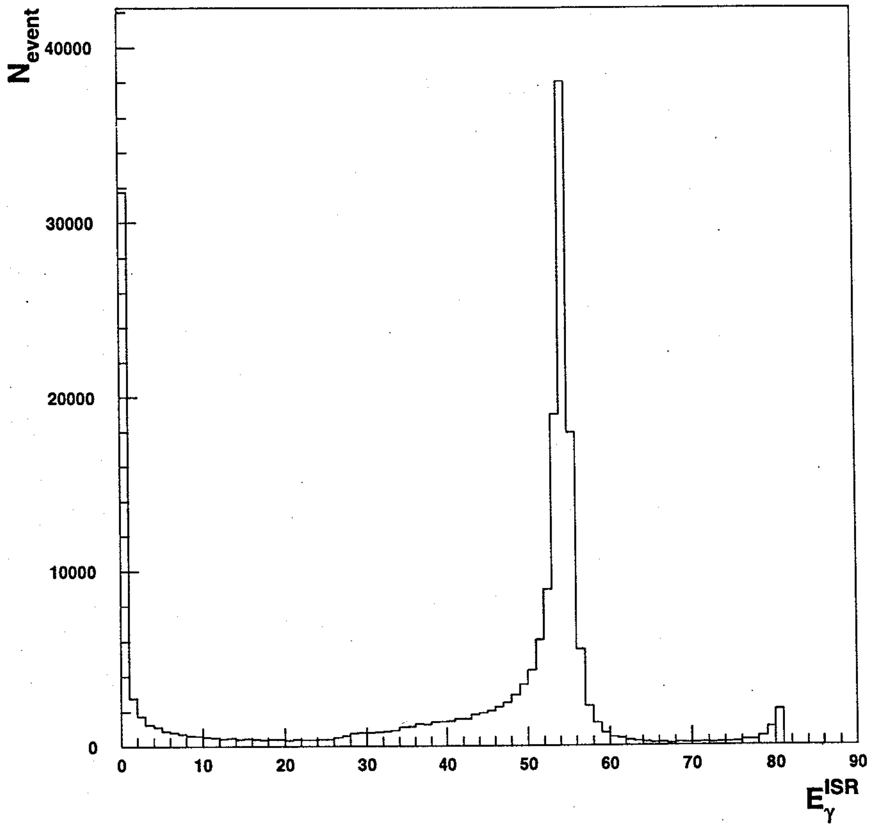

Figure 7.2: Energy distribution of the initial state photon at the particle level. The peak observed at 54 GeV corresponds to a return of the centre of mass energy for hadron production to the Z peak.

figure 7.4. It discriminates the well balanced events from unbalanced ones with an initial state photon which is lost in the beam pipe. Now, the well balanced events could contain initial state radiation where the photon is seen in the detector. These are removed by the second cut when a cluster compatible with a high energy photon of more than 30 GeV is found in the BGO calorimeter. Figure 7.5 shows the energy distribution of the most energetic photon in the BGO, where we observe a peak near 54 GeV corresponding to the emission of the hard initial state photon.

The final data sample used for this analysis contains 450 hadronic events. After all the cuts, the contamination from hard initial state radiation ($E_\gamma > 30$ GeV) amounts to about 10% of the sample. This contamination affects the mean effective centre of mass energy of the hadronic system which is lowered to about 154 GeV. The effect of initial state radiation

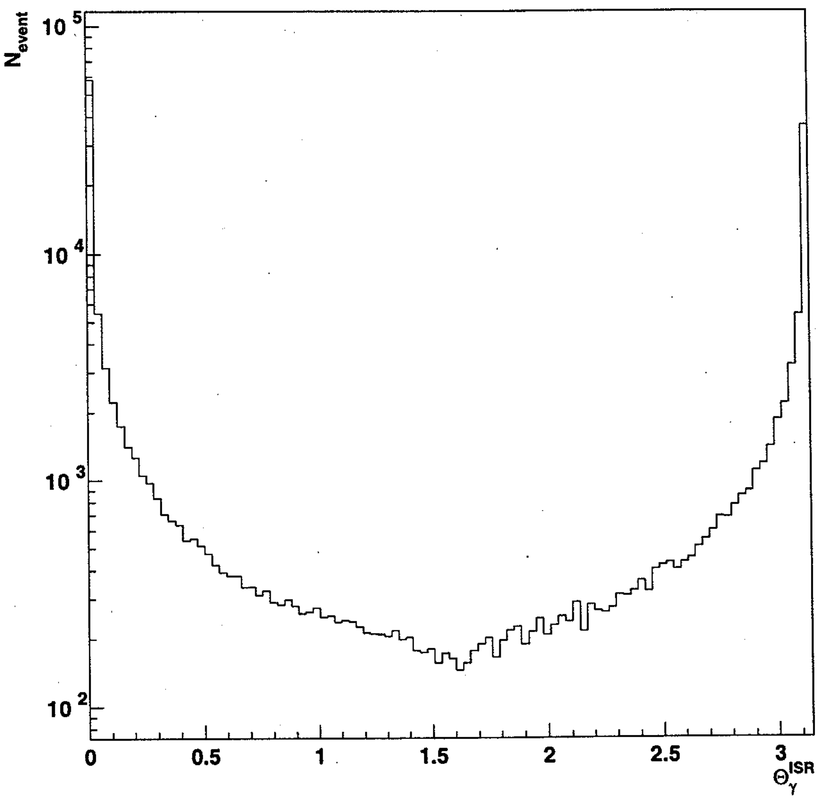

Figure 7.3: Distribution of polar angle of the initial state photon at the particle level. It is evident that the photons are dominantly produced at very low angles.

is accounted for using the PYTHIA Monte Carlo event generator. Applying the same set of cuts to simulated $e^+e^- \to W^+W^-$ events produced by KORALW generator [63], we estimate about 4% background contamination due to this process. A study of two photon Monte Carlo events generated by the PYTHIA generator [64] gives a background contribution of 3% to the selected sample. Table 7.2 summarises the background content of the event sample. At $\sqrt{s}$ = 161 GeV, Zee and ZZ events amount to 1% of the selected sample while the contribution of τ pair events is negligible.

7.2 Event Shape Variables

The jet structure of hadronic events can be analysed using global event shape variables. Observables like thrust, heavy jet mass, total and wide jet broadening studied in this analysis have been defined and described in detail in Chapter 2. Improved QCD calculations exist for these observables [65–67]. The other variables we study are jet multiplicity

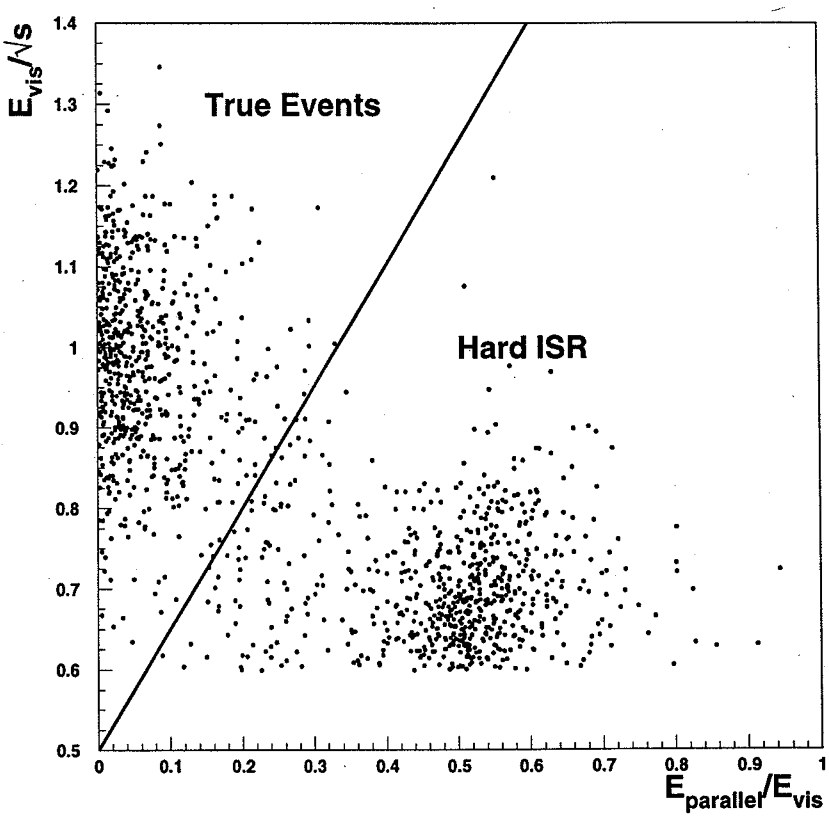

Figure 7.4: Visible energy normalised to centre of mass energy as a function of longitudinal energy imbalance scaled by the visible energy. The well balanced events corresponding to the high energy events are clearly separated from the events with hard unobserved initial state photon.

and charge multiplicity which we describe below,

(i) *Jet Multiplicity*:

Jets are reconstructed using JADE [21] and DURHAM [22] algorithms as discussed in Section 2.4. In this case to define the closeness variable we replace the centre of mass energy by the total visible energy. The jet fraction f_i is the fraction of all hadronic events containing i-jets

$$f_i = \frac{\sigma_{i-jets}}{\sigma_{tot}} .$$

f_i is a function of the jet resolution parameter y_{cut}.

(ii) *Charge Multiplicity*:

We define charge multiplicity, n_{ch}, as the number of charged particles in an event.

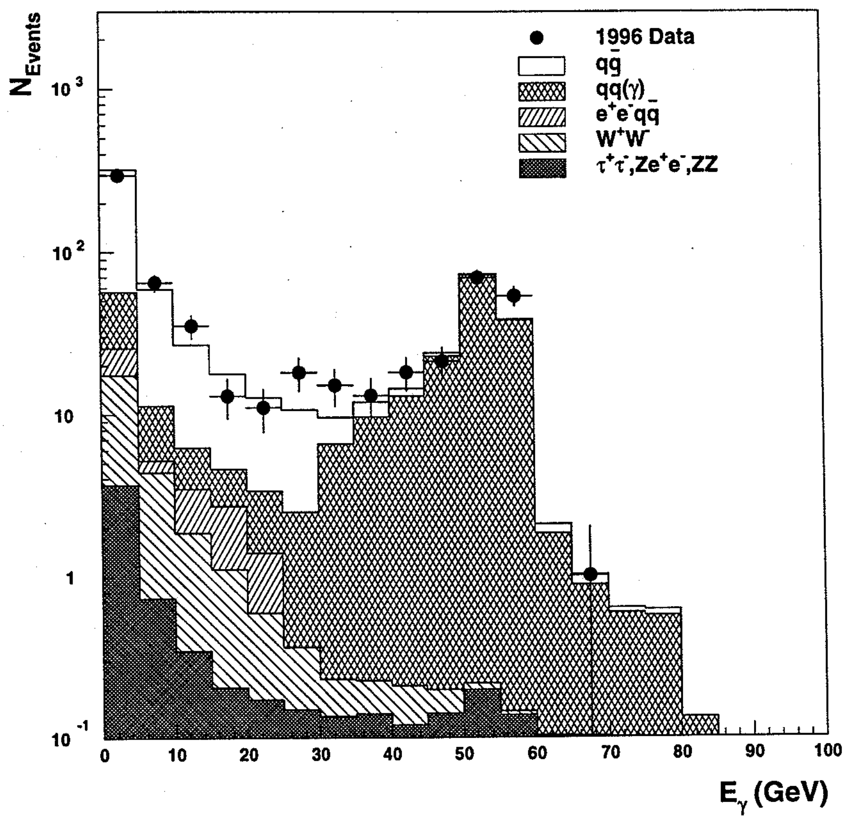

Figure 7.5: Energy distribution of the most energetic photon seen in the BGO calorimeter where all the above mentioned selection cuts except the one on the energy of the most energetic photon itself are applied.

The charge multiplicity distribution is obtained from reconstructed tracks while the other event shape distributions are obtained from reconstructed calorimetric clusters which are considered massless. For Monte Carlo events, the global event shape variables are calculated before (particle level) and after (detector level) detector simulation. The calculation before the detector simulation takes into account all stable charged and neutral particles. The measured distributions at detector level differ from the ones at particle level because of detector effects: limited acceptance and finite resolution.

The measured distributions for thrust (T), heavy jet mass (ρ), total (B_T) and wide (B_W) jet broadening at $\sqrt{s} = 161$ GeV are compared with the PYTHIA predictions at detector level as shown in figures 7.7 and 7.8. Data and Monte Carlo are in agreement. The background contributions from various sources are shown as well. All the Monte Carlo distributions are normalised to the total integrated luminosity.

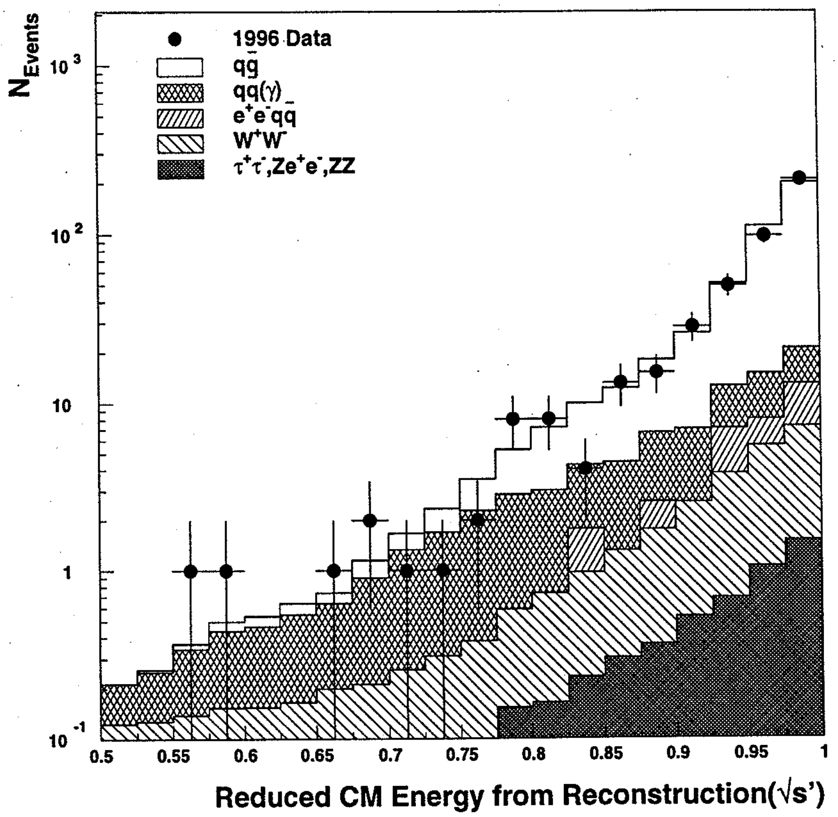

Figure 7.6: Reduced centre of mass energy reconstructed from the visible energy in the detector using kinematical constraint.

We subtract the shape of the background using Monte Carlo predictions from the data sample. The background corrected distributions are then corrected for detector resolution and finite acceptance on a bin-by-bin basis comparing the detector level result with the particle level result using Monte Carlo event sample. In the case of charged particle multiplicity the detector corrections are obtained using an unfolding matrix. We correct for initial and final state photon radiation bin-by-bin using Monte Carlo distributions at particle level with and without initial and final state radiation. Figure 7.11 show the detector resolution effect and the overall detector correction factors for total jet broadening.

The unfolding procedure is sufficiently accurate considering the limited statistics of the data sample. We correct the charge multiplicity distribution assuming all weakly decaying light particles (K_s^0, Λ, etc. with mean lifetime larger than 3.3×10^{-10} s) to be stable.

Figures 7.9 and 7.10 show the distributions for corrected thrust, scaled heavy jet mass, total and wide jet broadening. The data are compared with JETSET 7.4 [48], HERWIG 5.8 [51], ARIADNE 4.06 [50] and COJETS 6.23 [53] QCD models at particle level without

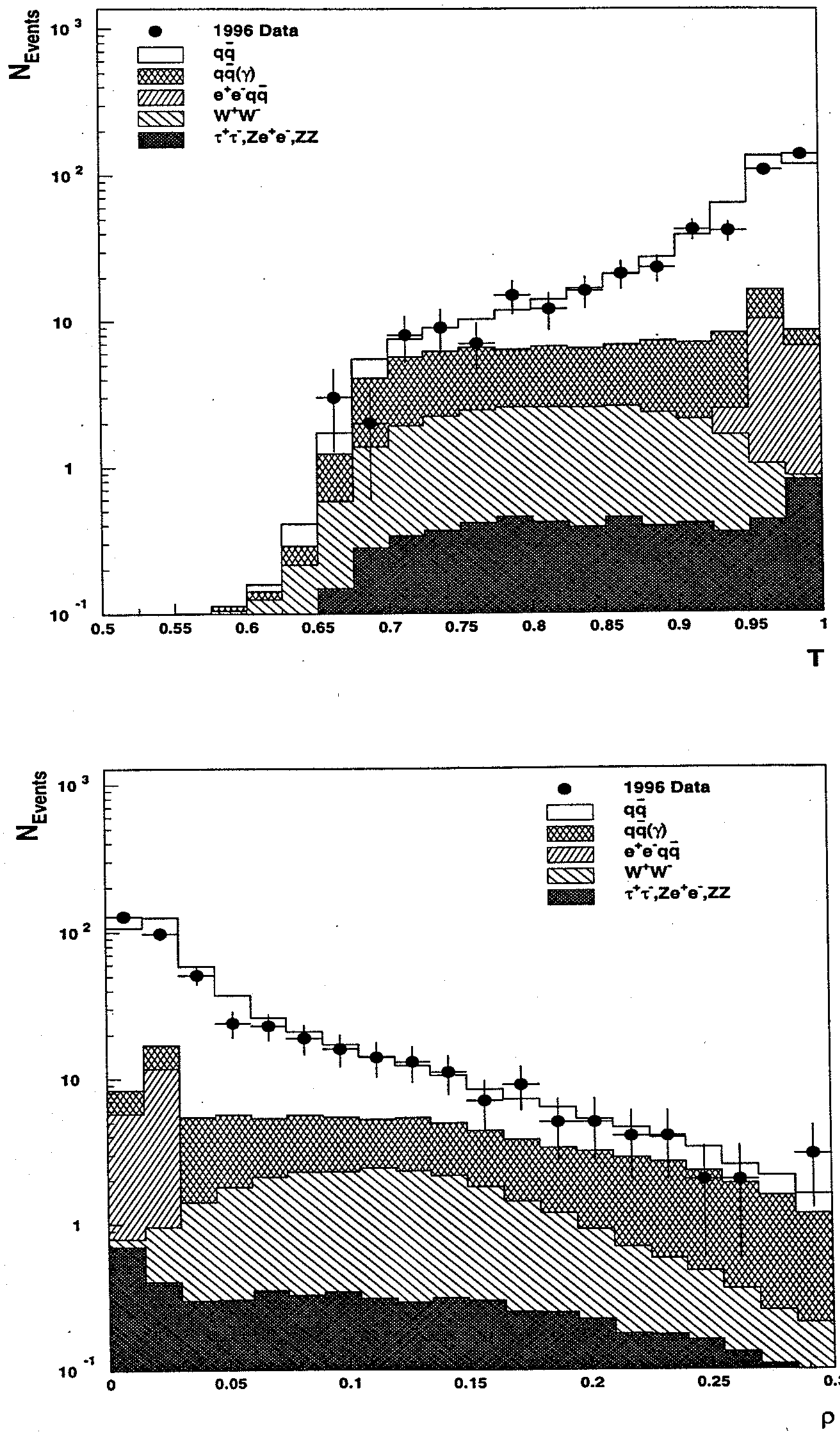

Figure 7.7: Measured distributions for thrust (T) and heavy jet mass (ρ), compared with the QCD predictions as described by PYTHIA. The background contributions from different sources are shown. All the Monte Carlo distributions are normalised using the total integrated luminosity. The experimental error shown is statistical.

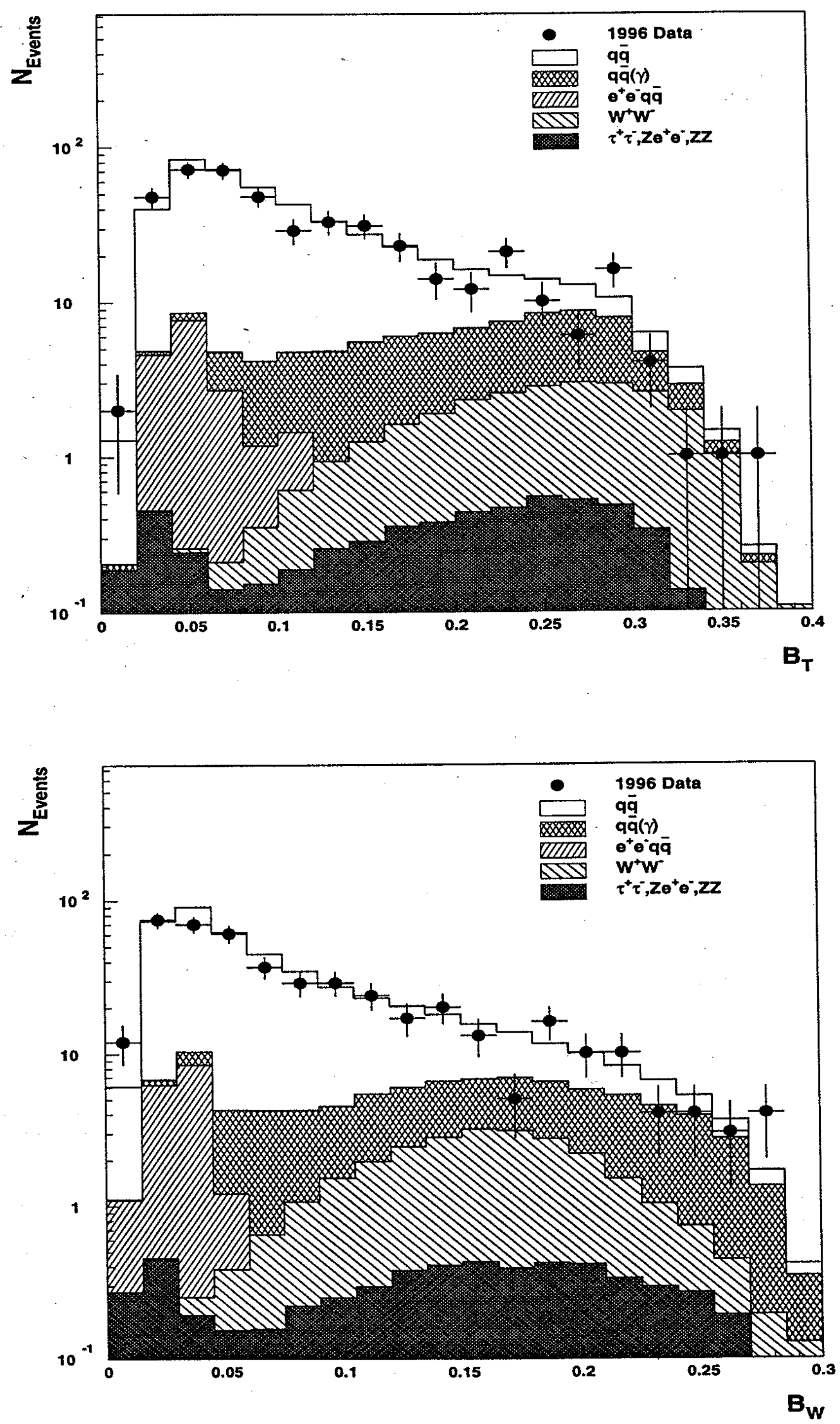

Figure 7.8: Measured distributions of total (B_T) and wide (B_W) jet broadening, compared with the QCD predictions as described by PYTHIA. The background contributions from different sources are shown. All the Monte Carlo distributions are normalised using the total integrated luminosity. The experimental error shown is statistical.

Process	Expected number of events	Fraction (%)
ISR $\leq$ 30 GeV	43.6	10
$e^+e^- \rightarrow W^+W^- \rightarrow 4f$	21.1	4
$e^+e^- \rightarrow e^+e^- +$ hadrons	15.6	3
$e^+e^- \rightarrow ZZ \rightarrow f\bar{f}f\bar{f}$	2.8	0.7
$e^+e^- \rightarrow Ze^+e^- \rightarrow e^+e^-f\bar{f}$	1.8	0.3
$e^+e^- \rightarrow \tau^+\tau^-$	1.8	0.3

Table 7.2: Background content of the selected event sample at $\sqrt{s} = 161$ GeV

initial and final state radiation. All the models agree with the measurements for the four observables T, ρ, B_T and B_W.

7.3 Energy Dependences of the Mean Values

The mean values of thrust and charged particle multiplicity are shown in figure 7.12 together with measurements at the Z resonance [68, 69] as well as those at low energy e^+e^- machines [70]. Also shown are the energy dependences of these quantities as predicted by JETSET 7.4 PS [48], HERWIG 5.8, ARIADNE 4.06, COJETS 6.23 [53] and JETSET 7.4 ME Monte Carlo models with the same parameter values over the full energy range [69]. One notices that QCD models except the JETSET 7.4 ME agree for all the distributions above 90 GeV. They are also in good agreement with the present measurement at 161 GeV. The JETSET 7.4 ME model fails to describe the energy dependence of $\langle n_{ch} \rangle$ over a wide energy range. This is understood as a consequence of a low parton multiplicity before fragmentation compared to the other models. The mean values of all the event shape variables at $\sqrt{s} = 161$ GeV studied in this analysis are listed in table 7.3.

7.4 Systematic Uncertainties

The systematic errors on event shape variables are mainly due to uncertainties in detector calibration, inhomogeneities in detector response and uncertainties in the background estimates.

The effect of detector calibration is studied by changing the definition of reconstructed objects used in the detector to build the observables. Instead of using only calorimetric clusters the analysis is repeated with a non linear combination of energies of charged tracks and calorimetric clusters to get the four-momenta of the objects used.

The uncertainty from possible inhomogeneities in detector response over the full acceptance is estimated by repeating the analysis only for the events where the event thrust points inside the central part of the detector where the resolution is better ($|\cos\theta_{\mathrm{Thrust}}| <$

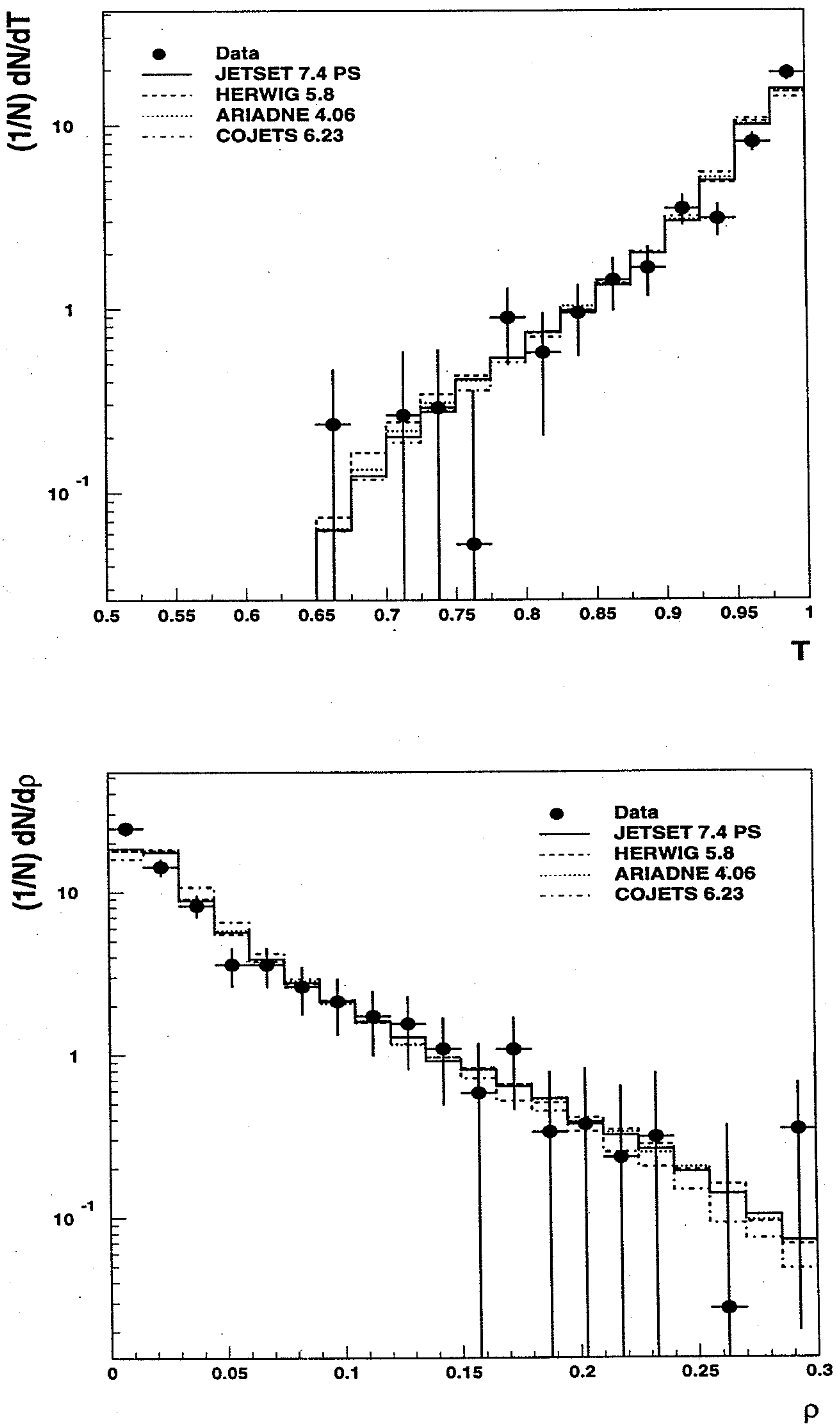

Figure 7.9: Distribution of thrust (T) and scaled heavy jet mass (ρ), after correction at $\sqrt{s} = 161$ GeV in comparison with QCD model predictions. The experimental errors are only statistical.

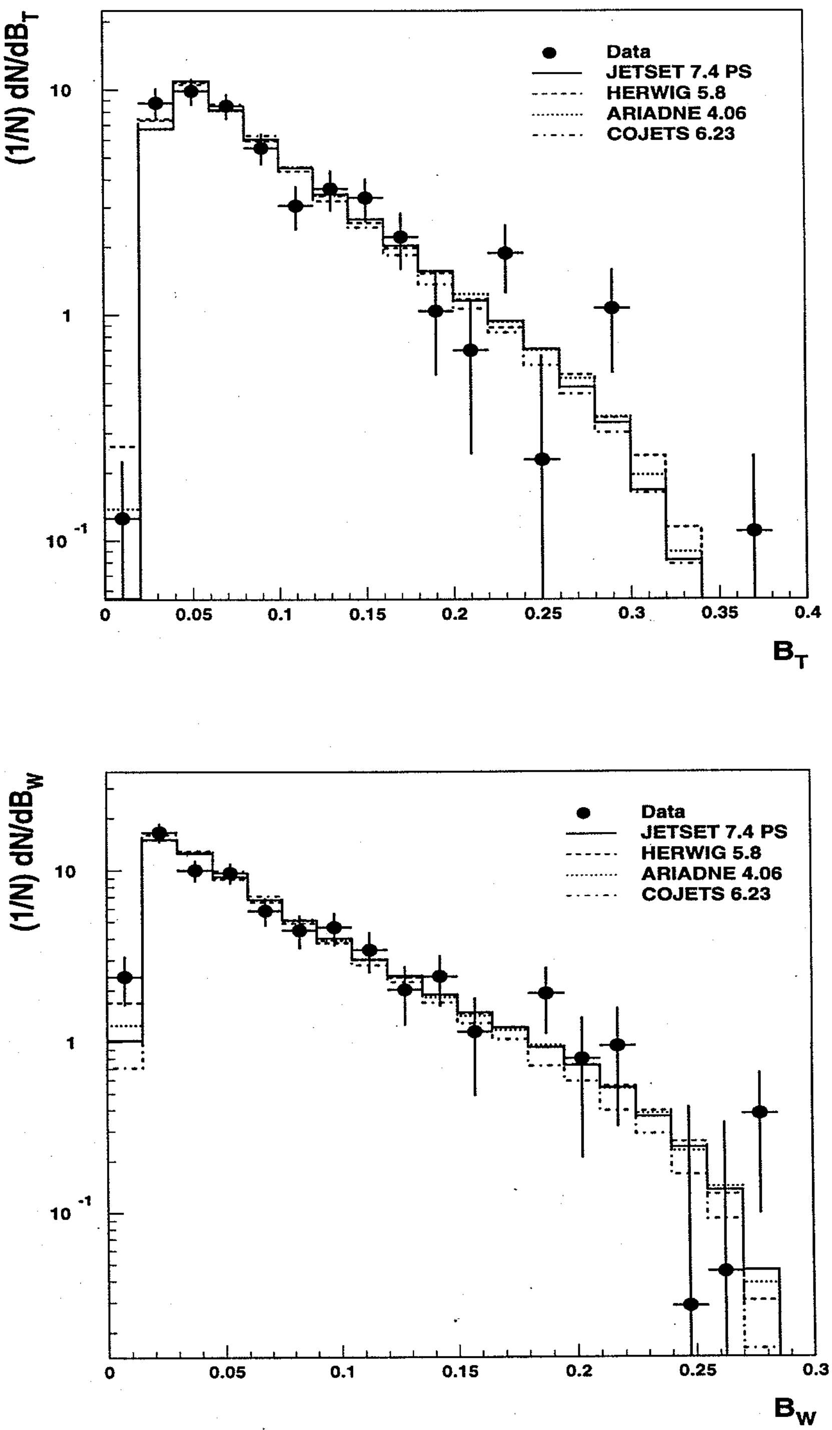

Figure 7.10: Distribution of total (B_T) wide (B_W) jet broadening, after correction at $\sqrt{s}$ = 161 GeV in comparison with QCD model predictions. The experimental errors are only statistical.

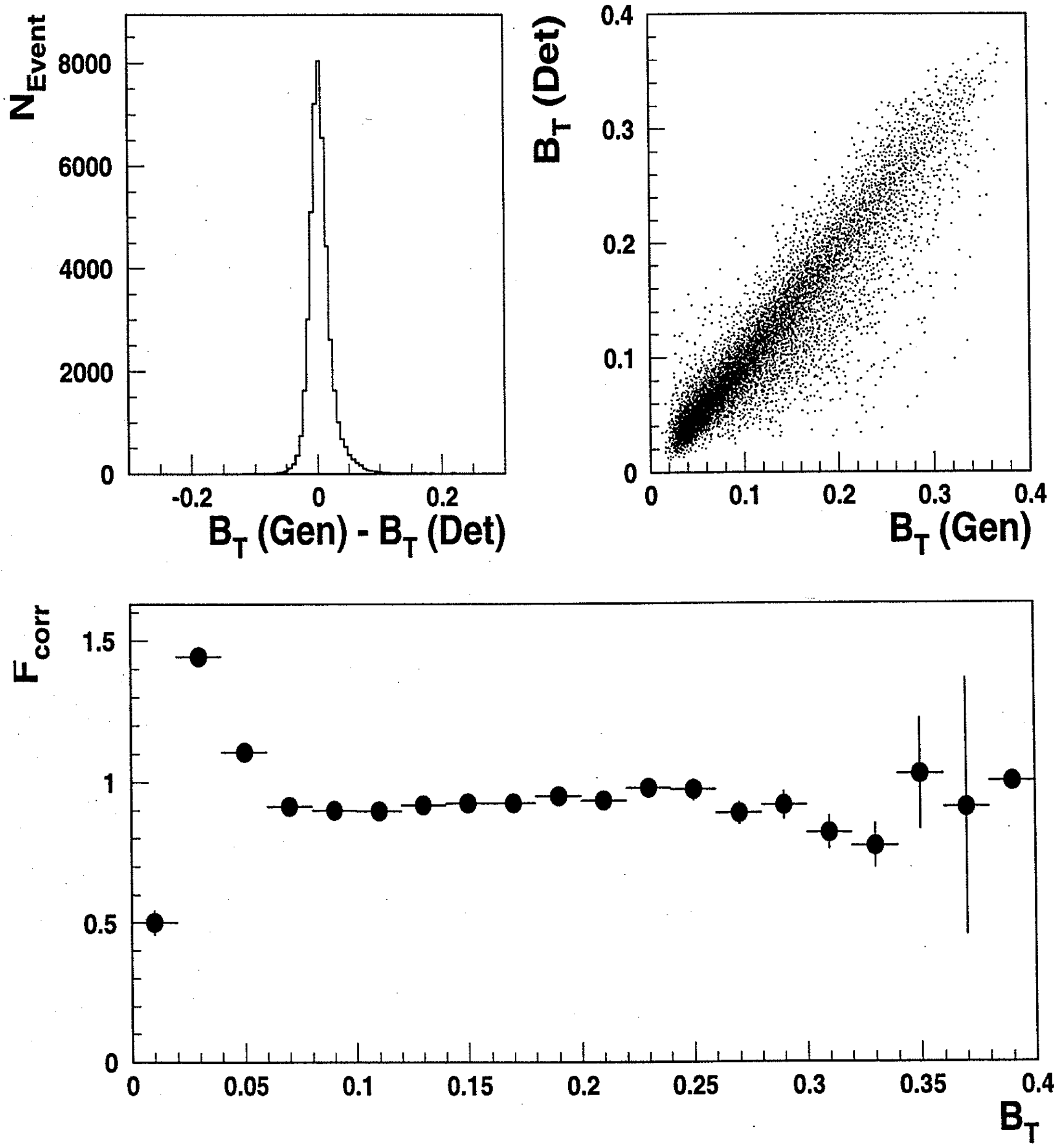

Figure 7.11: Detector resolution effect and the correction factor which accounts for both detector resolution and acceptance for total jet broadening. The data has been corrected on a bin-by-bin basis using detector simulated JETSET Monte Carlo events.

	$\sqrt{s} = 161$ GeV
$\langle T \rangle$	$0.946 \pm 0.003 \pm 0.001$
$\langle \rho_H \rangle$	$0.044 \pm 0.003 \pm 0.002$
$\langle B_T \rangle$	$0.094 \pm 0.003 \pm 0.001$
$\langle B_W \rangle$	$0.068 \pm 0.003 \pm 0.002$
$\langle y_{cut}^{JADE} \rangle$	$0.043 \pm 0.003 \pm 0.002$
$\langle y_{cut}^{DURHAM} \rangle$	$0.025 \pm 0.003 \pm 0.002$
$\langle S \rangle$	$0.070 \pm 0.005 \pm 0.003$
$\langle A \rangle$	$0.008 \pm 0.001 \pm 0.001$
$\langle C \rangle$	$0.207 \pm 0.010 \pm 0.010$
$\langle D \rangle$	$0.045 \pm 0.004 \pm 0.003$
$\langle T_{Major} \rangle$	$0.159 \pm 0.006 \pm 0.003$
$\langle T_{Minor} \rangle$	$0.069 \pm 0.002 \pm 0.003$
$\langle O \rangle$	$0.086 \pm 0.005 \pm 0.004$
$\langle T_{Minor}^{NS} \rangle$	$0.045 \pm 0.001 \pm 0.002$
$\langle H_2 \rangle$	$0.786 \pm 0.010 \pm 0.003$
$\langle H_3 \rangle$	$0.058 \pm 0.005 \pm 0.002$
$\langle H_4 \rangle$	$0.659 \pm 0.012 \pm 0.010$
$\langle \rho_L \rangle$	$0.012 \pm 0.001 \pm 0.001$
$\langle n_{ch} \rangle$	$25.59 \pm 0.4 \pm 0.4$

Table 7.3: Mean values of thrust (T), scaled heavy jet mass (ρ), total jet broadening (B_T), wide jet broadening (B_W), 3-jet resolution parameters (y_{cut}^{JADE} and y_{cut}^{DURHAM}), sphericity (S), aplanarity (A), C and D parameters, major (T_{Major}), minor (T_{Minor}), oblateness (O), minor narrow side, (T_{Minor}^{NS}), second, third and fourth Fox-Wolfram moments (H_2, H_3, H_4), light jet mass (ρ_L) and charge multiplicity (n_{ch}), measured at $\sqrt{s} = 161$ GeV. The first error is due to statistics and the second due to systematic effects.

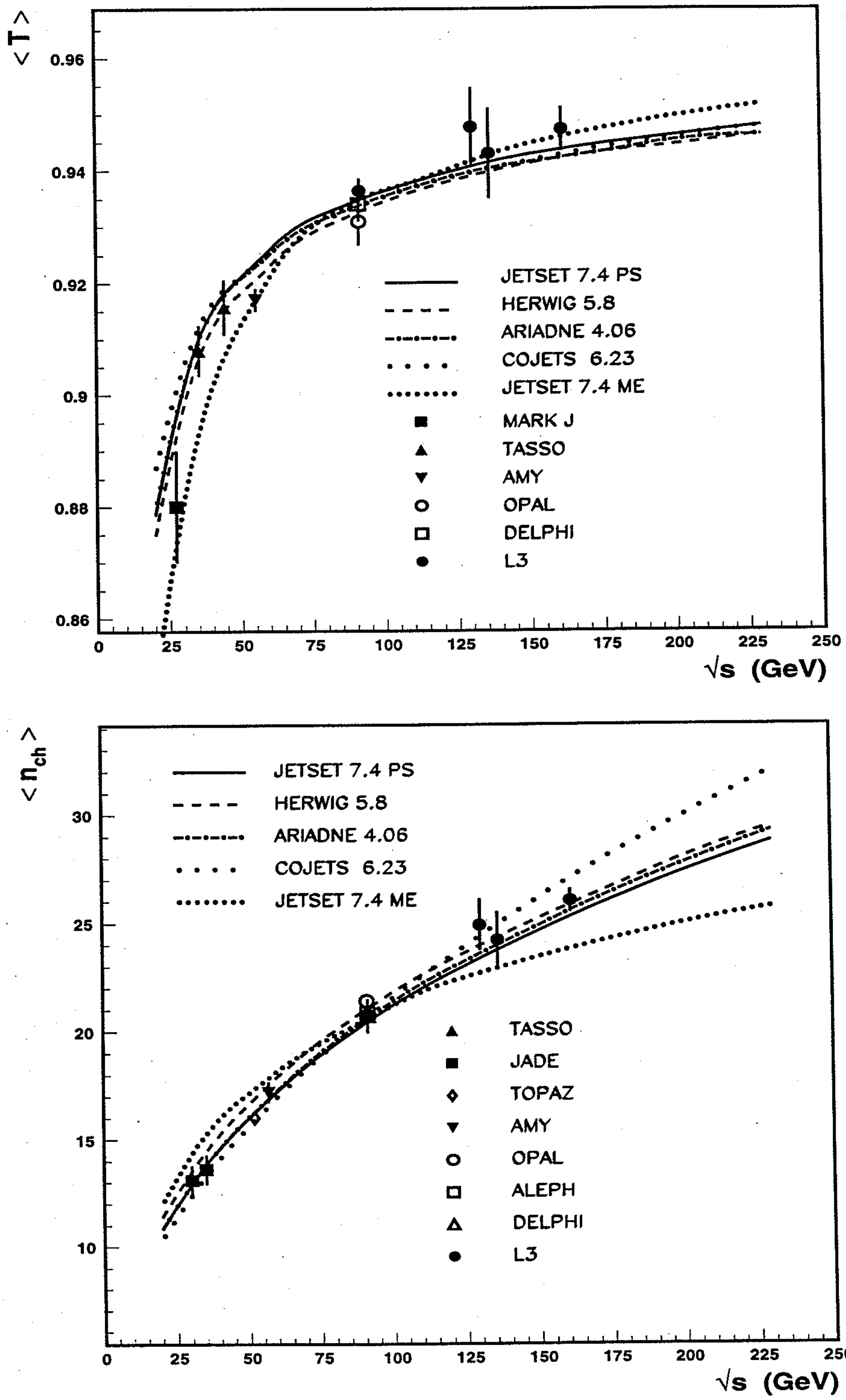

Figure 7.12: Distribution of mean thrust ($\langle$ T $\rangle$) and charged particle multiplicity ($\langle n_{ch} \rangle$), as functions of the centre of mass energy.

0.7).

The uncertainty on the background composition of the selected event sample has been estimated by repeating the analysis with:

- an alternative selection to reject the hard initial state photon event. The selection is then based on a cut on the effective centre of mass reconstructed from kinematical considerations. Figure 7.6 shows the distribution of the reconstructed reduced centre of mass energy for the selected sample. The cut corresponds to $\sqrt{s'} > 125$ GeV,
- a variation of the W^+W^- cross-section by $\pm$ 12% (1σ variation),
- a variation of two photon cross-section by $\pm$ 30% which corresponds to the maximum observed discrepancy when normalising the visible energy for 2 photon processes to the observed value.

The final systematic error is computed as the sum of all the above mentioned contributions in quadrature.

7.5 Jet Rates

The rate of events with 2, 3, 4 and 5 jets has been measured for JADE and DURHAM algorithms described in Section 2.4. The detector corrections and the background subtraction have been done in the same manner as for the other event shape variables for each value of the jet resolution parameter, y_{cut}. Figure 7.13 and 7.14 show the jet fraction measured with the two algorithms after background subtraction and correction for detector effects. The error shown includes both the statistical and systematic errors added in quadrature. The lines correspond to the prediction of JETSET 7.4 PS at 161 GeV. The measured jet rates are in agreement with the QCD model predictions at this centre of mass energy.

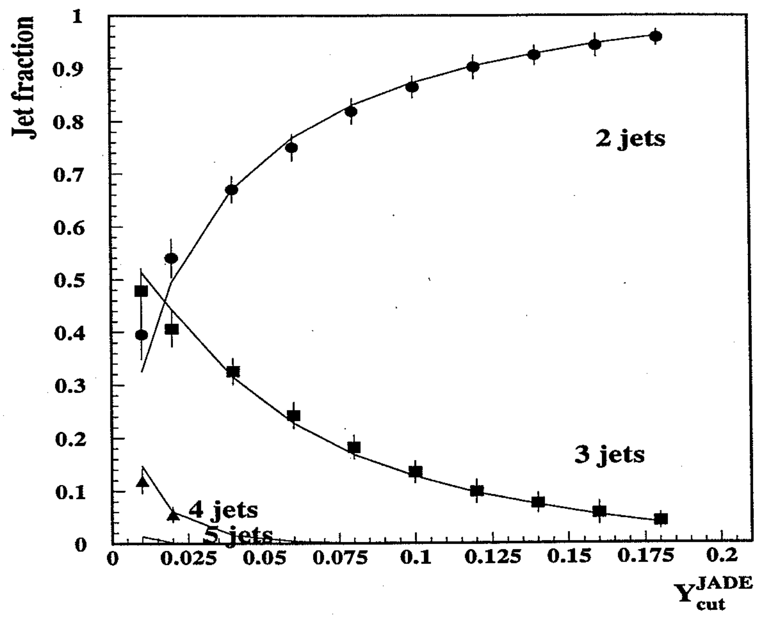

Figure 7.13: Jet rate as a function of y_{cut} for JADE algorithm at 161 GeV. The error bars include both statistical and systematic errors added in quadrature.

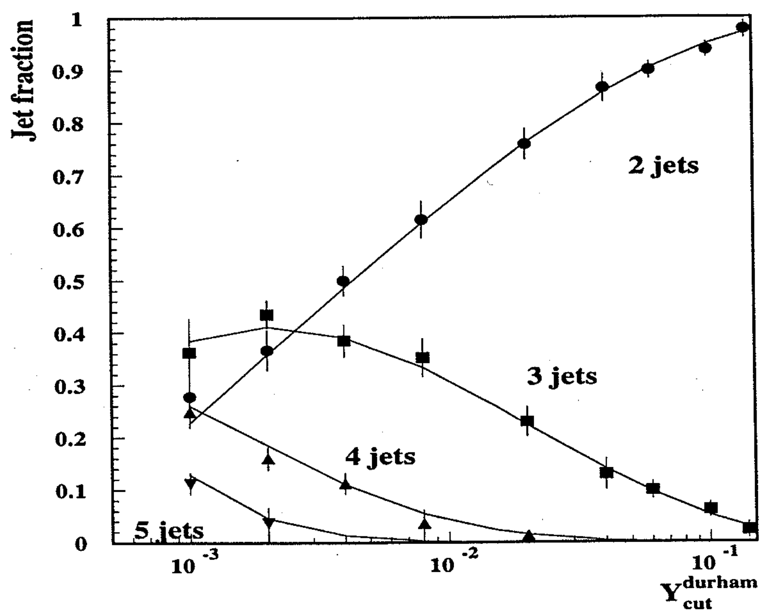

Figure 7.14: Jet rate as a function of y_{cut} for Durham algorithm at 161 GeV. The error bars include both statistical and systematic errors added in quadrature.

Chapter 8

The Strong Coupling Constant

The strong coupling constant (α_s) is a free parameter of perturbative Quantum Chromodynamics (QCD). It is important to measure α_s in as many different ways as possible, since agreement among the measurements serve as a test of consistency of the theory. A precise knowledge of the value of α_s and complete understanding of perturbative QCD are essential requirements of many electroweak tests at LEP. In particular, α_s constrains speculations about unification of the electroweak and strong interactions at very high energy regimes.

8.1 QCD Calculations

The standard method of determination of α_s involves comparison of experimental data with QCD calculations based on an order-by-order expansion in powers of α_s. For the process $e^+e^- \rightarrow$ *hadrons*, QCD matrix elements are known fully up to $\mathcal{O}({\alpha_s}^2)$. An improved calculation has been obtained by combining fixed order calculations with resummation of leading logarithm terms, which arise from soft and collinear gluon emission. This reduces the uncertainties related to the transition between perturbatively calculable parton level and hadron level, as well as those arising from the choice of the renormalisation scale, μ. It also extends the range of validity of the predictions into the region of high statistics, where the emitted gluons are very close in phase space to the original quarks.

8.1.1 Fixed $\mathcal{O}({\alpha_s}^2)$ Calculations

In fixed order calculations emission of at most two gluons is considered. So $\mathcal{O}({\alpha_s}^2)$ theory naturally cannot take into account the effect of multiple gluon emission. For variables, like thrust (T), heavy jet mass (ρ), total (B_T) and wide (B_W) jet broadening discussed in Section 2.4, this leads to a singular behaviour of the distributions in the kinematic regions where multi-gluon emission becomes dominant. This is a direct consequence of the collinear and infrared divergence of the gluon emission cross section. QCD predictions in fixed second order perturbation theory can describe the distribution of an infrared and collinear safe variable only in a limited kinematic region dominated by events with hard gluon emission, where corrections due to higher order terms arising from multiple soft gluon emission become negligible.

Fixed order calculations up to $\mathcal{O}(\alpha_s^2)$ exist for the above mentioned event shape variables. Cumulative cross section R(y) for an event shape variable y (y $\equiv$ 1$-$T, ρ, B_T or B_W) can be written as,

$$\begin{aligned} R(\alpha_s, y) &\equiv \int_0^y \frac{1}{\sigma}\frac{d\sigma}{dy} \\ &= \overline{\alpha}_s A(y) + \overline{\alpha}_s{}^2 \left[B(y) + 2\pi\beta_0 \ln(\mu^2/s) A(y)\right] \end{aligned}$$

where

$$\begin{aligned} \overline{\alpha}_s &= \frac{\alpha_s(\mu)}{2\pi} \\ \beta_0 &= \frac{33 - 2N_f}{12\pi} . \end{aligned}$$

Here μ is the scale and N_f is the number of light fermion flavours.

The coefficients A(y) and B(y) can be computed by integrating ERT matrix elements [71] up to $\mathcal{O}(\alpha_s^2)$ using the programme EVENT. Such QCD predictions (up to $\mathcal{O}(\alpha_s^2)$) describe the data well in the region corresponding to hard gluon emission, but fail in the two jet region (small y). For y $\approx$ 0

$$\begin{aligned} R(\alpha_s, y) &\sim \alpha_s{}^n \ln^{2n}\left(\frac{1}{y}\right) \\ &\equiv \left(\alpha_s L^2\right)^n , \end{aligned}$$

where L = ln (1/y) and n is the order of expansion. We note that the effective expansion parameter is not simply α_s, but $\alpha_s L^2$. Perturbative treatment makes sense for small ($\alpha_s L^2$); but at small y, the value of $\alpha_s L^2$ is not necessarily small. Therefore, these terms must be resummed to all orders in α_s in order to provide a satisfactory description.

8.1.2 Resummed Calculations

It is possible to isolate the singular terms in every order of the perturbation series and sum them up in the form of an exponential. These calculations have been carried out for the variables 1$-$T, ρ, B_T, B_W up to next-to-leading logarithm (NLLA) terms [65–67, 73]. On the other hand, in the fixed order calculations [71, 72], all the contributions (including the subleading terms) have been determined to second order.

Cumulative cross section $R(\alpha_s, y)$ for event shape variable y is given by,

$$\begin{aligned} R(\alpha_s, y) &\equiv \int_0^y \frac{1}{\sigma}\frac{d\sigma}{dy}dy \\ &= C(\alpha_s)\, e^{G(\alpha_s, L)} + D(\alpha_s, y)\,. \end{aligned}$$

Here $D(\alpha_s, y)$ is a remainder function which should vanish as $y \to 0$ and is given by

$$D(\alpha_s, y) = \sum_{n=1}^{\infty} D_n(y)\overline{\alpha}_s{}^n\,.$$

The functions C and G can be written as

$$\begin{aligned} C(\alpha_s) &= 1 + \sum_{n=1}^{\infty} C_n \overline{\alpha}_s{}^n \\ G(\alpha_s, L) &= \sum_{n=1}^{\infty}\sum_{m=1}^{n+1} G_{nm}\overline{\alpha}_s{}^n L^m \\ &\equiv L g_1(\overline{\alpha}_s L) + g_2(\overline{\alpha}_s L) + \overline{\alpha}_s g_3(\overline{\alpha}_s L) + \overline{\alpha}_s{}^2 g_4(\overline{\alpha}_s L) + \cdots\,. \end{aligned}$$

The functions $Lg_1(\overline{\alpha}_s L)$ and $g_2(\overline{\alpha}_s L)$ represent the sums of the leading and next-to-leading logarithms respectively, to all orders in $\overline{\alpha}_s$. The NLLA calculations give an approximate expression for R(y) in the form,

$$R_{NLLA}(y) = (1 + C_1\overline{\alpha}_s + C_2\overline{\alpha}_s{}^2)\, e^{[Lg_1(\overline{\alpha}_s L) + g_2(\overline{\alpha}_s L)]}\,.$$

The functions g_1 and g_2 are given by the NLLA calculations; the coefficients C_1 is known exactly from the $\mathcal{O}(\alpha_s)$ matrix element and C_2 is known for the four event shape variables under consideration, from numerical integration of the $\mathcal{O}(\alpha_s{}^2)$ matrix element.

The two approaches are summarised in table 8.1. The first two rows have been fully computed in the fixed order calculations and the first two columns are known to all orders. In order to describe data over a wide kinematic region, it is desirable to combine the two sets of calculations taking care of the common terms. This leads to a number of matching schemes which we discuss below.

8.1.3 Combining the Resummed and the Fixed Order Calculations

The next-to-leading-order calculations are expected to be most reliable in predicting the parton distributions in the two jet region. Unfortunately this region is subject to particularly large hadronisation effects, which introduce significant uncertainties when theoretical prediction is compared with data. One requires to construct an improved theoretical prediction by combining the second order and the leading, plus next-to-leading-logarithm

	LLA	NLLA	subleading			
$\mathcal{O}(\alpha_s)$	$\overline{\alpha}_s L^2$	$\overline{\alpha}_s L$	$\overline{\alpha}_s$	$\overline{\alpha}_s \mathcal{O}\left(\frac{1}{L}\right)$		
$\mathcal{O}(\alpha_s{}^2)$	$\overline{\alpha}_s{}^2 L^3$	$\overline{\alpha}_s{}^2 L^2$	$\overline{\alpha}_s{}^2 L$	$\overline{\alpha}_s{}^2$	$\overline{\alpha}_s{}^2 \mathcal{O}\left(\frac{1}{L}\right)$	
$\mathcal{O}(\alpha_s{}^3)$	$\overline{\alpha}_s{}^3 L^4$	$\overline{\alpha}_s{}^3 L^3$	$\overline{\alpha}_s{}^3 L^2$	$\overline{\alpha}_s{}^3 L$	$\overline{\alpha}_s{}^3$	$\overline{\alpha}_s{}^3 \mathcal{O}\left(\frac{1}{L}\right)$
$\vdots$	$\vdots$	$\vdots$	$\vdots$	$\vdots$	$\vdots$	$\vdots$

Table 8.1: Tabular representation of fixed order and the logarithmic expansions of theoretical predictions for event shape variables.

resummed calculations. The combination is exact to $\mathcal{O}(\alpha_s{}^2)$ over the whole phase space and in the vicinity of the 2-jet region ($y \to 0$) contains the dominant terms of all orders.

There is a certain freedom in combining the two sets of theoretical calculations which can be used to probe the sensitivity of measurement of α_s to the unknown higher order. The various matching schemes all contain the full $\mathcal{O}(\alpha_s{}^2)$ calculations, together with the resummation of leading and next-to-leading logarithms, but differ in higher orders.

The full $\mathcal{O}(\alpha_s{}^2)$ calculation yields an approximate expression for $R(y)$ of the form

$$R_{\mathcal{O}(\alpha_s{}^2)}(y) \quad = \quad 1 + A(y)\overline{\alpha}_s + B(y)\overline{\alpha}_s{}^2 \, .$$

The simplest matching scheme is to match the two calculations at a given value of y and use a suitable damping function so that the resummed calculations contribute to the two jet region and the fixed order calculations dominate in the multi-jet region. A more preferable approach would be to combine the two calculations and then subtract the common terms of the two calculations. This is done by taking logarithm of $R_{\mathcal{O}(\alpha_s{}^2)}(y)$ and expanding it as a power series, which yields,

$$\ln R_{\mathcal{O}(\alpha_s{}^2)}(y) \quad = \quad A(y)\overline{\alpha}_s + [B(y) - \frac{1}{2}A^2(y)]\overline{\alpha}_s{}^2 + \mathcal{O}(\alpha_s{}^3) \, .$$

In an analogous way, $R_{NLLA}(y)$ can be rewritten as

$$\ln R_{NLLA}(y) \quad = \quad L g_1(\overline{\alpha}_s L) + g_2(\overline{\alpha}_s L) + C_1\overline{\alpha}_s + [C_2 - \frac{1}{2}C_1^2]\overline{\alpha}_s{}^2 + \mathcal{O}(\alpha_s{}^3) \, .$$

Removing the terms up to $\mathcal{O}(\alpha_s{}^2)$ in the NLLA expression, one obtains

$$\begin{aligned} \ln R(y) = {} & L g_1(\overline{\alpha}_s L) + g_2(\overline{\alpha}_s L) - (G_{11}L + G_{12}L^2)\overline{\alpha}_s \\ & - (G_{22}L^2 + G_{23}L^3)\overline{\alpha}_s{}^2 + A(y)\overline{\alpha}_s + [B(y) - \frac{1}{2}A^2(y)]\overline{\alpha}_s{}^2 \, . \end{aligned} \tag{8.1}$$

This procedure is known as *ln(R) matching*. We can alternatively carry out the *R matching* by using $R(y)$ instead of $\ln(R)(y)$ which would yield,

$$
\begin{aligned}
R(y) = {} & (1 + C_1\overline{\alpha}_s + C_2\overline{\alpha}_s{}^2)e^{[Lg_1(\overline{\alpha}_s L)+g_2(\overline{\alpha}_s L)]} - (C_1 + G_{11}L + G_{12}L^2)\overline{\alpha}_s \\
& - [C_2 + G_{22}L^2 + G_{23}L^3 + (G_{11}L + G_{12}L^2)(C_1 + \frac{1}{2}(G_{11}L + G_{12}L^2))]\overline{\alpha}_s{}^2 \\
& + A(y)\overline{\alpha}_s + B(y)\overline{\alpha}_s{}^2 \, .
\end{aligned} \tag{8.2}
$$

We expect that the R-matching would be less reliable than the ln(R) matching, because the subleading term $G_{21}\overline{\alpha}_s L$, which does not vanish at $y \to 0$, is not exponentiated in equation (8.2), whereas it is exponentiated in equation (8.1) because it is implicitly included in the B(y) coefficient. This leads one to consider a modified form of equation (8.2) in which the $G_{21}\overline{\alpha}_s L$ term is included in the argument of the exponential, and subtracted after exponentiation. We refer to this as the *modified R-matching* scheme. The coefficient G_{21} is not analytically computed, but may be inferred approximately from numerical integration of the $\mathcal{O}(\alpha_s{}^2)$ matrix elements.

One has to take care of the additional constraint coming from kinematics. The cross sections should vanish beyond the kinematic limit

$$
\begin{aligned}
R(y = y_{max}) &= 1 \\
\frac{dR}{dy}(y = y_{max}) &= 0 \, .
\end{aligned}
$$

These constraints are strictly obeyed in fixed order calculations but they are not valid for the resummed expansion. The first constraint can be taken care of by replacing R(y) by $R(y) - R(y_{max})$ for the resummed calculations. Alternatively, one can replace L in the resummed term by

$$
L' = \ln(y^{-1} - y_{max}^{-1} + 1)
$$

in the *ln(R) matching* scheme to fulfil both of them. This possibility is referred to as *modified ln(R) matching.*

All the above four matching schemes may be applied to the event shape variables $1-T$, ρ, B_T and B_W.

The fixed order calculations together with resummed calculations can explain small y (high statistics) region. One gets a good fit at a reasonable renormalisation scale ($\mu \approx \sqrt{s}$). As more theoretical terms are known, uncertainty due to unknown higher order terms should reduce.

8.2 Hadronisation Correction

The theoretical calculations described above are given in the form of analytical functions for massless partons, $f^{pert}(y; s, \alpha_s(\mu), \mu)$. The calculations do not take into account the hadronisation of the partons. To compare the analytical calculations with the experimental distributions, the predictions have to be folded in by the effect of hadronisation and decays using Monte Carlo programmes. The hadronisation should start from partonic states corresponding as closely as possible to the analytic perturbative calculations. Since the NLLA QCD calculations are based on the leading logarithm approximation it is appropriate to use parton shower QCD Monte Carlo models which are based on essentially the same approximation to correct for hadronisation effect. We have used the parton shower programmes JETSET 7.4 PS, ARIADNE 4.06 and HERWIG 5.8 with string and cluster fragmentation. The fragmentation parameters are determined from a comparison of predicted and measured distributions for several event shape variables [46]. The important fragmentation parameters of all the QCD Monte Carlo generators used in the work and their values are listed in Section 4.1.1. All these generators describe our experimental measurements well. We fold in the perturbative calculations for a variable y with the probability $p^{non-pert}(y', y)$ of finding a value y after fragmentation and decays for a parton level value y':

$$f(y) = \int f^{pert}(y') \cdot p^{non-pert}(y', y)\, dy' .$$

The resulting differential cross section f(y) is compared to our measurements which is corrected for background, detector resolution and acceptance. The correction due to hadronisation and decays changes the perturbative prediction by less than 5–10% for the event shape variables over a wide kinematic range. The hadronisation correction is relatively large in the extreme two jet region.

The uncertainties in the probabilities $p^{non-pert}(y', y)$ and the measurement of the strong coupling constant, α_s are estimated in the following way:

- We change the fragmentation parameters in the JETSET 7.4 PS Monte Carlo model.

  We have independently varied the parameters which are related to parton showering and hadronisation, σ_Q = PARJ(21) = 0.41 ± 0.02 GeV and b=PARJ(42)=0.886 ± 0.06 (GeV^{-2}) by ±1 standard deviation about their optimised values. The effect of these changes is found to be modest.

- We compare the predictions of the different hadronisation models. We use HERWIG 5.8 programme which uses a cluster fragmentation model.

- We study the effect of Bose-Einstein correlation by switching this effect on in the JETSET 7.4 PS generator.

We found that the most dominant contribution to the hadronisation error comes from the Bose-Einstein correlation effect. We estimate the overall uncertainty as half of the maximum spread.

Figure 8.1 shows quantitatively the hadronisation effect as observed on the event shape variables thrust, heavy jet mass, total and wide jet broadening at a centre of mass energy of 161 GeV. Hadronisation effects were studied using JETSET 7.4 PS, HERWIG 5.8 and ARIADNE 4.06. The difference in the hadronisation effects observed in the models studied gives a measure of the systematic error on the measurement of α_s.

8.3 Results on α_s

In order to derive α_s, we fit the theoretical distribution f(y) (after folding in the hadronisation effects) to the measured event shape distributions for a fixed scale $\mu = \sqrt{s}$. For each variable used, the measured data are first corrected for background contamination, detector resolution, acceptance and if needed for initial and final state radiation. The selection and correction of data have been discussed in detail in Chapters 6 and 7.

Since the event shape variables used are affected differently by higher order effects and hadronisation corrections, a comparison of the α_s values determined from several event shape variables allows one to estimate the size of theoretical uncertainties.

8.3.1 Strong Coupling Constant at Reduced CM Energies

For the fit to QCD performed for datasets at reduced centre of mass energies in the range from 30–86 GeV we use the ranges of values of the variables as given in table 8.2. The choice of the range over which data were to be fitted has been based on a number of considerations. We require that the resummation calculation should be reliable over the entire fit range. We further require that the detector and hadronisation correction factors should be reasonably small and uniform across the fit range, and that the hadronisation correction should not be strongly model dependent. The statistics of the sample need to be sufficient for a reliable fit.

Variable	Fit range
1−T	0.025 – 0.330
ρ	0.015 – 0.252
B_T	0.070 – 0.330
B_W	0.030 – 0.200

Table 8.2: Ranges of values of variables used for QCD fits to the data.

Figure 8.2 shows the experimental data, which is corrected for background and detector effect, together with the QCD fits for scaled heavy jet mass at the six centre of mass energies in the range from 30 to 86 GeV. Tables 8.3 and 8.4 contain the values of the strong coupling constant and the errors on it from different sources. They also contain

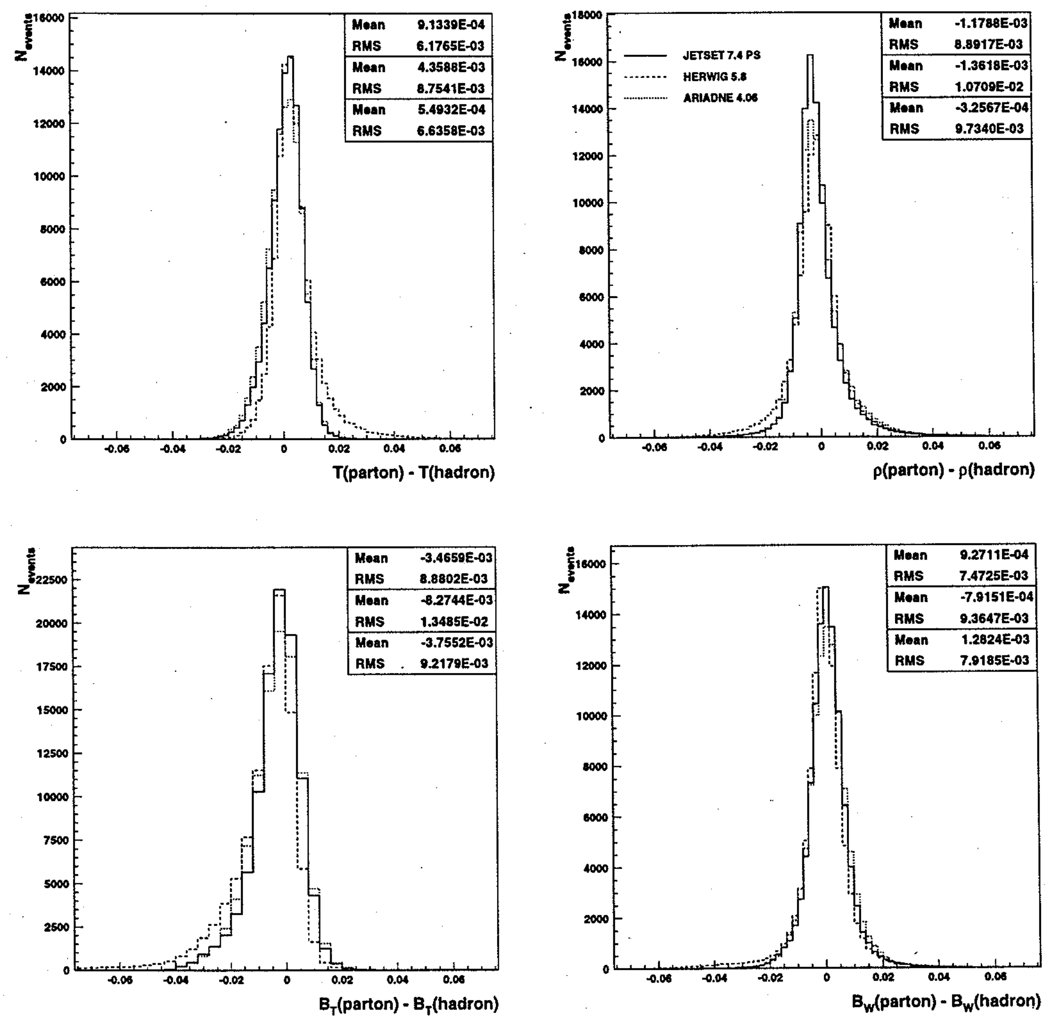

Figure 8.1: Hadronisation effect on the event shape variables thrust, heavy jet mass, total and wide jet broadening at a centre of mass energy of 161 GeV. Hadronisation effects were studied using JETSET 7.4 PS, HERWIG 5.8 and ARIADNE 4.06. Relevant showering and fragmentation parameters of all the Monte Carlo programmes were tuned using L3 data at $\sqrt{s} \simeq 91.2$ GeV. The difference in the hadronisation effects observed in models studied gives a measure of the systematic error on the measurement of a physical variable coming from hadronisation.

the corresponding χ^2 values per degree of freedom. These values are obtained from the fits to fixed order (up to $\mathcal{O}(\alpha_s{}^2)$) together with resummed calculations using hadronisation corrections from JETSET 7.4 PS.

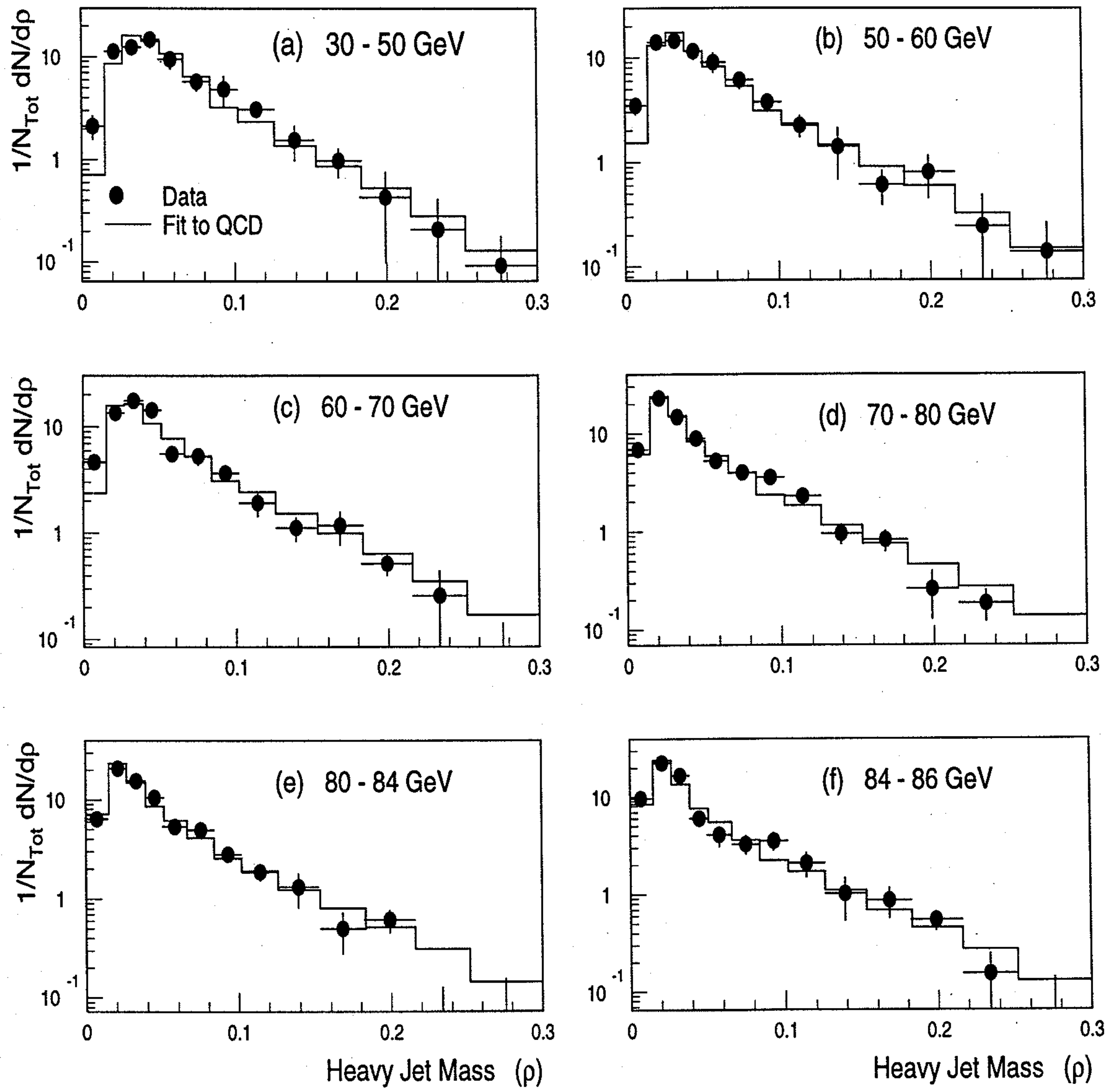

Figure 8.2: Fitted distribution for scaled heavy jet mass (ρ) at different centre of mass energies (a) 30–50 GeV, (b) 50–60 GeV, (c) 60–70 GeV, (d) 70–80 GeV, (e) 80–84 GeV, (f) 84–86 GeV. The histograms correspond to the fits to the QCD predictions.

The errors shown in tables 8.3 and 8.4 are divided into three main parts. The first part corresponds to the statistical errors together with the experimental systematic uncertainties. We have estimated the experimental systematic errors on these measurements in the following way.

- Background fraction in the sample was varied within one standard deviation.

$\sqrt{s}$ (GeV)		(1−T)	ρ	B_T	B_W
30−50	α_s	0.1427	0.1264	0.1472	0.1402
	χ^2/d.o.f.	1.15	1.03	0.37	0.20
	Statistical error	± 0.004	± 0.004	± 0.004	± 0.003
	Systematic error	± 0.007	± 0.006	± 0.010	± 0.014
	Overall experimental error	± 0.008	± 0.007	± 0.011	± 0.015
	Fragmentation Model	± 0.011	± 0.006	± 0.009	± 0.003
	Model parameters	± 0.004	± 0.005	± 0.003	± 0.003
	Hadronisation uncertainty	± 0.011	± 0.006	± 0.009	± 0.003
	QCD scale uncertainty	± 0.004	± 0.002	± 0.006	± 0.004
	Matching scheme uncertainty	± 0.001	± 0.001	± 0.010	± 0.004
	Error due to higher orders	± 0.004	± 0.002	± 0.010	± 0.004
	Overall theoretical error	± 0.012	± 0.006	± 0.013	± 0.005
50−60	α_s	0.1463	0.1355	0.1456	0.1268
	χ^2/d.o.f.	1.02	0.54	0.29	1.71
	Statistical error	± 0.004	± 0.003	± 0.005	± 0.005
	Systematic error	± 0.017	± 0.007	± 0.008	± 0.009
	Overall experimental error	± 0.017	± 0.008	± 0.009	± 0.010
	Fragmentation Model	± 0.009	± 0.002	± 0.006	± 0.001
	Model parameters	± 0.004	± 0.004	± 0.005	± 0.002
	Hadronisation uncertainty	± 0.009	± 0.004	± 0.006	± 0.002
	QCD scale uncertainty	± 0.004	± 0.003	± 0.006	± 0.003
	Matching scheme uncertainty	± 0.001	± 0.001	± 0.005	± 0.004
	Error due to higher orders	± 0.004	± 0.003	± 0.006	± 0.004
	Overall theoretical error	± 0.010	± 0.005	± 0.008	± 0.004
60−70	α_s	0.1441	0.1384	0.1316	0.1154
	χ^2/d.o.f.	0.54	1.60	0.63	0.31
	Statistical error	± 0.004	± 0.002	± 0.004	± 0.003
	Systematic error	± 0.008	± 0.007	± 0.005	± 0.010
	Overall experimental error	± 0.009	± 0.007	± 0.006	± 0.011
	Fragmentation Model	± 0.008	± 0.002	± 0.005	± 0.003
	Model parameters	± 0.004	± 0.003	± 0.003	± 0.002
	Hadronisation uncertainty	± 0.008	± 0.003	± 0.005	± 0.003
	QCD scale uncertainty	± 0.005	± 0.002	± 0.004	± 0.002
	Matching scheme uncertainty	± 0.002	± 0.001	± 0.005	± 0.003
	Error due to higher orders	± 0.005	± 0.002	± 0.005	± 0.003
	Overall theoretical error	± 0.009	± 0.004	± 0.007	± 0.004

Table 8.3: The strong coupling constant, α_s at 30−50, 50−60 and 60−70 GeV from the fits to the event shape variables.

$\sqrt{s}$ (GeV)		(1−T)	ρ	B_T	B_W
70−80	α_s	0.1232	0.1131	0.1255	0.1024
	χ^2/d.o.f.	1.42	0.99	1.28	1.66
	Statistical error	± 0.003	± 0.002	± 0.003	± 0.003
	Systematic error	± 0.010	± 0.003	± 0.006	± 0.012
	Overall experimental error	± 0.010	± 0.004	± 0.007	± 0.012
	Fragmentation Model	± 0.007	± 0.005	± 0.004	± 0.003
	Model parameters	± 0.002	± 0.002	± 0.002	± 0.001
	Hadronisation uncertainty	± 0.007	± 0.005	± 0.004	± 0.003
	QCD scale uncertainty	± 0.003	± 0.002	± 0.004	± 0.002
	Matching scheme uncertainty	± 0.001	± 0.001	± 0.004	± 0.002
	Error due to higher orders	± 0.003	± 0.002	± 0.004	± 0.002
	Overall theoretical error	± 0.008	± 0.005	± 0.006	± 0.004
80−84	α_s	0.1246	0.1176	0.1245	0.1041
	χ^2/d.o.f.	1.01	2.47	0.50	1.12
	Statistical error	± 0.004	± 0.002	± 0.004	± 0.003
	Systematic error	± 0.012	± 0.005	± 0.009	± 0.010
	Overall experimental error	± 0.013	± 0.005	± 0.010	± 0.010
	Fragmentation Model	± 0.006	± 0.007	± 0.005	± 0.007
	Model parameters	± 0.002	± 0.002	± 0.002	± 0.001
	Hadronisation uncertainty	± 0.006	± 0.007	± 0.005	± 0.007
	QCD scale uncertainty	± 0.003	± 0.001	± 0.004	± 0.002
	Matching scheme uncertainty	± 0.001	± 0.001	± 0.005	± 0.002
	Error due to higher orders	± 0.003	± 0.001	± 0.005	± 0.002
	Overall theoretical error	± 0.007	± 0.007	± 0.007	± 0.007
84−86	α_s	0.1156	0.1110	0.1165	0.0993
	χ^2/d.o.f.	0.89	1.21	0.81	0.60
	Statistical error	± 0.004	± 0.003	± 0.005	± 0.003
	Systematic error	± 0.013	± 0.005	± 0.004	± 0.012
	Overall experimental error	± 0.014	± 0.006	± 0.006	± 0.012
	Fragmentation Model	± 0.006	± 0.004	± 0.004	± 0.004
	Model parameters	± 0.002	± 0.002	± 0.002	± 0.001
	Hadronisation uncertainty	± 0.006	± 0.004	± 0.004	± 0.004
	QCD scale uncertainty	± 0.002	± 0.002	± 0.003	± 0.002
	Matching scheme uncertainty	± 0.001	± 0.001	± 0.004	± 0.002
	Error due to higher orders	± 0.002	± 0.002	± 0.004	± 0.002
	Overall theoretical error	± 0.006	± 0.004	± 0.006	± 0.004

Table 8.4: The strong coupling constant, α_s at 70−80, 80−84 and 84−86 GeV from the fits to the event shape variables.

- Selection cuts were varied independently within certain ranges.
- Different smoothening methods were applied to correct measured data for detector resolution and acceptance.
- Two fragmentation models (JETSET and HERWIG) were used to correct the data.
- The overall event sample was compared with events where the isolated photon is restricted in the central part of the detector ($|\cos\theta_\gamma| < 0.70$).

The experimental systematic error is dominated by error coming from use of different smoothening methods for correction of data. The overall experimental error is obtained by adding the statistical and systematic errors in quadrature.

The second part shows the variation in the fitted value of α_s with respect to JETSET 7.4 PS due to the use of different hadronisation models. It also shows the overall variation due to parameter changes in JETSET, the dominant contribution being the Bose-Einstein correlation effect. For all variables, except the scaled heavy jet mass, the most important variation comes from the use of different fragmentation models. We use this as an estimate of the overall hadronisation uncertainty.

The third part summarises the errors coming from unknown higher orders terms in the QCD predictions. The scale error is obtained by repeating the α_s fit for different values of the renormalisation scale in the interval $0.5\sqrt{s} \leq \mu \leq 2\sqrt{s}$. For all these values of the renormalisation scale, a good fit is obtained. The matching scheme uncertainty is obtained from half of the maximum spread due to the variation of the matching algorithm. The systematic errors due to higher order terms have been estimated independently from the scale uncertainty and the matching scheme uncertainty. The larger of these is taken as the theoretical uncertainty due to higher orders. The overall theoretical error is obtained by adding to this, in quadrature, the hadronisation uncertainty.

To obtain a combined value for the strong coupling constant we take the unweighted average of the four α_s values obtained from four variables independently at each centre of mass energy. The overall experimental error is obtained by adding in quadrature the statistical error and the unweighted average of experimental systematic errors. We assign the overall theoretical uncertainty as the average of the theoretical errors obtained from the four different measurements at each centre of mass energy. The combined results are summarised in table 8.5.

8.3.2 Strong Coupling Constant at 161 GeV

For the fit to QCD at $\sqrt{s} = 161$ GeV we use the ranges of values over which the four variables can vary as given in table 8.6.

$\sqrt{s}$ (GeV)	α_s ($\sqrt{s}$)	$\Delta\alpha_s$ (experimental)	$\Delta\alpha_s$ (theoretical)
30–50	0.139	± 0.010	± 0.009
50–60	0.139	± 0.011	± 0.007
60–70	0.132	± 0.008	± 0.006
70–80	0.116	± 0.008	± 0.006
80–84	0.118	± 0.010	± 0.007
84–86	0.111	± 0.010	± 0.005

Table 8.5: The strong coupling constant, α_s at the six centre of mass energies from the four fits to the event shape variables.

Variable	Fit range
1–T	0.00 – 0.300
ρ	0.00 – 0.255
B_T	0.00 – 0.300
B_W	0.05 – 0.165

Table 8.6: Ranges of values of variables used for QCD fit to the data at $\sqrt{s} = 161$ GeV.

Figures 8.3 and 8.4 show the experimental data together with the QCD fits for the four variables thrust, scaled heavy jet mass, total and wide jet broadening. Table 8.7 lists the values of α_s, the errors from different sources and the χ^2 as obtained from the fits to $\mathcal{O}({\alpha_s}^2)$ + resummed calculations using hadronisation corrections from JETSET 7.4 PS with standard L3 parameters.

The first error shown in table 8.7 corresponds to statistical errors and experimental systematic uncertainties added in quadrature. The experimental systematic errors come mainly due to uncertainties in detector calibration and response and uncertainties in the background estimates. We use an alternative definition of clusters to build the observables and repeat our analysis to estimate the effect. Systematic uncertainty comes from possible inhomogeneities in detector response over the full acceptance. This is estimated by repeating the analysis only for the events where the event thrust points inside the central part of the detector where the resolution is better ($|\cos\theta_{\mathrm{thrust}}| < 0.7$). The uncertainty coming from the background composition of the selected event sample has been estimated by repeating the analysis using an alternative selection cut to remove the hard initial state photon and also varying the background contaminations coming from W^+W^- and two photon processes.

The second error listed in table 8.7 comes from hadronisation corrections and the third one summarises the errors coming from higher order terms in the QCD predictions. We combine the results obtained from the four variables in the same manner as we have done for the case of data at reduced centre of mass energy to obtain

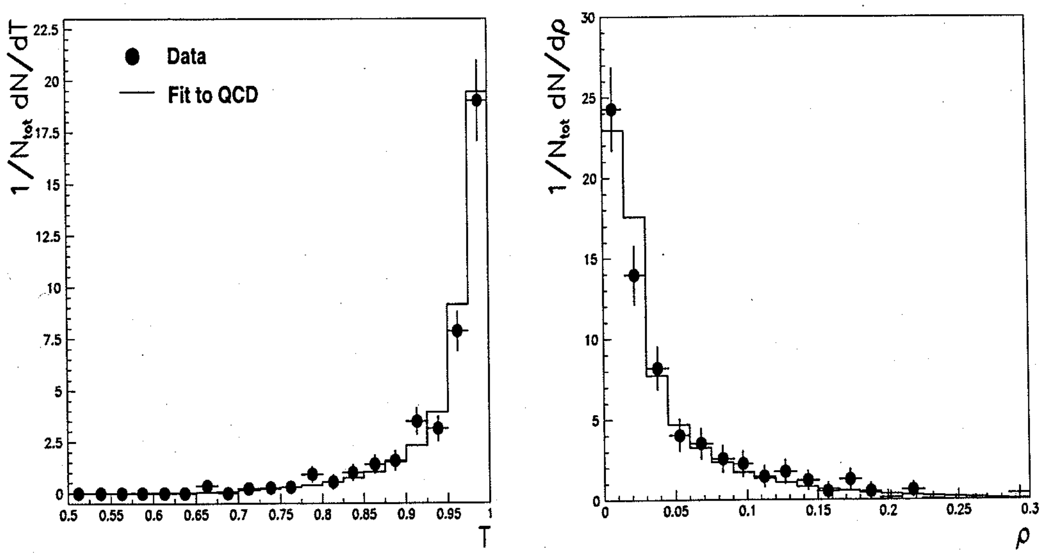

Figure 8.3: Fitted distribution for thrust (T) and scaled heavy jet mass (ρ) at a $\sqrt{s}$ = 161 GeV. The points correspond to data corrected for background and detector effects whereas the histograms correspond to the fits to the QCD predictions.

	(1−T)	ρ	B_T	B_W
α_s (161 GeV)	0.099	0.098	0.108	0.101
χ^2/d.o.f.	1.04	0.74	2.12	0.54
Statistical error	± 0.005	± 0.005	± 0.004	± 0.004
Systematic error	± 0.003	± 0.003	± 0.001	± 0.002
Overall experimental error	± 0.006	± 0.006	± 0.004	± 0.005
Fragmentation Model	± 0.002	± 0.002	± 0.002	± 0.001
Model parameters	± 0.002	± 0.002	± 0.001	± 0.001
Hadronisation uncertainty	± 0.002	± 0.002	± 0.002	± 0.001
QCD scale uncertainty	± 0.002	± 0.001	± 0.003	± 0.002
Matching scheme uncertainty	± 0.002	± 0.002	± 0.005	± 0.005
Error due to higher orders	± 0.002	± 0.002	± 0.005	± 0.005
Overall theoretical error	± 0.003	± 0.003	± 0.005	± 0.005

Table 8.7: α_s from the fits to the event shape variables 1−T, ρ, B_T, and B_W at $\sqrt{s}$ = 161 GeV. The first error is a combination of statistical and systematic errors whereas the second and third errors are due to hadronisation correction and due to higher order terms.

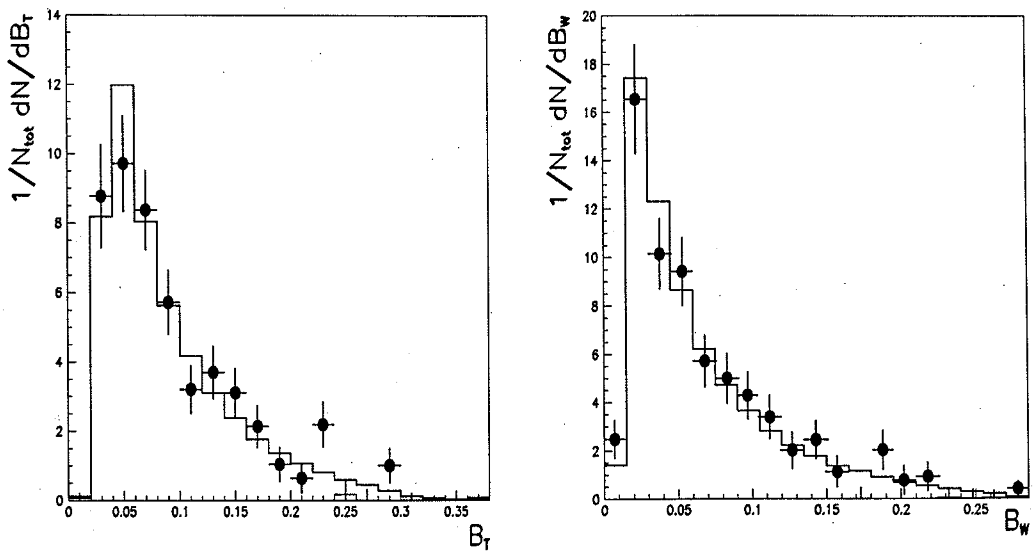

Figure 8.4: Fitted distribution for total (B_T) and wide (B_W) jet broadening variables at a $\sqrt{s}$ = 161 GeV. The points correspond to data corrected for background and detector effects whereas the histograms correspond to the fits to the QCD predictions.

$$\alpha_s \text{ (161 GeV)} = 0.102 \pm 0.005 \text{ (exp)} \pm 0.005 \text{ (theor)}$$

where the first error is experimental and the second one is theoretical.

Chapter 9

Summary

We have presented the results from an analysis of data collected by the L3 experiment around Z peak and at $\sqrt{s} = 161$ GeV in the Large Electron Positron collider, LEP. Events with hadronic final state have been used to determine the strong coupling constant (α_s), from a study of different events shape variables. We have also performed a precise energy calibration using the hadronic events.

A new method of energy calibration has been introduced which uses informations from the central tracking detector, the electromagnetic and hadron calorimeters, the muon chamber and the possible correlations in energy measurement among the neighbouring detector components. This method gives a better energy resolution of 9% compared to the resolution obtained (13%) by the standard method used in L3.

We have studied events from hadronic Z decays with an energetic isolated photon in the final state. Photons from initial state radiation or off the quarks in the final state constitute the signal events. Emission of a high energy isolated photon off a quark (antiquark) takes place at the first branching of the parton shower development. On the other hand, the development of the complete hadronic shower takes place over a longer time scale. One can, therefore, study hadron production at reduced centre of mass energies from a study of hadronic events with hard isolated photons.

The centre of mass energy of the hadronic system after the removal of the photon ranges from 30 GeV to 86 GeV depending on the energy of the emitted photon. We have studied several event shape variables at this reduced centre of mass energies. In particular, distributions for thrust, heavy jet mass and jet broadening variables, for which improved perturbative QCD calculations ($\mathcal{O}({\alpha_s}^2)$ together with resummation of large logarithm terms) exist, have been measured. From a fit of the data, corrected for background and detector effects, to resummed $\mathcal{O}({\alpha_s}^2)$ QCD calculations, we have determined the strong coupling constant over a wide range of energy.

The present analysis of the determination of the strong coupling constant at different reduced centre of mass energies using hadronic events from Z decays with an energetic isolated photon in the final state is the first measurement of its kind. Determination of α_s from one single experiment would reduce the experiment dependent systematic errors.

The structure of hadronic events at $\sqrt{s} = 161$ GeV has been studied as well. The strong coupling constant at this centre of mass energy has been determined again from a study of event shape variables.

Figure 9.1 shows the energy evolution of the mean of the event shape variables for all the energy points studied together with the earlier L3 measurements at $\sqrt{s} = 91.2$ GeV and 133 GeV. We list the measured values of α_s at the corresponding energy points in table 9.1.

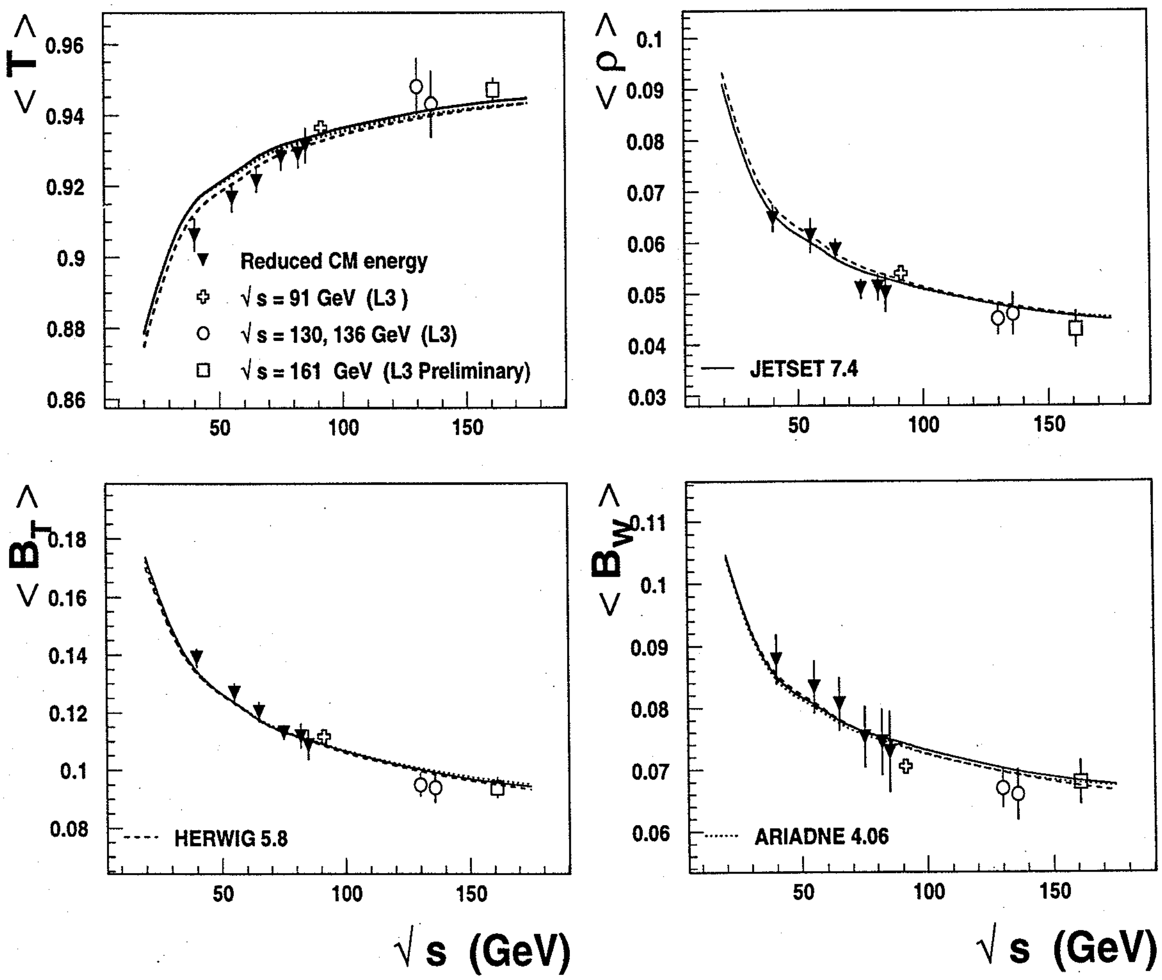

Figure 9.1: Distributions of mean (a) thrust (T), (b) scaled heavy jet mass (ρ), (c) total jet broadening (B_T), (d) wide jet broadening (B_W) as a function of centre of mass energy. The smooth lines correspond to the predictions of different QCD models.

$\sqrt{s}$ (GeV)	α_s ($\sqrt{s}$)	$\Delta\alpha_s$ (expt)	$\Delta\alpha_s$ (theo)
30–50	0.139	± 0.010	± 0.009
50–60	0.139	± 0.008	± 0.007
60–70	0.132	± 0.007	± 0.006
70–80	0.116	± 0.008	± 0.006
80–84	0.118	± 0.008	± 0.007
84–86	0.111	± 0.008	± 0.005
91	0.122	± 0.002	± 0.007
133	0.107	± 0.005	± 0.005
161	0.102	± 0.005	± 0.005

Table 9.1: α_s at different centre of mass energies using L3 data. Measured values of α_s at the six reduced centre of mass energies together with similar measurements from L3 at $\sqrt{s} = m_Z$, 133 GeV and 161 GeV are displayed.

The energy dependence of the strong coupling has been studied with the measurements done from the L3 experiment alone. Since the theoretical errors are common to all these measurements, we have carried out a fit through these measured α_s values to QCD prediction using only the experimental errors. The fit with QCD evolution gives

$$\alpha_s\,(m_Z) = 0.119 \pm 0.002\;(\mathrm{exp})$$

where $\chi^2 = 10.3$ for 9 data points leading to a fit probability of 0.25. One can take the unweighted average of the 9 different estimates of theoretical uncertainties as the overall theoretical error. Thus one obtains

$$\alpha_s\,(m_Z) = 0.119 \pm 0.002\;(\mathrm{exp}) \pm 0.007\;(\mathrm{theo})\;.$$

If one considers α_s to be independent of energy, one obtains a χ^2 of 31.5 for 9 data points giving rise to a probability of 1.2×10^{-4}. The results of the two fits together with the L3 measurements are shown in figure 9.2. The measurements strongly suggest the running of α_s ala QCD.

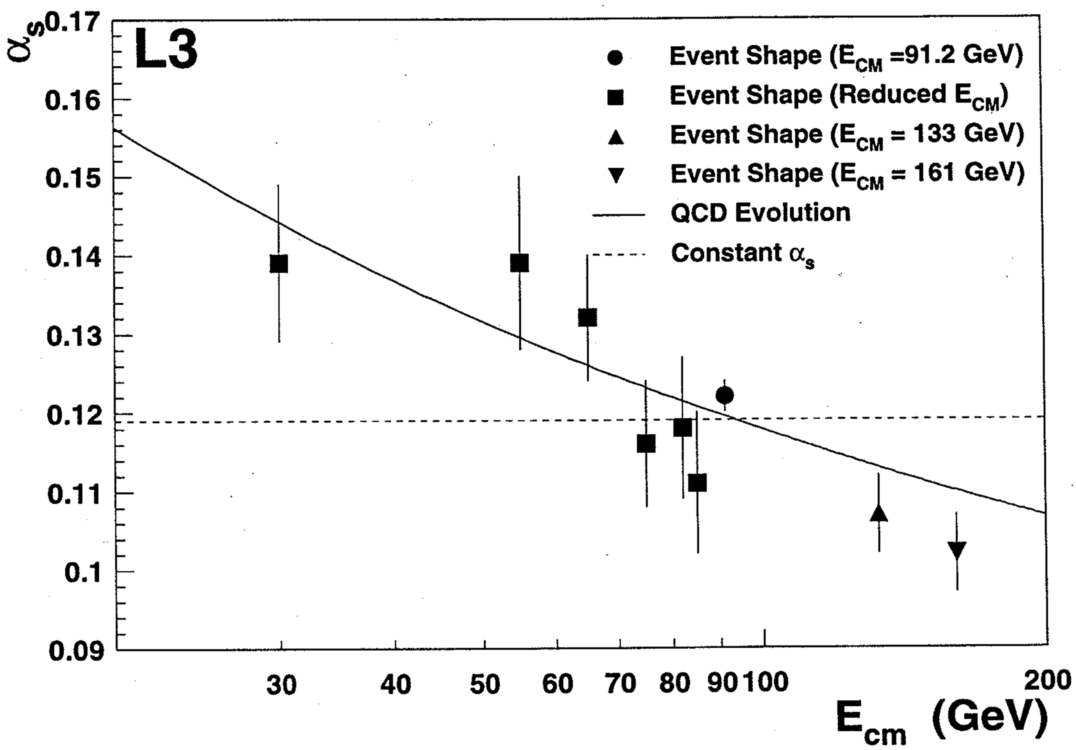

Figure 9.2: Measured values of α_s at the six reduced centre of mass energies together with similar measurements from L3 at $\sqrt{s} = 91.2$, 133 and 161 GeV. The solid line is the results of a fit assuming running of α_s as predicted by QCD, whereas the dotted line is a fit with constant α_s.

Publications of Subir Sarkar

[1] Further Results on Cerium Fluoride Crystals.
Crystal Clear Collaboration, S.Anderson *et al.*, Nuclear Instruments and Methods **A332** (1993) 73.

[2] A Measurement of Tau Polarization at LEP.
L3 Collaboration, M. Acciarri *et al.*, Physics Letters **B341** (1994) 245.

[3] B* Production in Z Decays at LEP.
L3 Collaboration, M. Acciarri *et al.*, Physics Letters **B345** (1995) 589.

[4] Energy and Particle flow in Three-Jet and Radiative Two-Jet Events from Hadronic Z Decays.
L3 Collaboration, M. Acciarri *et al.*, Physics Letters **B345** (1995) 74.

[5] Measurement of Exclusive Branching Fractions of Hadronic One-Prong Tau Decays.
L3 Collaboration, M. Acciarri *et al.*, Physics Letters **B345** (1995) 93.

[6] Search for Anomalous $Z \rightarrow \gamma\gamma\gamma$ Events at LEP.
L3 Collaboration, M. Acciarri *et al.*, Physics Letters **B345** (1995) 609.

[7] Combined Preliminary Data on Z Parameters from the LEP Experiments and Constraints
on the Standard Model.
The LEP Collaborations ALEPH, DELPHI, L3 and OPAL and
the LEP Electroweak Working Group.
CERN preprint CERN-PPE/94-187; November 25, 1994.

[8] Measurement of Energetic Single-Photon Production at LEP.
L3 Collaboration, M. Acciarri *et al.*, Physics Letters **B346** (1995) 190.

[9] Measurement of the Weak Charged Current Structure in Semileptonic b-Hadron decays.
L3 Collaboration, M. Acciarri *et al.*, Physics Letters **B351** (1995) 375.

[10] Search for Neutralinos in Z Decays.
L3 Collaboration, M. Acciarri *et al.*, Physics Letters **B350** (1995) 109.

[11] Tests of QED at LEP Energies using $e^+e^- \rightarrow \gamma\gamma(\gamma)$ and $e^+e^- \rightarrow l^+l^-\gamma\gamma$.
L3 Collaboration, M. Acciarri *et al.*, Physics Letters **B353** (1995) 136.

[12] One-prong τ Decays with Neutral Kaons.
L3 Collaboration, M. Acciarri *et al.*, Physics Letters **B352** (1995) 487.

[13] Evidence for Gluon Interference in Hadronic Z Decays.
L3 Collaboration, M. Acciarri *et al.*, Physics Letters **B353** (1995) 145.

[14] Study of the $K^o_S K^o_S$ Final State in Two Photon Collision.
L3 Collaboration, M. Acciarri *et al.*, Physics Letters **B363** (1995) 118.

[15] Search for Neutral Charmless B Decays At LEP.
L3 Collaboration, M. Acciarri *et al.*, Physics Letters **B363** (1995) 127.

[16] Search for the Decays $B^o_d \rightarrow \gamma\gamma$ and $B^o_s \rightarrow \gamma\gamma$.
L3 Collaboration, M. Acciarri *et al.*, Physics Letters **B363** (1995) 137.

[17] A Combination of Preliminary LEP Electroweak Measurements and Constraints on the Standard Model.
The LEP Collaborations, ALEPH, DELPHI, L3, OPAL and the LEP Electroweak Working Group.
CERN preprint CERN-PPE/95-172, November 25, 1994.

[18] Measurement of η Production in Two and Three-Jet Events from Hadronic Z Decays at LEP.
L3 Collaboration, M. Acciarri *et al.*, Physics Letters **B371** (1996) 126.

[19] Measurement of Hadron and Lepton-Pair Production at 130 GeV $< \sqrt{s} <$ 140 GeV at LEP.
L3 Collaboration, M. Acciarri *et al.*, Physics Letters **B370** (1996) 195.

[20] Studies of Hadronic Event Structure and α_s determination at $\sqrt{s} = 130, 136$ GeV.
L3 Collaboration, M. Acciarri *et al.*, Physics Letters **B371** (1996) 137.

[21] Search for Excited Leptons in e^+e^- Annihilation at $\sqrt{s} =$ 130–140 GeV.
L3 Collaboration, M. Acciarri *et al.*, Physics Letters **B370** (1996) 211.

[22] Measurement of Muon Pair Production at $50 < \sqrt{s} < 86$ GeV at LEP.
L3 Collaboration, M. Acciarri *et al.*, Physics Letters **B374** (1996) 331.

[23] Combining Heavy Flavour Electroweak Measurements at LEP.
The LEP Collaborations ALEPH, DELPHI, L3 and OPAL
Submitted to Nuclear Instruments and Methods.

[24] Search for Supersymmetric Particles at 130 GeV $< \sqrt{s} <$ 140 GeV at LEP.
L3 Collaboration, M. Acciarri *et al.*, Physics Letters **B377** (1996) 289.

[25] Search for Unstable Sequential Neutral and Charged Heavy Leptons in e^+e^- annihilation at $\sqrt{s} = 130$ and 136 GeV.
L3 Collaboration, M. Acciarri *et al.*, Physics Letters **B377** (1996) 304.

[26] Measurement of the Michel Parameters and the average tau neutrino helicity from tau decays in $e^+e^- \to \tau^+\tau^-$.
L3 Collaboration, M. Acciarri *et al.*, Physics Letters **B377** (1996) 313.

[27] Observation of Multiple Hard Photon Final States at $\sqrt{s} = 130$–140 GeV at LEP.
L3 Collaboration, M. Acciarri *et al.*, Physics Letters B, Accpted.

[28] Measurement of the Branching Ratios $b \longrightarrow e\nu X$, $\mu\nu X$, $\tau\nu X$ and νX.
L3 Collaboration, M. Acciarri *et al.*, Zeitschrift für Physik . **C71** (1996) 379.

[29] Search For New Particles In Hadronic Events With Isolated Photons.
L3 Collaboration, M. Acciarri *et al.*, Physics Letters B accepted

[30] Measurement of the B°_d Meson Oscillation Frequency.
L3 Collaboration, M. Acciarri *et al.*, Physics Letters **B383** (1996) 487.

[31] Search For Neutral Higgs Boson Production Through the Process $e^+e^- \to Z^* + H^\circ$.
L3 Collaboration, M. Acciarri *et al.*, Physics Letters B (accepted).

[32] Measurement of the Lifetime of the Tau Lepton.
L3 Collaboration, M. Acciarri *et al.*, Physics Letters B (accepted).

[33] Search for Neutral B Meson Decays to Two Charged Leptons.
L3 Collaboration, M. Acciarri *et al.*, Physics Letters B (submitted).

Reference

[1] S. L. Glashow, Nuclear Physics **22** (1961) 579;
S. Weinberg, Physical Review Letters **19** (1967) 1264;
A. Salam, in Proceedings of the 8th Nobel Symposium, ed. N. Svartholm, (Almquist and Wiksell, Slockholm, 1968).

[2] P. W. Higgs, Physics Letters **12** (1964) 132.

[3] M. Gell-Mann, Acta Phys. Austriaca Suppl. **IX** (1972) 733;
H. Fritzsch and M. Gell-Mann, 16th International Conference on High Energy Physics, Batavia, 1972; editors J.D. Jackson and A. Roberts, National Accelerator Laboratory (1972);
H. Fritzsch, M. Gell-Mann and H. Leytwyler, Physics Letters **B47** (1973) 365;
D.J. Gross and F. Wilczek, Physical Review Letters **30** (1973) 1343;
D.J. Gross and F. Wilczek, Physical Review **D8** (1973) 3633;
H.D. Politzer, Physical Review Letters **30** (1973) 1346;
G. 't Hooft, Nuclear Physics **B33** (1971) 173.

[4] W. Caswell, Physical Review Letters **30** (1974) 244;
D. R. T. Jones, Nuclear Physics **B75** (1974) 531;
O. V. Tarasov, A. A. Vladimirov, A. Y. Zharkov, Physics Letters **B93** (1980) 429.

[5] P. Hoyer *et al.*, Nuclear Physics **B161** (1979) 349.

[6] A. Ali *et al.*, Nuclear Physics **B168** (1980) 409;
A. Ali *et al.*, Physics Letters **B93** (1980) 155.

[7] T. Hebbeker, Physics Reports **217** (1992) 69;
S.Bethke, J.E. Pilcher, Annual Review of Nuclear & Particle Science **42** (1992) 251;
M. Schmelling, CERN/PPE 94-184, submitted to Physica Scripta.

[8] S.G. Gorishny, A.L. Kataev and S.A. Larin, Physics Letters **B212** (1988) 238.

[9] R.K. Ellis, D.A. Ross and A.E. Terrano, Nuclear Physics **B178** (1981) 421; F. Fabricius *et al.*, Physics Letters **B97** (1980) 431; F. Fabricius *et al.*, Zeitschrift

für Physik **C11** (1982) 315; F. Gutbrod, G. Kramer, G. Schierholz, Zeitschrift für Physik **C21** (1984) 235;

[10] B. R. Webber, Annual Review of Nuclear & Particle Science **36** (1986) 253.

[11] G. Alterali, G. Parisi, Nuclear Physics **B126**(1977) 298.

[12] R. Field, R. P. Feynman, Nuclear Physics **B136** (1978) 1.

[13] JADE Collaboration, W. Bartel *et al.*, Physics Letters **B101** (1981) 129;
JADE Collaboration, W. Bartel *et al.*, Zeitschrift für Physik **C21** (1983) 37;
JADE Collaboration, F. Ould-Saada *et al.*, Zeitschrift für Physik **C39** (1988) 1.

[14] B. Andersson *et al.*, Physics Reports **97** (1983) 31.

[15] G. C. Fox and S. Wolfram, Nuclear Physics **B213** (1983) 65.

[16] S. Brandt *et al.*, Physics Letters **12** (1964) 57;
E. Fahri, Physical Review Letters **39** (1977) 1587.

[17] MARK J Collaboration, D.P. Barber *et al.*, Physical Review Letters **43** (1979) 830.

[18] MARK J Collaboration, D.P. Barber *et al.*, Physics Letters **B89** (1979) 139.

[19] T. Chandramohan and L. Clavelli, Nuclear Physics **B184** (1981) 365;
MARK II Collaboration, A. Peterson *et al.*, Physical Review **D37** (1988) 1;
TASSO Collaboration, W. Braunschweig *et al.*, Zeitschrift für Physik **C45** (1989) 11.

[20] G.C. Fox, F. Wolfram, Physical Review Letters **41** (1978) 1581;
G.C. Fox, F. Wolfram, Nuclear Physics **B149** (1979) 413;
G.C. Fox, F. Wolfram, Physics Letters **B82** (1979) 134.

[21] JADE Collaboration, W. Bartel *et al.*, Zeitschrift für Physik **C33** (1986) 23;
JADE Collaboration, S. Bethke *et al.*, Physics Letters **B213** (1988) 235.

[22] Y.L. Dokshitzer, Contribution to the Workshop on Jets at LEP and HERA, Durham (1990);
N. Brown and W.J. Stirling, Rutherford Preprint RAL-91-049;
S. Catani *et al.*, Physics Letters **B269** (1991) 432;
S. Bethke *et al.*, Nuclear Physics **B370** (1992) 310.

[23] J.D. Bjorken, S.J. Brodsky, Physical Review **D1** (1970) 1416.

[24] G. Parisi, Physics Letters **B74** (1978) 65;
J.F. Donoghue, F.E. Low, S.Y. Pi, Physical Review **D20**(1979) 1759.

[25] S. Catani *et al.*, Physics Letters **B295** (1992) 269.

[26] ALEPH Collaboration D. Decamp *et al.*, Nuclear Instruments & Methods **A294** (1990) 127.

[27] DELPHI Collaboration P. Aarnio *et al.*, Nuclear Instruments & Methods **A303** (1991) 233.

[28] L3 Collaboration B. Adeva *et al.*, Nuclear Instruments & Methods **A289** (1990) 35.

[29] OPAL Collaboration K. Ahmet *et al.*, Nuclear Instruments & Methods **A305** (1991) 275.

[30] R. Bailey, (World Scientific, Singapore, 1993), volume International Journal of Modern Physics A, Proc. Suppl., p. 401.
J. Jowett, The 8-bunch pretzel scheme, Proceedings of the first workshop on LEP performance, Chamonix 1991, CERN-SL-91-23 (1991).

[31] A. Hofman, Performance Limitations at LEP, Preprint CERN-SL-94-058, CERN, 1994.

[32] C. Bovet *et al.*, Final Report of the 1994 Bunch Train Study Group, Preprint CERN-SL-94-95-AP, CERN, 1994.

[33] L3 Collaboration, M. Acciari *et al.*, Nuclear Instruments & Methods **A351** (1994) 300.
L3 Collaboration, O. Adriani *et al.*, Physics Reports **236** (1993) 1.

[34] H. Akbari *et al.*, Nuclear Instruments & Methods **A315** (1992) 161;
F. Beissel *et al.*, Nuclear Instruments & Methods **A332** (1993) 33.

[35] M. Caccia *et al.*, Nuclear Instruments & Methods **A315** (1992) 197;
G. Ambrosi *et al.*, Nuclear Instruments & Methods **A344** (1994) 133;
O. Adriani *et al.*, Nuclear Instruments & Methods **A348** (1994) 431;
The L3 SMD collaboration, M. Acciarri *et al.*, Nuclear Instruments & Methods **A351** (1994) 300;
M. Acciarri *et al.*, Nuclear Instruments & Methods **A360** (1995) 103.

[36] A. Bay *et al.*, Nuclear Instruments & Methods **A321** (1992) 119.

[37] The L3 BGO Collaboration, J. A. Bakken *et al.*, Nuclear Instruments & Methods **A343** (1994) 456.

[38] A. Arefiev *et al.*, Nuclear Instruments & Methods **A285** (1989) 403;